

이학박사 학위논문

# Studies on Graphene-based Nanomaterials for Biomedical Applications

그래핀 기반 나노소재들의 바이오의료 응용연구

2019년 2월

서울대학교 대학원

화학부 물리화학 전공

유 제 민

# Studies on Graphene-based Nanomaterials for Biomedical Applications

Advisor: Byung Hee Hong

Submitting a Ph.D. Dissertation of Chemistry

February 2019

Graduate School of Natural Sciences  
Seoul National University  
Chemistry Major

Je Min Yoo

Confirming the Ph.D. Dissertation written by

Je Min Yoo

February 2019

Chair	<u>Seokmin Shin</u>	(Seal)
-------	---------------------	--------

Vice Chair	<u>Byung Hee Hong</u>	(Seal)
------------	-----------------------	--------

Examiner	<u>Yan Lee</u>	(Seal)
----------	----------------	--------

Examiner	<u>Jung Pyo Lee</u>	(Seal)
----------	---------------------	--------

Examiner	<u>Young-Ho Lee</u>	(Seal)
----------	---------------------	--------

## **Abstract**

# **Studies on Graphene-based Nanomaterials for Biomedical Applications**

Je Min Yoo

Department of Chemistry

The Graduate School

Seoul National University

Due to many of its unprecedented physical, electrical and chemical properties, graphene has gained enormous attention of researchers since its first historical discovery in 2004. Technically, the term ‘graphene’ refers to a two-dimensional single-atom-thick graphite film that once was deemed to plausibly replace indium tin oxide for transparent flexible displays. In addition to the film type graphene suitable for macroscopic applications, the noticeable features of other forms of graphene-based nanomaterials in solution have been recently revealed for applications in other branches of science including biology and nanomedicine. Along with the current research trends in these areas giving special attention to employing novel nanomaterials, we have performed some innovative studies to demonstrate the importance of graphene and its derivatives for versatile applications in these fields. This dissertation thus highlights the implications of graphene film and graphene-based nanomaterials for human health and the treatment of neurodegenerative diseases.

*Chapter 1* is an introductory guide to graphene-based nanomaterials, which include their applications in biology and medical science, relevant preparation steps and some recent toxicity/biodegradation studies.

*Chapter 2* discusses the use of chemical vapor deposition graphene film for degradation of phenolic compounds in industrial wastewater. Phenol and its derivatives are considered to be the major threatening substances as they can be potentially mutagenic and carcinogenic. Although previous attempts have successfully destructed these compounds through ferrous ion-based advanced oxidation processes, they require complicated and costly procedures including environmentally harmful residual salt removal and pH adjustment. The chapter suggests the unprecedented role of the CVD graphene film in the generation of hydroxyl radicals – the active components in AOP for phenol destruction – from hydrogen peroxide through immediate electron transfer, and demonstrates the application of a recyclable CVD graphene film as an environment-friendly catalyst without the need of additional treatments.

*Chapter 3* highlights the therapeutic application of graphene quantum dots for Parkinson's disease. The pathological hallmark of Parkinson's disease is closely related to the aggregation of misfolded  $\alpha$ -synuclein fibrils. By inhibiting the fibrillation of  $\alpha$ -synuclein and inducing disaggregation of mature fibrils as well as blocking their transmission to neighboring neurons, GQDs prevent/rescue the death of dopaminergic neurons in the midbrain through the penetration across the blood-brain barrier. The outcomes indicate GQDs' potent therapeutic efficacy and are especially promising as the current clinical drugs focus merely on alleviating motor dysfunctions by injecting levodopa, the precursor of dopamine.

Finally, *Chapter 4* discusses another therapeutic aspect of graphene quantum dots for neurodegenerative diseases, their effects on Niemann-Pick type C disease. This study provides new insights on graphene quantum dots' ability to deplete intracellular cholesterol and restore compromised autophagic flux to treat lysosomal storage diseases.

**Keyword :** Graphene, Graphene Quantum Dots, Biomedical Applications, Environmental Catalyst, Nanomedicine, Neurodegenerative Diseases

**Student Number :** 2013-20274

# Table of Contents

<b>Abstract of Dissertation .....</b>	<b>i</b>
<b>Table of Contents .....</b>	<b>iv</b>
<b>List of Figures and Tables .....</b>	<b>vi</b>

## **Chapter 1. Introduction of Graphene-based Nanomaterials**

1.1. Applications in Biology and Medical Science .....	1
1.1.1. Sensing Applications.....	2
1.1.2. Therapeutic Applications .....	3
1.1.3. Fluorescence Bio-imaging .....	4
1.2. Preparation of Graphene-based Nanomaterials.....	6
1.2.1. Enhancing the Stability under Physiological Conditions.....	7
1.2.2. Reduction of GOs .....	8
1.3. Toxicity of Graphene-based Nanomaterials.....	9
1.3.1. <i>In vitro</i> Toxicity of Graphene-based Nanomaterials .....	9
1.3.2. <i>In vivo</i> Toxicity of Graphene-based Nanomaterials.....	11
1.3.3. Biodegradation of Graphene-based Nanomaterials .....	13
1.4. Perspectives and Other Applications.....	15
1.5. References .....	17

## **Chapter 2. Catalytic Degradation of Phenols by Recyclable CVD Graphene Films**

1.1. Abstract .....	21
1.2. Introduction.....	22
1.3. Results and Discussion.....	23
1.4. Conclusion .....	31
1.5. Experimental .....	32
1.6. Supplementary Information .....	34

1.7. References .....	37
 <b>Chapter 3. Graphene Quantum Dots Prevent <math>\alpha</math>-synucleinopathy in Parkinson's Disease</b>	
1.1. Abstract .....	39
1.2. Results and Discussion.....	40
1.3. Conclusion .....	54
1.4. Experimental .....	54
1.5. Supplementary Information .....	70
1.6. References .....	89
 <b>Chapter 4. Graphene Quantum Dots Alleviate Impaired Functions in Niemann-Pick Type C Disease <i>in vivo</i></b>	
1.1. Abstract .....	92
1.2. Introduction.....	93
1.3. Results and Discussion.....	94
1.4. Conclusion .....	102
1.5. Experimental .....	102
1.6. Supplementary Information .....	108
1.7. References .....	114
 <b>Appendix .....</b>	 <b>116</b>
 <b>Abstract in Korean .....</b>	 <b>120</b>

# List of Figures and Tables

## Chapter 1

**Figure 1-T1.** Characteristic features of graphene-based nanomaterials.

**Figure 1-1.** Graphene based *in vivo* targeting imaging agents.

**Figure 1-2.** Dynamic tracking of protein of interest.

**Figure 1-3.** *In vivo* imaging and bio-distribution of the carboxylated GQDs.

**Figure 1-4.** Enzymatic oxidation of GOs.

## Chapter 2

**Figure 2-1.** Preliminary experiments to validate CVD graphene's catalytic activity with 1 cm<sup>2</sup> Gr/SiO<sub>2</sub>.

**Figure 2-2.** Time-resolved HPLC analysis of degraded products.

**Figure 2-3.** Area-dependent catalytic activity and recycle test.

**Figure 2-S1.** Detailed analysis on the properties of monolayer graphene.

**Figure 2-S2.** Supplementary HPLC data for the degraded products.

**Figure 2-S3.** XPS analysis on graphene pre- and post-phenol degradation.

## Chapter 3

**Figure 3-1.** Effect of GQDs on  $\alpha$ -syn fibrillization and fibril disaggregation.

**Figure 3-2.** Detailed analysis of the interaction between GQDs and mature  $\alpha$ -syn fibrils during the dissociation process.

**Figure 3-3.** Effect of GQDs on  $\alpha$ -syn PFF-induced neuronal death, pathology and transmission *in vitro*.



**Figure 3-4.** Effect of GQDs on  $\alpha$ -syn-induced pathologies *in vivo*.

**Figure 3-ST1.** Mean  $\pm$  s.d. values and P values of Figure 1b, c, e, and f.

**Figure 3-S1.** Schematic overview of the therapeutic effect of GQDs on the pathogenesis of PD.

**Figure 3-S2.** Synthesis and biotinylation of GQDs and binding assay between GQDs-biotin and  $\alpha$ -syn fibrils.

**Figure 3-S3.** The effect of GQDs on disaggregation of  $\alpha$ -syn fibrils.

**Figure 3-S4.** The effect of GQDs on disaggregation of  $\alpha$ -syn PFFs.

**Figure 3-S5.**  $^1\text{H}$ - $^{15}\text{N}$  HSQC spectral analysis.

**Figure 3-S6.** The effect of GQDs on  $\alpha$ -syn PFFs-induced cell death and restricted neurite outgrowth.

**Figure 3-S7.** The effect of GQDs on  $\alpha$ -syn PFFs-induced mitochondrial dysfunction and oxidative stress.

**Figure 3-S8.** The effect of GQDs on  $\alpha$ -syn PFFs-induced primary neuronal toxicity and pathology at different treatment points of GQDs and live cell imaging.

**Figure 3-S9.** The BBB permeability of GQDs. a, Schematic illustration of the *in vitro* BBB model.

**Figure 3-S10.** The effect of GQDs on  $\alpha$ -syn PFFs-induced glial cell activation in the SN.

**Figure 3-S11.** The effect of GQDs on pathologies and glial cell activation of hA53T  $\alpha$ -syn transgenic mice.

**Figure 3-S12.** Long-term *in vitro* and *in vivo* toxicity of GQDs.

**Figure 3-S13.** The comparative effects of nano-GOs and rGQDs on  $\alpha$ -syn PFFs

induced primary neuronal toxicity, disaggregation of fibrils and the BBB permeability.

## *Chapter 4*

**Figure 4-1.** The effect of GQDs on abnormal characteristics in NPC-iNSC.

**Figure 4-2.** Analysis of the interaction between GQDs and cholesterol in NPC-iNSC.

**Figure.3** The effect of GQDs on impaired autophagy *in vitro*.

**Figure 4.** The effect of GQDs on NPC1 pathologies *in vivo*.

**Figure 4-S1.** Characterisation of GQDs.

**Figure 4-S2.** Direct conversion of NPC1 patient derived fibroblasts to neural stem cells.

**Figure 4-S3.** Extended  $^1\text{H}$  NMR spectra.

**Figure 4-S4.** The time-dependent effect of GQDs on cholesterol accumulation in NPC-iNSC and the effect of GQDs-biotin.

**Figure 4-S5.** Cytotoxicity, survival rate, *in vitro* and *in vivo* permeability of GQDs.

**Figure 4-S6.** Inhibited microgliosis in GQDs treated NPC1 mutant mice.

# ***Chapter 1***

## ***Introduction of Graphene-based Nanomaterials***

### **1.1. Applications in Biology and Medical Science**

Since its first serendipitous, yet historical discovery by British scientists in 2004,<sup>1</sup> graphene has attracted significant attention of researchers from all fields of science for exploiting many of its exceptional properties. One of the major research foci has been replacing indium tin oxide (ITO) with large-scale, high-quality chemical vapor deposition (CVD) graphene for macroscopic applications such as flexible thin films for transparent electrodes. Additional studies in the fields of electronics, physics, and materials science have also been extensively investigated.<sup>2</sup>

Recently, given an increasing consensus on graphene's environmentally-friendly aspects, researchers have considered employing graphene in other branches of science such as biology and medicine. Above all, dispersed graphene-based nanomaterials including graphene oxides (GOs), graphene quantum dots (GQDs), and reduced graphene oxides (rGOs) are more frequently employed for biomedical applications while the term graphene refers to a two-dimensional atomic film. GOs and GQDs are especially broadly utilized for biomedical applications due to their high dispersibility and low cytotoxicity.

---

\* The contents of this chapter are reproduced from: 1) Je Min Yoo<sup>†</sup>, Jin Hyoun Kang<sup>†</sup> and Byung Hee Hong<sup>\*</sup>. *Chemical Society Reviews* (2015) **44**, 4835-4852. © The Royal Society of Chemistry and 2) Je Min Yoo, Do Won Hwang and Byung Hee Hong. (2018) Graphene-Based Nanomaterials. In: Lee D. (eds) Radionanomedicine. Biological and Medical Physics, Biomedical Engineering. Springer, Cham.

Types	Structure	Optical properties	Toxicity
GOs	Sub-10 nm to micrometer size range Disrupted $sp^2$ domain with hydrophilic oxygenated group	Intrinsic photo-luminescence emission with UV excitation, and tunable emission wavelength located at the range of UV–Vis	Typically more toxic than GQDs, and cell-line dependent toxicity but no significant toxicity for both in vitro and in vivo levels at low doses
GQDs	Few nanometer (2–5 nm) small $sp^2$ domain size and oxygenated groups at edge		Generally, non-toxic (up to 1 mg ml <sup>-1</sup> ). Excretion through both renal and fecal clearance. No significant toxicity based on in vitro and in vivo studies
rGOs	Large connected $sp^2$ domains than GOs, with few hydrophilic group	A high photoluminescence quenching effect with enhanced absorption cross-section in NIR range	More toxic than hydrophilic graphene derivatives. Not-readily biodegradable without functional moieties

**Figure 1-T1.** Characteristic features of graphene-based nanomaterials.

Figure 1-T1 briefly summarizes the major features of GOs, GQDs and rGOs. In general, GOs are synthesized through the Hummer's method and GQDs can be obtained by thermo-oxidative cutting of carbon precursors including GOs. Notably, GOs and GQDs have various functional groups available for further modifications, which can be utilized for specialized purposes and further enhance their dispersibility.

### 1.1.1. Sensing Applications

In the beginning, researchers have primarily focused on utilizing the ability of GOs to quench fluorescence and the availability of their functional groups for molecular conjugation for various optical bio-sensing studies. In 2009, Lu *et al.*

successfully detected fluorophore-labeled DNA on/off the basal plane of GOs.<sup>3</sup> This work was followed by detecting other small molecules such as phosphate containing metabolites, protein kinases, trypsin and neurotransmitters with appropriate surface modulations.<sup>4-7</sup> A recent report by Mei *et al.* illustrated that logically designed GO gates could discriminate  $\text{Fe}^{3+}$  and  $\text{Fe}^{2+}$  in living cells by exploiting the difference in fluorescence quenching.<sup>8</sup> Some researchers devoted special attention to unusual characteristics of stem cell growth and differentiation on graphene film substrates, which could possibly open new venues in stem cell engineering.<sup>9,10</sup>

### **1.1.2. Therapeutic Applications**

Graphene-based nanomaterials are also known to exhibit high absorbance in the NIR region, which gave rise to novel approaches for NIR laser-triggered selective ablation of cancer cells.<sup>11,12</sup> With appropriate modifications with targeting moieties, graphene-based nanomaterials can specifically target malignant tumor cells without damaging the healthy ones. Interestingly, graphene-based nanomaterials' hydrophobic basal plane can be exploited for various synergistic therapies. Some groups attended to the fact that hydrophobic anti-cancer drugs and photodynamic agents could be easily loaded onto the basal plane of graphene-based materials through  $\pi$ - $\pi$  interactions. By combining the photothermal ablation with either chemotherapies or photodynamic therapies, therapeutic effects came to be higher.<sup>13,14</sup> NIR-responsive hyperthermia was not only utilized for the direct ablation of cells, but also employed as an external cue for controlled drug/gene delivery by disorganizing a drug-loading matrix or endocytosed vesicles by NIR laser.<sup>15-17</sup>

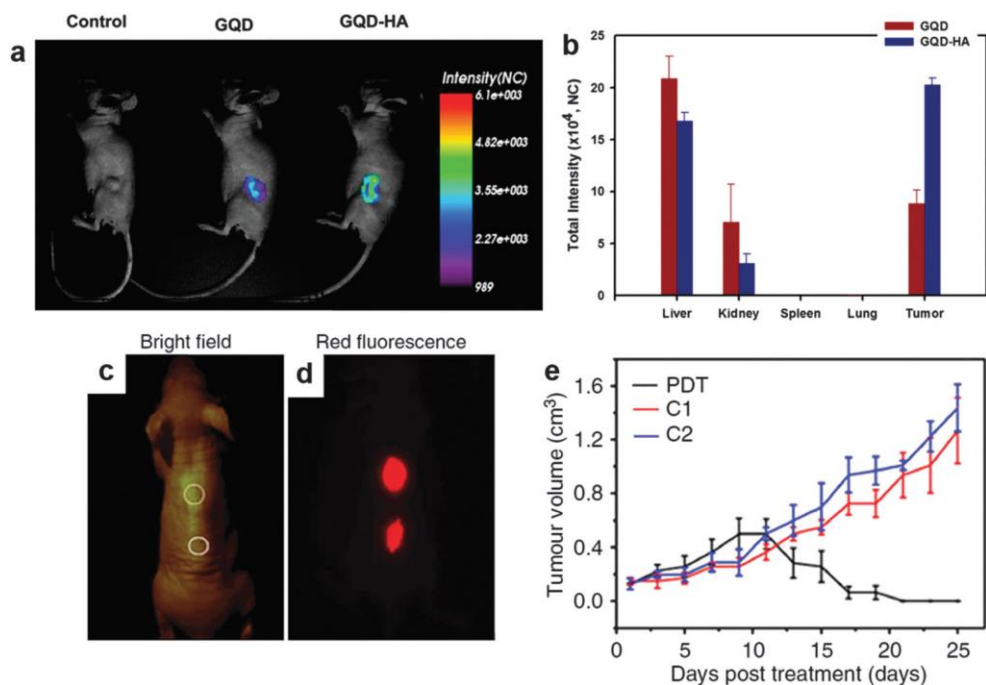


**Figure 1-1.** Graphene based *in vivo* targeting imaging agents. (a) *In vivo* fluorescence images of GQD-HA in mice after tail vein injection. (b) Fluorescence intensity from dissected organs. (c) and (d) Bright field image and *in vivo* fluorescence image after GQD injection. (e) Time-dependent tumor growth curves.

### 1.1.3. Fluorescence Bio-imaging

Numerous drug delivery strategies and direct photothermal ablation of tumor cells have been accompanied by various graphene-based platforms. Although many of these studies performed *in situ* imaging of drug delivery/therapy, most of these studies utilized coated inorganic quantum dots and other fluorescence molecules attached to graphene-based materials to visualize the phenomena. In 2013, Nahain *et al.* presented two graphene-based anti-cancer drug delivery methods using rGOs and GQDs.<sup>18,19</sup> In the case of the rGO-hyaluronic acid (HA) conjugate system (avg. size  $\cong$  200 nm), spiropyran was additionally attached as a photochromic dye for yielding a graphene-based fluorescent nanocomposite.<sup>18</sup> It

should be noted that these authors repeated similar experiments without attaching additional fluorescent materials. Instead, they utilized the intrinsic fluorescence of GQDs with an average size of 20 nm to confirm efficient targeting of GQD–HA to the desired receptors.<sup>19</sup> Successful delivery of the GQD–HA conjugate to overexpressed CD44 receptors was confirmed by obtaining fluorescence images from the tumor tissue through both *in vitro* and *in vivo* observations (Fig. 1-1). Anti-cancer treatment was subsequently administered by releasing doxorubicin under mildly acidic conditions, which was loaded onto the basal plane of GQDs. Although previously studied graphene-based therapy/imaging applications included other fluorescent molecules, researchers endeavor to exploit the luminescence of GQDs for *in situ* therapy monitoring. In 2014, Ge *et al.* incorporated a few nanometer scale GQDs in highly efficient photodynamic cancer therapy with simultaneous fluorescence imaging.<sup>20</sup> In this study, the authors successfully synthesized GQDs with a broad absorption spectrum and strong deep-red emission peaking at 680 nm. Through both *in vitro* and *in vivo* experiments, the authors clearly demonstrated that GQDs can be considered promising PDT agents, with a superior singlet oxygen quantum yield, photo- and pH-stability and even simultaneous fluorescent imaging.

While most researchers have focused on exploiting GQDs' fluorescence for monitoring *in situ* drug delivery to confirm successful targeting, Zheng *et al.* demonstrated that GQDs can be utilized as universal fluorophores that could reveal some important biological functions (Fig. 1-2).<sup>21</sup> In this study, specific labeling and dynamic tracking of insulin receptors were achieved through GQDs fluorescence of internalized and recycled insulin receptors in adipocytes. The authors tried to determine the specific functions of some relative proteins. By dynamically tracking

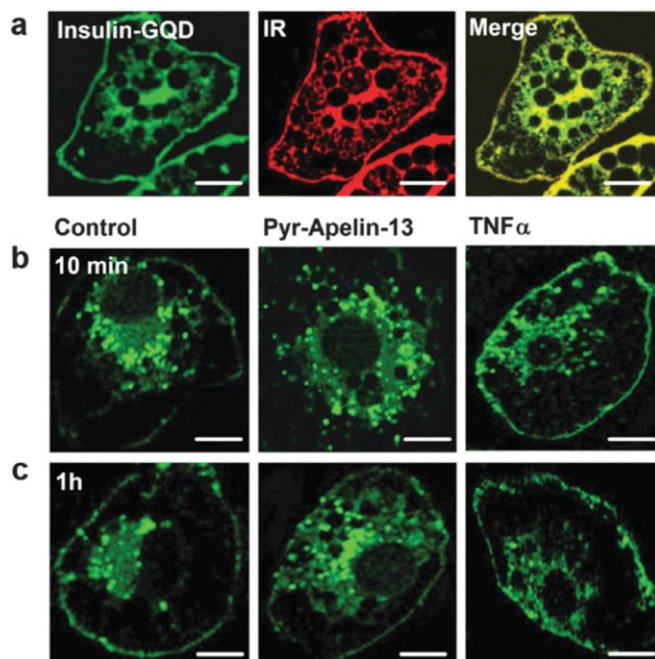


**Figure 1-2.** Dynamic tracking of protein of interest. (a) Confocal fluorescence images of insulin conjugated GQDs (green, left) or with antibodies against insulin receptor (IR) (red, middle). (b) and (c) Cellular distribution of insulin receptors after (b) 10 min or (c) 1 h incubation with insulin-GQDs. Scale bar = 10 mm.

the insulin receptors, the authors found that the internalization and recycling of insulin receptors are oppositely regulated by two distinct proteins: (1) apelin, which improves the insulin sensitivity, and (2) TNF- $\alpha$ , which enhances the insulin resistance. Although this study alone did not fundamentally change the therapeutic approaches to diabetes treatment, divulging in important cellular/subcellular functions revealed by using the GQDs fluorescence would be helpful for various future biomedical studies.

## 1.2. Preparation of Graphene-based Nanomaterials

As mentioned, GOs and GQDs are widely employed in a number of



biological applications due to the low cytotoxicity, large surface area and high dispersibility in various polar solvents. GOs are typically obtained through the Hummer's method while GQDs are prepared by thermo-oxidatively cut GOs or other carbon precursors. These graphene derivatives show outstanding optical properties, which make them suitable for versatile applications including bio-imaging. Simple modifications of GOs and GQDs make these graphene derivatives better prepared for specific biomedical applications.

### **1.2.1. Enhancing the Stability under Physiological Conditions**

GOs can be dispersed in distilled water without much aggregation for several months, but are prone to aggregation in physiological solutions which commonly contain ionic salts. One of the strategies for enhancing stability under biological conditions is introducing biocompatible hydrophilic polymers and reducing the size of GOs. Although the synthesized GOs exhibit wide size distributions, the average size can be reduced by sonication. Many recent reports indicate that the sonication assisted modifications reduce the average size of GOs owing to the high sonication energy, and large GO particles can be broken down into much smaller ones, as small as 10 nm.<sup>22</sup> Since small sized GOs show improved dispersion stability in polar solvents including physiological solution,<sup>23</sup> sub-500 nm GOs were commonly used in bio-imaging. For modification with hydrophilic polymers, polyethylene glycol (PEG) is one of the most preferably used polymers. Sun *et al.* grafted branched PEGs on GOs for enhancing the dispersion stability in biological buffers and further application as imaging agents.<sup>22</sup> In that study, PEGs were bonded to GOs through the reaction with epoxy and carboxylic acid groups achieving PEGylated nano-sized GOs, which showed

exceptional stability in phosphate buffered saline (PBS). Many studies used PEGs to achieve high stability even in solutions with high concentrations of salts (B10% NaCl).<sup>24</sup> Other biocompatible hydrophilic polymers such as polyamido amine (PAMAM), dextran (DEX) and polyacrylic acid (PAA) also can be used as a stabilizer by covalent modification methods.<sup>25–27</sup>

### 1.2.2. Reduction of GOs

rGOs have been considered for photothermal therapy and photoacoustic imaging agents due to their high absorption cross-section in the NIR region. GOs can be reduced via photothermal,<sup>28</sup> electrochemical,<sup>29</sup> or chemical reduction,<sup>30</sup> but chemical reduction is considered the easiest way to obtain rGOs. In 2007, Stankovich *et al.* demonstrated that hydrazine can reduce GOs dispersed in water.<sup>30</sup> Ever since, hydrazine has been widely used to produce rGOs. However, owing to the toxicity of hydrazine and insolubility of rGOs, further surface modifications have also been performed afterwards. Contrary to GOs, covalent surface modifications cannot drastically change the properties of rGOs as only a negligible amount of carboxyl and epoxy groups are present. Instead, non-covalent approaches using the  $\pi$ – $\pi$  interaction between the basal plane and aromatic molecules are used to modulate the surface properties of rGOs based on the strong van der Waals interaction. To obtain highly dispersible rGOs, PEGs terminated with hydrophobic alkyl chains can be attached, as suggested by the work of Shi *et al.*<sup>31</sup>

In recent years, various proteins are employed as a reducing agent and stabilizer of GOs for better biocompatibility and stability. Liu *et al.* demonstrated that GOs can be reduced by gelatin and well-dispersed in physiological solutions.<sup>32</sup>

The resulting gelatin-rGO nanosheets were also internalized in cells without considerable cytotoxicity, and used as effective *in vitro* imaging agents. Sheng *et al.* demonstrated that bovine serum albumin (BSA) can reduce GOs and simultaneously behave as a surfactant, producing hydrophilic rGOs which can be successfully used as *in vivo* imaging agents.<sup>33</sup>

### **1.3. Toxicity of Graphene-based Nanomaterials**

Although CNTs and graphene-based materials are some of the most widely studied nanoscale  $sp^2$  carbon allotropes with very similar chemical compositions, recent studies have observed entirely different levels of toxicities from these two classes of materials.<sup>34,35</sup> Unlike CNTs, most studies have generally agreed on the negligible cytotoxicity of graphene-based materials.

#### **1.3.1. *In vitro* Toxicity of Graphene-based Nanomaterials**

Over the last few years, several groups investigated cellular internalization and *in vitro* cytotoxicity of functionalized graphene derivatives: GOs and GQDs using different types of mammalian cells. These reports generally confirmed low cytotoxicity and relatively high cellular uptake, which makes graphene-based materials suitable for various biomedical applications.<sup>36-41</sup> Nevertheless, some researchers argued that the cytotoxicity of a few hundred nanometer or micro-meter sized GOs is much higher than that of GQDs, which should not be disregarded in biomedical applications.<sup>37,38</sup> In particular, some studies indicated that GOs and GO-based nanoplatelets are related to severe cytotoxicity and lung diseases.<sup>42,43</sup> Other researchers revealed heterogeneous cell-

specific cytotoxicity of GOs by performing cytotoxicity screening of GOs on multiple different cell lines.<sup>44</sup> In general, the cytotoxicity of graphene-based materials was found to be strongly related to the size of particles, which could partially explain lower cytotoxicity of a few nano-meter sized GQDs over a few micro-meter sized GOs.<sup>38,43,45</sup> On the contrary, Akhavan *et al.*, have repeatedly argued that the cytotoxicity of graphene-based materials is independent of size, but direct interaction of the sharp edges of graphene with the cell membranes is more likely a mechanism underlying the observed cytotoxicity.<sup>46,47</sup> In other words, the authors believe that nano-sized GOs can also be lethal to mammalian cells. Thus, detailed toxicity mechanisms pertaining to the size and shape of graphene-based materials are still uncertain and further studies seem unavoidable.

In addition, the effects of graphene functionalization in cell membrane permeability and cytotoxicity were studied by many researchers. The authors commonly discussed that covalently attaching hydrophilic molecules such as polyethylene glycol (PEG) to the edges of graphene enhances solubility and biocompatibility in a biological environment.<sup>22</sup> Some authors investigated possible toxicity effects of the functional groups by modifying them with  $-\text{COOH}$ ,  $\text{NH}_2$ ,  $\text{CO}-\text{N}(\text{CH}_3)_2$ , and  $-\text{PEG}$ .<sup>41,48</sup> Quantitative data analysis showed no distinct toxicity changes among these GQD variants, while the cell membrane permeability increased respectively in the order of  $-\text{PEG}$ ,  $-\text{OH}$ , and  $-\text{NH}_2$ .<sup>49</sup> These results are encouraging for researchers who endeavor to employ modified graphene derivatives as they all exhibit very low cytotoxicity.<sup>50</sup> In 2011, Sasidharan *et al.* studied distinct behaviors between pristine/hydrophobic graphene and carboxylated/hydrophilic graphene in biological environments. Compared to pristine graphene, carboxylated graphene pacify hydrophobic interaction with the

cell membrane and the associated toxic effects such as the deformation of cell membrane and increased intracellular ROS level and subsequent apoptosis.<sup>39</sup> Indeed, graphene functionalization plays a vital role not only in cell-nanoparticle interactions, but also in enzyme-catalyzed biodegradation, which will be discussed in a later paragraph.

### **1.3.2. *In vivo* Toxicity of Graphene-based Nanomaterials**

Besides the *in vitro* toxicity studies addressed above, many authors have explored *in vivo* bio-distribution and toxicology of graphene-based materials recently. In 2010, Yang *et al.* discussed the long-term *in vivo* pharmacokinetics and bio-distribution of PEGylated <sup>125</sup>I-labeled nano-graphene sheets (NGS) with systemic toxicology examination.<sup>51</sup> The radioactivity levels of <sup>125</sup>I-NGS-PEG were measured in the blood and many different organs over time after intravenous injection. Overall, they found persistently decreased radioactivity levels of <sup>125</sup>I-NGS-PEG in most organs. They presumed that small NGS-PEG particles may be cleared out by renal or fecal excretion. The authors also investigated long-term *in vivo* toxicology over 3 months by carrying out blood biochemistry and hematology analysis. Mice injected with 20 mg/kg NGS-PEG were sacrificed at different periods of time, and all parameters from the blood biochemistry and hematological data did not indicate any appreciable toxicity. In 2013, the same group carried out *in vivo* bio-distribution and toxicology studies of functionalized nano-GOs by administering it through two other major routes: oral feeding and intraperitoneal (i.p.) injection.<sup>36</sup> They revealed that oral administration induced no obvious tissue uptake, while i.p. injection led to high accumulation of nano-GOs in the RES system over long periods of time. In spite of the results obtained through the i.p.

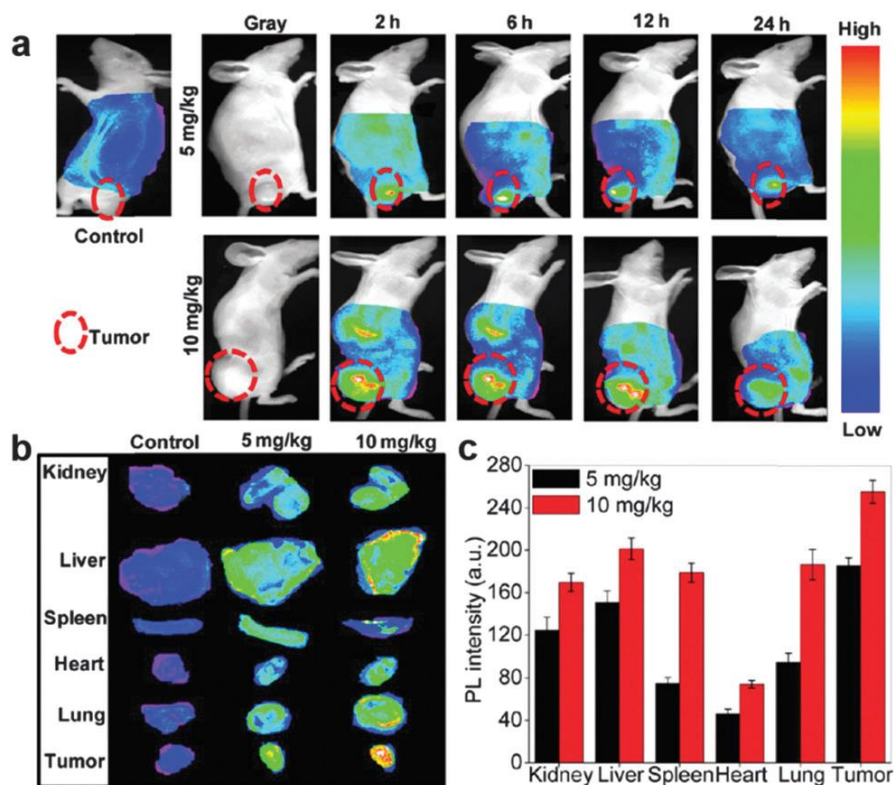


**Figure 1-3.** *In vivo* imaging and bio-distribution of the carboxylated GQDs. (a) The *in vivo* imaging of KB tumor bearing mice after intravenous injection of GQDs (5 and 10 mg/kg). (b) and (c) *ex vivo* images and quantitative distribution of isolated organs of mice at 24 h after injection.

injection, they found that both routes did not result in significant toxicity to the treated animals.

In 2014, Nurunnabi *et al.* reported *in vivo* bio-distribution and toxicity of carboxylated GQDs by intravenously injecting them into mice.<sup>52</sup> The accumulation and potential toxicity were tested by performing a long-term serum biochemical analysis and histological evaluations. Overall, the study revealed no serious *in vivo* toxicity and GQDs were mainly found in the liver, spleen, lung, kidney, and tumor sites (Fig. 1-3). Further study confirmed that GQDs did not yield any appreciable organ damage or lesions in mice that were treated with GQDs by administering 5

mg/kg or 10 mg/kg dosages for 21 days. These results were followed by similar conclusions of *in vivo* bio-distribution studies, illustrating fast clearance of GQDs from kidneys without significant accumulation in the main organs.<sup>44</sup> Results of these biocompatibility studies suggest that GQDs can be used in clinical applications in the near future. However, these results also indicate that high doses of GOs can be toxic and have a lethal outcome, on good agreement with the results of *in vitro* studies.

### **1.3.3. Biodegradation of Graphene-based Nanomaterials**

As much as various parameters of *in vitro* and *in vivo* toxicity studies are important, thorough understandings on oxidation–bio-degradation processes of graphene-based materials are crucial for universal and beneficial applications. In 2011, Kotchey *et al.* reported enzyme-catalyzed oxidation of GOs and rGO by incubating each solution with low concentrations of hydrogen peroxide and horseradish peroxidase (HRP).<sup>53</sup> Strikingly, the study revealed that the degree of functionalization is directly correlated with the degree of enzyme-catalyzed oxidation. Results from Raman spectroscopy, transmission electron microscopy (TEM) and atomic force microscopy (AFM) confirmed that mild enzymatic oxidation with HRP induced the formation of holey graphene oxide, which eventually resulted in fully oxidized debris of GO flakes (Fig. 1-4). On the other hand, incubation of rGOs with HRP did not make any significant changes in terms of enzymatic oxidation. The authors deduced that the presence of functional groups on GOs induced looser binding with HRP and allowed the enzyme to be more dynamic; the catalytic heme site of HRP was thus brought in proximity of GOs. On the other hand, more hydrophobic rGOs made tighter binding with HRP without

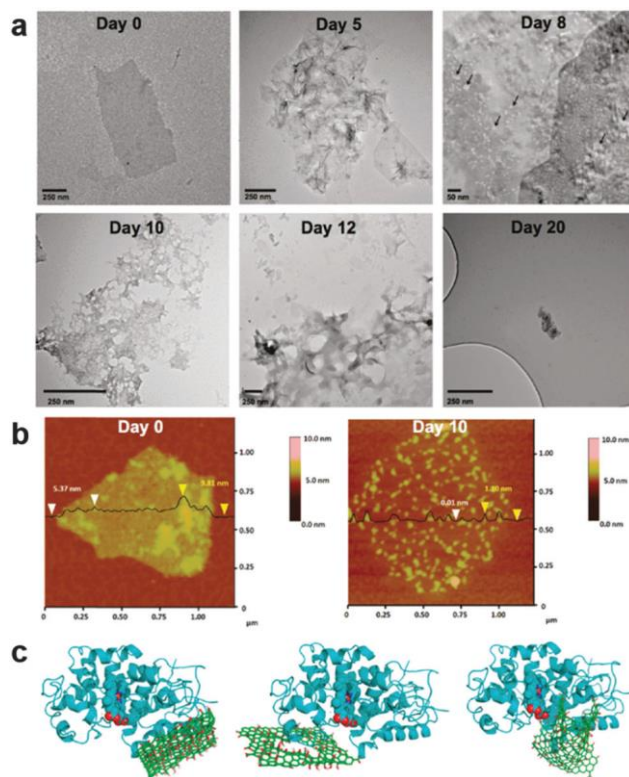


**Figure 1-4.** Enzymatic oxidation of GOs. (a) TEM images of GOs incubated with horse radish peroxidase (HRP). (b) AFM images with GOs incubated with HRP. (c) Simulated docking between GOs and HRP.

making contacts with the catalytic heme site. In 2012, the same group reported thorough investigation on the enzyme-catalyzed degradation of CNMs using HRP and myeloperoxidase (MPO).<sup>54</sup> The report verified promising aspects of functionalized CNMs for *in vivo* applications as they are presumably biodegradable by intracellular enzymes with peroxidase activity such as human MPO (hMPO). Nevertheless, it should be noted that the experimental results are not directly correlated with actual biodegradation in the human body as the physiological hMPO levels are generally more diluted than the experimental conditions. In addition, the oxidative debris of GO nanoflakes could be another possible source of toxicity.



## 1.4. Perspectives and Other Applications

The promising aspects of graphene derivatives for biological and medical applications are: availability to produce various forms of graphene derivatives for different studies, high dispersibility upon conjugating diverse molecules and possibility to deliver drugs with specific targeting ability. The strong intrinsic Raman scattering signals can be utilized for Raman spectroscopy-based analysis, and increased NIR absorbance of the reduced version of derivatives is advantageous for successful relevant investigations. The fluorescence characteristics of GOs and GQDs can be tuned by modifying functional groups, and enhanced QY makes fluorescence bio-imaging another plausible method. Although CNTs exhibit some useful properties and have been considered for biological applications early on, the difficult separation steps may hinder large-scale production of well-defined CNTs. On the other hand, the dispersed forms of graphene are more applicable to mass production. Solvo-thermal synthesis employing sodium had already achieved gram-scale graphene,<sup>55</sup> and shear exfoliation in NMP can be readily used for industry-scale production.<sup>56</sup> In addition, in contrast to the CNTs, graphene does not require further purification steps, which present a hurdle for CNT commercialization. The produced graphene can be further oxidized under oxidative conditions for introducing additional oxygenated functional groups, and functional ligands and biomolecules can be incorporated for increasing graphene's water dispersibility and targeting, which is desired for biomedical applications.

Among many graphene derivatives, CVD graphene exhibits high electron conductivity and fast heat dissipation. Low density of defects could serve to

perfectly trap liquid for preventing vaporization under high vacuum or ultra-high vacuum conditions, which are the mandatory conditions for electron microscopy analysis. Thus, graphene can be utilized as an atomically thin window for *in situ* electron microscopy for liquid state samples, including various biomolecules and tissues. In addition, this single-atom thick film would make conformal contacts with non-conductive samples assuring the details of surface information. Thus, it could be employed as a novel conductive coating material for transmission electron microscopy (TEM) and scanning electron microscopy (SEM) analysis where noble metals such as platinum (Pt) are currently used.

In this chapter, recent biomedical applications, preparation and toxicity of graphene-based nanomaterials were reviewed. As mentioned, graphene has a number of exceptional properties for different biomedical studies including low toxicity and easily conjugatable functional groups. In addition, various forms of graphene also possess other remarkable properties including high Raman scattering intensity, large absorption cross section in the NIR region, and sharp photoacoustic contrast with the NIR incident beam. Based on the status of current research, it is expected that graphene-based nanomaterials will play vital roles in a number of important biomedical studies in the near future.

## 1.5. References

1. K. S. Novoselov, A. K. Geim, S. V. Morozov, D. Jiang, Y. Zhang, S. V. Dubonos, I. V. Grigorieva and A. A. Firsov, *Science*, 2004, **306**, 666.
2. A. K. Geim and K. S. Novoselov, *Nat. Mater.*, 2007, **6**, 183.
3. C.-H. Lu, H.-H. Yang, C.-L. Zhu, X. Chen and G.-N. Chen, *Angew. Chem., Int. Ed.*, 2009, **48**, 4785.
4. J.-J. Liu, X.-L. Zhang, Z.-X. Cong, Z.-T. Chen, H.-H. Yang and G.-N. Chen, *Nanoscale*, 2013, **5**, 1810.
5. Y. Wang, L. Zhang, R.-P. Liang, J.-M. Bai and J.-D. Qiu, *Anal. Chem.*, 2013, 85, 9148.
6. X. Li, S. Zhu, B. Xu, K. Ma, J. Zhang, B. Yang and W. Tian, *Nanoscale*, 2013, **5**, 7776.
7. S.-J. Jeon, S.-Y. Kwak, D. Yim, J.-M. Ju and J.-H. Kim, *J. Am. Chem. Soc.*, 2014, **136**, 10842.
8. Q. Mei, C. Jiang, G. Guan, K. Zhang, B. Liu, R. Liu and Z. Zhang, *Chem. Commun.*, 2012, **48**, 7468.
9. W. C. Lee, C. H. Y. X. Lim, H. Shi, L. A. L. Tang, Y. Wang, C. T. Lim and K. P. Loh, *ACS Nano*, 2011, **5**, 7334.
10. S. Y. Park, J. Park, S. H. Sim, M. G. Sung, K. S. Kim, B. H. Hong and S. Hong, *Adv. Mater.*, 2011, **23**, H263.
11. J. T. Robinson, S. M. Tabakman, Y. Liang, H. Wang, H. S. Casalongue, D. Vinh *et al.*, *J. Am. Chem. Soc.*, 2011, **133**, 6825.
12. B. Tian, C. Wang, S. Zhang, L. Feng, Z. Liu, *ACS Nano*, 2011, **5**, 7000.
13. C. Jang, J.H. Lee, A. Sahu, G. Tae, *Nanoscale*, 2015, **7**, 18584.
14. L. Zhou, L. Zhou, S. Wei, X. Ge, J. Zhou, H. Jiang *et al.*, *J. Photochem. Photobiol.*, 2014, **B 135**, 7.
15. H. Kim, W.J. Kim, *Small*, 2014, **10**, 117.
16. P. Matteini, F. Tatini, L. Cavigli, S. Ottaviano, G. Ghini, R. Pini, *Nanoscale*,

- 2014, **6**, 7947.
17. V. Shanmugam, S. Selvakumar, C. -S. Yeh, *Chem. Soc. Rev.*, 2014, **43**, 6254.
  18. A.-A. Nahain, J.-E. Lee, J. H. Jeong and S. Y. Park, *Biomacromolecules*, 2013, **14**, 4082.
  19. A.-A. Nahain, J.-E. Lee, I. In, H. Lee, K. D. Lee, J. H. Jeong and S. Y. Park, *Mol. Pharmaceutics*, 2013, **10**, 3736.
  20. J. Ge, M. Lan, B. Zhou, W. Liu, L. Guo, H. Wang, Q. Jia, G. Niu, X. Huang, H. Zhou, X. Meng, P. Wang, C.-S. Lee, W. Zhang and X. Han, *Nat. Commun.*, 2014, **5**, 4596.
  21. X. T. Zheng, A. Than, A. Ananthanaraya, D.-H. Kim and P. Chen, *ACS Nano*, 2013, **7**, 6278.
  22. X. Sun, Z. Liu, K. Welsher, J. T. Robinson, A. Goodwin, S. Zaric and H. Dai, *Nano Res.*, 2008, **1**, 203.
  23. Z. Liu, J. T. Robinson, X. Sun and H. Dai, *J. Am. Chem. Soc.*, 2008, **130**, 10876.
  24. S. Zhu, H. Zhen, Y. Li, P. Wang, X. Huang and P. Shi, *J. Nanopart. Res.*, 2014, **16**, 2530.
  - 25 P. S. Wate, S. S. Banerjee, A. Jalota-Badhwar, R. R. Mascarenhas, K. R. Zope, J. Khandare and R. D. K. Misra, *Nanotechnology*, 2012, **23**, 415101.
  26. S. A. Zhang, K. Yang, L. Z. Feng and Z. Liu, *ACS Nano*, 2011, **49**, 4040.
  27. G. Gollavelli and Y.-C. Ling, *Biomaterials*, 2012, **33**, 2532.
  28. L. J. Cote, R. Cruz-Silva and J. X. Huang, *J. Am. Chem. Soc.*, 2009, **131**, 11027.
  29. G. K. Ramesha and S. Sampath, *J. Phys. Chem. C*, 2009, **113**, 7985.
  30. S. Stankovich, D. A. Dikin, R. D. Piner, K. A. Kohlhaas, A. Kleinhammes, Y. Jia, Y. Wu, S. T. Nguyen and R. S. Ruoff, *Carbon*, 2007, **45**, 1558.
  31. S. Shi, K. Yang, H. Hong, H. F. Valdovinos, T. R. Nayak, Y. Zhang, C. P. Theuer, T. E. Barnhart, Z. Liu and W. Cai, *Biomaterials*, 2013, **34**, 3002.
  32. K. Liu, J.-J. Zhang, F.-F. Cheng, T.-T. Zheng, C. Wang and J.-J. Zhu, *J. Mater. Chem.*, 2011, **21**, 12034.
  33. Z. Sheng, L. Song, J. Zheng, D. Hu, M. He, M. Zheng, G. Gao, P. Gong, P.

- Zhang, Y. Ma and L. Cai, *Biomaterials*, 2013, **34**, 5236.
34. A. M. Jastrzebska, P. Kurtycz and A. R. Olszyna, *J. Nanopart. Res.*, 2012, **14**, 1320.
  35. C. Fisher, A. E. Rider, Z. J. Han, S. Kumar, I. Levchenko and K. Ostrikov, *J. Nanomater.*, 2012, **2012**, 315185.
  36. K. Yang, H. Gong, X. Shi, J. Wan, Y. Zhang and Z. Liu, *Biomaterials*, 2013, **34**, 2787.
  37. Y. Chong, Y. Ma, H. Shen, X. Tu, X. Zhou, J. Xu, J. Dai, S. Fan and Z. Zhang, *Biomaterials*, 2014, **35**, 5041.
  38. H. Zhang, C. Peng, J. Yang, M. Lv, R. Liu, D. He, C. Fan and Q. Huang, *ACS Appl. Mater. Interfaces*, 2013, **5**, 1761.
  39. A. Sasidharan, L. S. Panchakarla, P. Chandran, D. Menon, S. Nair, C. N. R. Rao and M. Koyakutty, *Nanoscale*, 2011, **3**, 2461.
  40. C. Wu, C. Wang, T. Han, X. Zhou, S. Guo and J. Zhang, *Adv. Healthcare Mater.*, 2013, **2**, 1613.
  41. X. Yuan, Z. Liu, Z. Guo, Y. Ji, M. Jin and X. Wang, *Nanoscale Res. Lett.*, 2014, **9**, 108.
  42. K. Wang, J. Ruan, H. Song, J. Zhang, Y. Wo, S. Guo and D. Cui, *Nanoscale Res. Lett.*, 2011, **6**, 1.
  43. A. Schinwald, F. A. Murphy, A. Jones, W. MacNee and K. Donaldson, *ACS Nano*, 2012, **6**, 736.
  44. S. M. Chowdhury, G. Lalwani, K. Zhang, J. Y. Yang, K. Neville and B. Sitharaman, *Biomaterials*, 2013, **34**, 283.
  45. L. De Marzi, L. Ottaviano, F. Perrozzi, M. Nardone, S. Santucci, J. De Lapuente, M. Borrás, E. Treossi, V. Palermo and A. Poma, *J. Biol. Regul. Homeostatic Agents*, 2014, **28**, 281.
  46. O. Akhavan, E. Ghaderi and A. Akhavan, *Biomaterials*, 2012, **33**, 8017.
  47. O. Akhavan and E. Ghaderi, *ACS Nano*, 2010, **4**, 5731.
  48. W. Kong, J. Liu, R. Liu, H. Li, Y. Liu, H. Huang, K. Li, J. Liu, S.-T. Lee and Z.

- Kang, *Nanoscale*, 2014, **6**, 5116.
49. C. Kirchner, T. Liedl, S. Kudera, T. Pellegrino, A. M. Javier, H. E. Gaub, S. Stoilzle, N. Fertig and W. J. Parak, *Nano Lett.*, 2005, **5**, 331.
50. L. Yan, F. Zhao, S. Li, Z. Huc and Y. Zhao, *Nanoscale*, 2011, **3**, 362.
51. K. Yang, J. Wan, S. Zhang, Y. Zhang, S.-T. Lee and Z. Liu, *ACS Nano*, 2011, **5**, 516.
52. M. Nurunnabi, Z. Khatun, K. M. Huh, S. Y. Park, D. Y. Lee, K. J. Cho and Y.-K. Lee, *ACS Nano*, 2013, **7**, 6858.
53. G. P. Kotchey, B. L. Allen, H. Vedala, N. Yanamala, A. A. Kapralov, Y. Y. Tyurina, J. Klein-Seetharaman, V. E. Kagan and A. Star, *ACS Nano*, 2011, **5**, 2098.
54. G. P. Kotchey, S. A. Hasan, A. A. Kapralov, S. H. Ha, K. Kim, A. A. Shvedova, V. E. Kagan and A. Star, *Acc. Chem. Res.*, 2012, **45**, 1770.
55. M. Choucair, P. Thordarson and J. A. Stride, *Nat. Nanotechnol.*, 2008, **4**, 30.
56. K. R. Paton, *et al.*, *Nat. Mater.*, 2014, **13**, 6242.

## ***Chapter 2***

# ***Catalytic Degradation of Phenols by Recyclable CVD Graphene Films***

### **1.1. Abstract**

Phenolic compounds are deemed as the major industrial pollutants as they are both mutagenic and carcinogenic. To destroy these substances, ferrous ion-based catalysts have been widely employed for oxidative destruction through advanced oxidation processes (AOPs). These agents, however, inevitably show several drawbacks including the need for pH adjustment and further purification steps to remove residual salts. Here we report the use of a chemical vapour deposition (CVD) graphene film as a novel metal-free catalyst for the AOP-based degradation of phenols in aqueous solution, which does not require additional steps for salt removal nor external energy to activate the process. We have also verified that the catalytic activity is strongly dependent on the surface area of the graphene film and the degradation efficiency can be markedly improved by exploiting an array of multiple graphene films. Finally, the recyclability of the graphene film has been validated by performing repetitive degradation tests to ensure its practical use.

---

\* This chapter is reproduced from: Je Min Yoo<sup>†</sup>, Baekwon Park<sup>†</sup>, Sang Jin Kim, Yong Seok Choi, Sungmin Park, Eun Hye Jeong, Hyukjin Lee<sup>\*</sup> and Byung Hee Hong<sup>\*</sup>. *Nanoscale* (2018) **10**, 5840-5844. © The Royal Society of Chemistry

## 1.2. Introduction

Phenol and its derivatives are important materials in many industries, but are also hazardous and potentially mutagenic and/or carcinogenic.<sup>1-3</sup> For such reasons, destroying organic pollutants in an aquatic environment has been one of the major foci in the field of environmental medicine and wastewater treatment. To date, oxidative destruction of phenolic compounds has been carried out mostly through advanced oxidation processes (AOPs), which exploit the generated secondary radicals as powerful oxidants under aqueous conditions.<sup>4-6</sup> To facilitate the processes while minimising disadvantages, a number of different catalysts including ferrous ion-based Fenton's reagents have been widely employed. However, these agents necessitate further steps to remove residual salts and are optimised under relatively harsh conditions such as low pH. In addition, other candidates without ferrous ions predominantly demand external energies including UV light and electricity, which complicates their universal applications.<sup>7-10</sup>

In this communication, we propose the application of a monolayer graphene film as a novel catalyst to degrade phenols through the AOP. Graphene has gained much attention in diverse fields of study due to many of its outstanding physical, chemical and electrical properties, as well as its exceptional ability to donate or withdraw electrons.<sup>11-14</sup> We have thus inferred that a graphene film can be utilised to generate hydroxyl radicals from hydrogen peroxide ( $\text{H}_2\text{O}_2$ ) through immediate redox reactions, where the generated radicals can be exploited to oxidatively destroy phenols without any additional treatments.



### 1.3. Results and Discussion

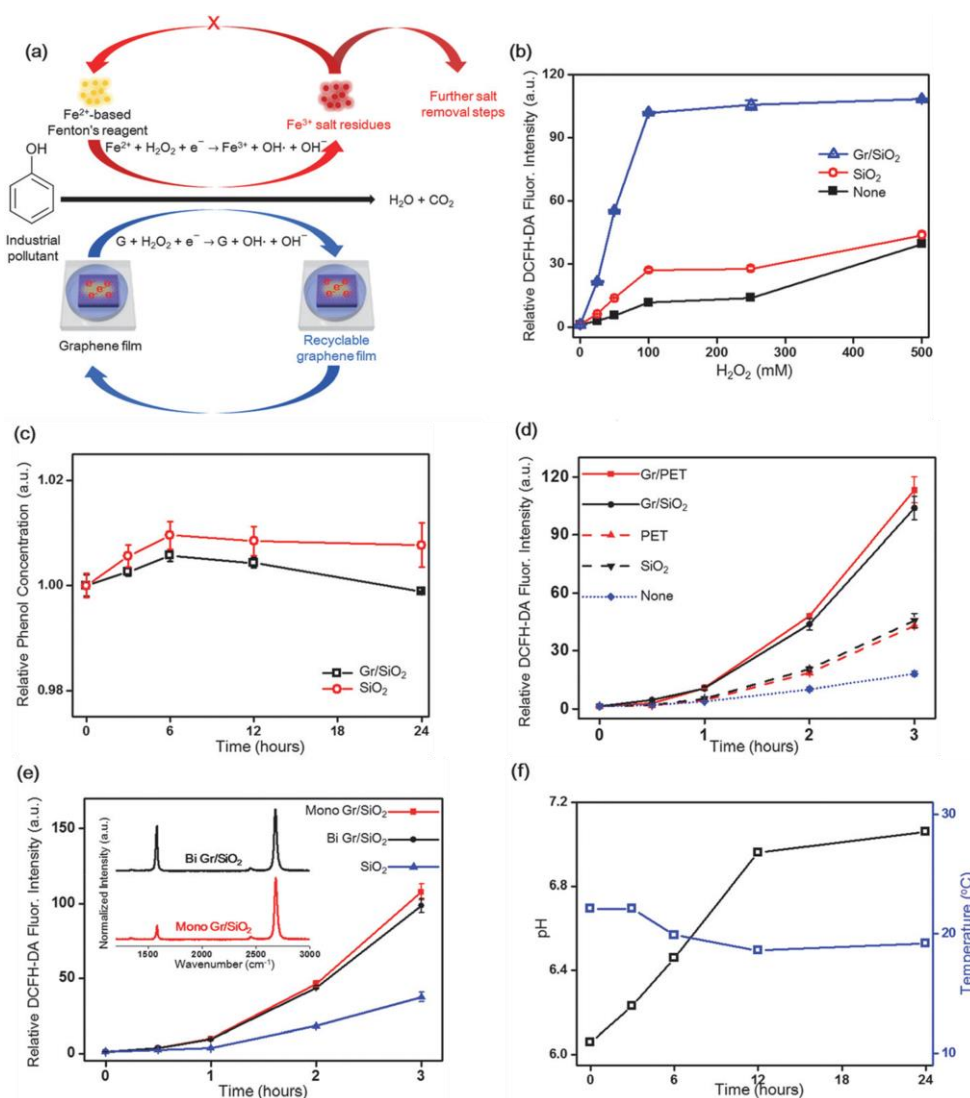


**Figure 2-1.** (a) Schematic representation of the conventional phenol degradation method using  $\text{Fe}^{2+}$ -based Fenton's reagent (top) and the novel method with a recyclable graphene film (bottom). (b) Representative DCFH-DA fluorescence intensity (2  $\mu\text{M}$ ) with respect to increasing  $\text{H}_2\text{O}_2$  concentrations in the presence of 1  $\text{cm}^2$  Gr/SiO<sub>2</sub> (blue), 1  $\text{cm}^2$  SiO<sub>2</sub> only (red), and non-treated (black). (c) Preliminary surface adsorption test of phenols (1 mM) in the presence (black) and absence (red) of 1  $\text{cm}^2$  graphene film. (d) Representative DCFH-DA fluorescence intensity (2  $\mu\text{M}$ ) in the presence of 1  $\text{cm}^2$  Gr/PET (red line), Gr/SiO<sub>2</sub> (blue line), PET only (red dot), SiO<sub>2</sub> only (black dot), and non-treated (blue dot) and (e) mono- (red), bilayer Gr/SiO<sub>2</sub> (black) and SiO<sub>2</sub> only (blue) with the respective Raman spectra. (f) Time-dependent pH (black) and temperature (blue) changes in the presence of 1  $\text{cm}^2$  graphene film,  $\text{H}_2\text{O}_2$  (100 mM), and phenols (1 mM).

For the study, a high quality monolayer graphene film was synthesized through the chemical vapour deposition (CVD) method (Fig. 2-S1), and transferred onto a silicon substrate (Gr/SiO<sub>2</sub>).<sup>15,16</sup> Ideally, graphene facilitates the AOP-mediated destruction of phenols in an analogous manner to the conventional ferrous ion-based catalysts, but this would be more advantageous in multiple aspects: (i) further steps for salt removal would not be necessary, (ii) the optimal activity is not restricted to low pH, (iii) no input of external energy is required and (iv) the film is recyclable as long as graphene is not severely damaged and H<sub>2</sub>O<sub>2</sub> can be replenished (Fig. 2-1 a).

To investigate the ability of the graphene film to generate hydroxyl radicals from H<sub>2</sub>O<sub>2</sub>, the fluorescence intensity of 2',7'-dichlorofluorescein diacetate (DCFH-DA, 2 μM) was measured at different H<sub>2</sub>O<sub>2</sub> concentrations. DCFH-DA is one of the most common fluorescent probes for the detection of reactive oxygen species (ROS),<sup>17,18</sup> where its fluorescence intensity corresponds to the levels of ROS. Gr/SiO<sub>2</sub> and bare SiO<sub>2</sub>, changes in the fluorescence intensity were monitored. While the non-treated and SiO<sub>2</sub> only groups respectively resulted in a 12-fold and 27-fold increase in the fluorescence intensity, Gr/SiO<sub>2</sub> elicited a 102-fold increase with 100 mM H<sub>2</sub>O<sub>2</sub> (Fig. 2-1 b).

The difference in the fluorescence intensity solely arose from the presence of a 1 cm<sup>2</sup> monolayer graphene sheet, which apparently took part in generating secondary radicals (i.e. hydroxyl radicals, OH·) from H<sub>2</sub>O<sub>2</sub>; the radicals' strong oxidising potential is reflected by the dramatic fluorescence intensity increment. Indeed, previous reports including density functional theory (DFT) studies have explored the H<sub>2</sub>O<sub>2</sub> reduction reaction (HPRR) on graphene, through which powerful secondary radicals can be generated *en route* to its complete reduction to

water.<sup>19,20</sup> More specifically, ambient  $\text{H}_2\text{O}_2$  molecules are transiently adsorbed onto the surface of the graphene film mainly through the van der Waals force. Upon the spontaneous physisorption, breakage of the O–O bond is replaced by the formation of the C–O bond with graphene, where the adsorbed  $\text{OH}\cdot$  on graphene plays the role of a strong oxidant against the surrounding targets like DCFH-DA.<sup>21,22</sup>

Unlike the temporary adsorption of  $\text{H}_2\text{O}_2$  molecules, the molecular adsorption of phenols on the graphene film may hinder their degradation process as these ring compounds are known to interact with graphene through hydrophobic interactions.<sup>22</sup> On account of this potential issue, the adsorption of phenols on graphene was preliminarily tested by incubating  $1\text{ cm}^2$  graphene in a  $1\text{ mM}$  phenol solution (Fig. 2-1 c). As shown from the results, practically no phenol molecules were adsorbed onto the graphene films. It can thus be inferred that the  $\pi$ – $\pi$  interactions between phenols and graphene are either only transient or negligible, which can be supported by the previous literature that re-discussed the  $\pi$ -stacking in general.<sup>23</sup>

To investigate the effects of the underlying substrate and the number of graphene sheets on the catalytic performance, monolayer graphene on flexible polyethylene terephthalate (PET) and bilayer graphene on  $\text{SiO}_2$  were prepared (Fig. 2-1 d and e). As shown in Fig. 2-1 d, the substrate change resulted in only insignificant differences in the catalytic effect, as assessed by DCFH-DA fluorescence assay. Thus, Gr/ $\text{SiO}_2$  was exploited for all following assessments to facilitate relevant analyses including Raman and XPS. In like manner, mono- and bilayer graphene, which exhibited characteristic Raman 2D/G ratios of 4.27 and 1.15, did not show critical changes in the catalytic effects (Fig. 2-1 e).<sup>24</sup> The result is in accordance with a previous study on the electron transfer of mono- and bilayer

graphene, which practically show no clear distinction.<sup>25</sup>

In addition, the time-dependent pH and temperature changes were monitored by incubating 1 cm<sup>2</sup> Gr/SiO<sub>2</sub> and 1 mM phenols with 100 mM H<sub>2</sub>O<sub>2</sub> under ambient conditions (Fig. 2-1 f). Notably, the pH started at 6.06 and gradually increased with time, and saturated at 7.06 after 24 hours of incubation. The gradual pH increment can be attributed to the progressive consumption of phenols and H<sub>2</sub>O<sub>2</sub>, which are both weakly acidic, during the generation of hydroxyl radicals.<sup>26,27</sup> H<sub>2</sub>O<sub>2</sub> is exploited for the production of hydroxyl radicals and phenols are degraded as a result of the process. Collectively, the final pH of this graphene-catalysed process reaches that of water, which is far more advantageous than ferrous ion-based catalysts that are optimally activated in the pH range of 3–4.<sup>5</sup> It should also be noted that there were no significant changes in the temperature during the course of phenol degradation except for the changes caused by the surrounding temperature.

The effect of graphene-induced radicals on the degradation of phenols was subsequently investigated. Note that the concentration of H<sub>2</sub>O<sub>2</sub> was adjusted to 100 mM in all following assessments as the fluorescence intensity for the Gr/SiO<sub>2</sub> group was practically saturated from 100 mM onwards. After incubating 1 mM phenols with 1 cm<sup>2</sup> Gr/SiO<sub>2</sub> for 24 hours, the sample was analysed by time-resolved ion-exchange high performance liquid chromatography (HPLC) (Fig. 2-2 a). Besides the standard HPLC signal of phenol, which displays its characteristic peak at 68.56 minutes (Fig. 2-2 b), four other distinct signals were newly observed. To identify the substances designated by the emerged peaks, a HPLC-coupled organic acid analyser with a proton column and ultraviolet (UV) absorption spectroscopy were exploited. Foremost, we sought to characterise the three

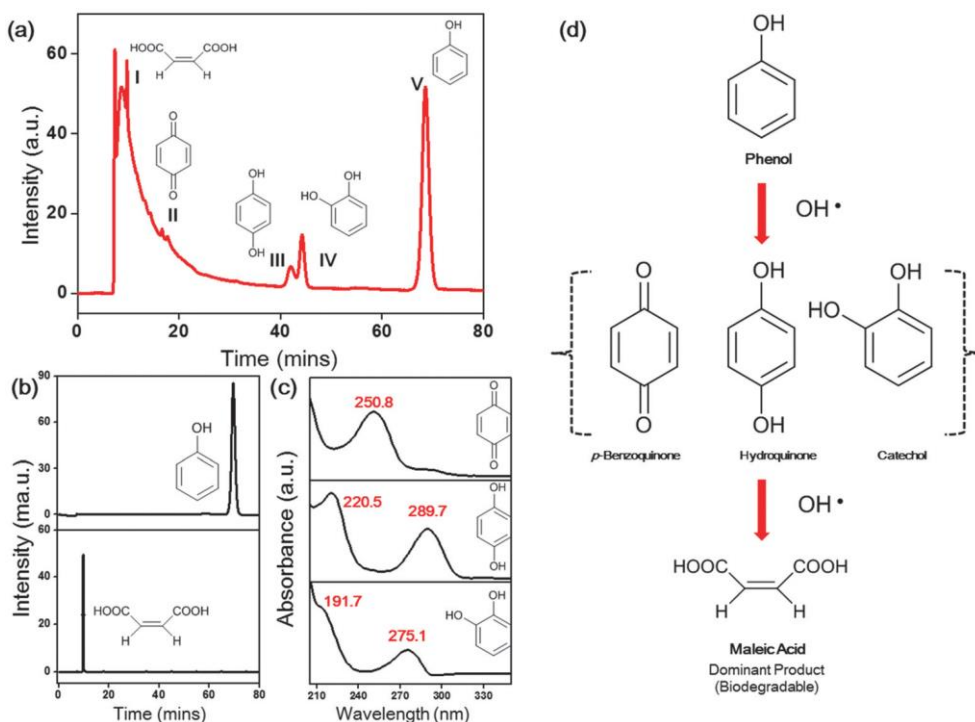


**Figure 2-2.** (a) Time-resolved high-performance liquid chromatography (HPLC) analysis with the designated peaks representing the substances detected in the midst of the pathway. (b) Standard HPLC signals of phenol and maleic acid. (c) UV absorption spectra of the labelled intermediate compounds. (d) Schematic representation of the observed degradation pathway from phenol to maleic acid.

substances separated at 16.65, 41.99, and 44.25 minutes post-injection, as they are likely to manifest less oxidised structures than the substance appearing at 9.74 minutes (Fig. 2-2 c). Based on the reference UV spectra, we could verify that the obtained absorption spectra represent p-benzoquinone, hydroquinone, and catechol, respectively, for the HPLC signals at 16.65, 41.99, and 44.25 minutes.<sup>28–30</sup> As expected, these compounds are the oxidative derivatives of phenol, with different degrees of oxidation. Although  $\text{H}_2\text{O}_2$  signals peaking at 7.43 and 8.65 minutes overlapped with the peaks at 9.74 and 16.65 minutes (Fig. 2-S2 a), they did not interfere with the identification process.

The major substance appearing at 9.74 minutes post-injection was subsequently characterised with the HPLC-coupled organic acid analyser. According to the standard HPLC signals, the peak matches with that of maleic acid (Fig. 2-2 b), which features a biodegradable linear structure with four carbons. Previous studies discussing the potential pathway for oxidative destruction of phenol also report maleic acid as a dominant product through the complete oxidation of phenol to carbon dioxide and water.<sup>4</sup> The report also classifies p-benzoquinone, hydroquinone, and catechol as the major intermediate products prior to the ring opening process to maleic acid, while these substances are not deemed to be biodegradable yet (Fig. 2-2 d).

As 1 cm<sup>2</sup> Gr/SiO<sub>2</sub> could only elicit 25% reduction of the initial concentration of phenols (1 mM), we sought to improve the catalytic efficiency by exploiting an array of multiple graphene films (Fig. 2-3 a). Preliminarily, the relative DCFH-DA fluorescence intensity for graphene films with different areas – 1, 2, 4, and 9 cm<sup>2</sup> – was measured to validate that the amount of generated radicals increases with respect to the area of the graphene film. Intriguingly, the fluorescence intensity markedly increased as a function of graphene area by exhibiting a 131, 208, and 913-fold increase in the fluorescence intensity respectively with 2, 4, and 9 cm<sup>2</sup> Gr/SiO<sub>2</sub> (Fig. 2-3 b).

The same test groups were subsequently employed in time-dependent phenol degradation analysis with HPLC. In accordance with the results from DCFH-DA measurements, the oxidative destruction of phenols occurs in a time-dependent manner with a strong dependency on the area of the graphene film. After 24 hours of incubation, the initial concentration of phenol was reduced by 54%,

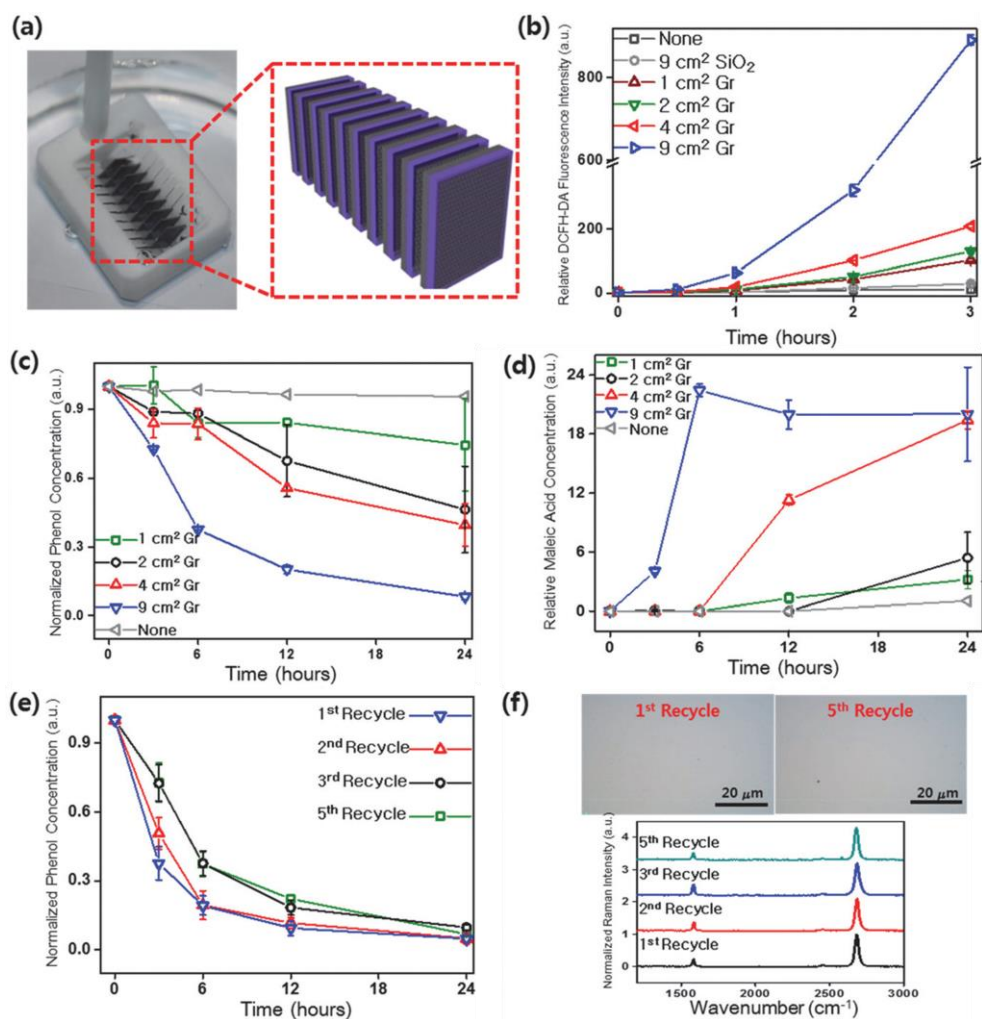


**Figure 2-3.** (a) Schematic representation of multiple 1 cm<sup>2</sup> graphene arrays to improve the catalytic performance. (b) Representative graphene area-dependent DCFH-DA fluorescence intensity (2 μM) with 100 mM H<sub>2</sub>O<sub>2</sub>. (c) Time-dependent changes in phenols and (d) maleic acid using graphene films with different unit areas. (e) Time-dependent changes in the amount of phenols through HPLC analysis of the recycled 9 cm<sup>2</sup> graphene films with normalised phenolic levels. (f) Representative optical microscopy (OM) images and Raman spectra after performing the first, second, third and fifth incubation cycles.

60%, and 92% respectively with 2, 4, and 9 cm<sup>2</sup> Gr/SiO<sub>2</sub> (Fig. 2-3 c).

It should also be noted that the total amount of non-biodegradable ring structures – phenol, hydroquinone and catechol – decreased gradually with time.

Likewise, time-dependent maleic acid concentrations were monitored by using the HPLC-coupled organic acid analyser (Fig. 2-3 d). Interestingly for 9 cm<sup>2</sup> Gr/SiO<sub>2</sub>, which exhibited the highest phenol reduction ratio, the concentration of maleic acid sharply increased after 3 hours of incubation. However, it shows a slight decline after 6 hours and becomes saturated until the end of the incubation period. Such inconsistent trends between the maleic acid increments and the phenol decrements can be attributed to the complete oxidation of maleic acid to carbon dioxide and water, which was supported by the generation of bubbles in the test batches.

Finally, the recyclability of the graphene film was investigated by carrying out repetitive phenol destruction tests using a single 9 cm<sup>2</sup> Gr/SiO<sub>2</sub> sample (Fig. 2-3 e). After each cycle, the levels of phenols and oxidised intermediates were analysed. Remarkably, graphene films elicited the same catalytic effects after a series of recycling processes; four distinct time-resolved HPLC spectra for phenol degradation by the first, second, third, and fifth recycled 9 cm<sup>2</sup> Gr/SiO<sub>2</sub> display practically the same results (Fig. 2-3 e). On average, the concentration of the remaining phenol was  $6.5 \pm 2.3\%$  in each tested cycle. This is nearly equivalent to the 92% reduction achieved with pristine 9 cm<sup>2</sup> Gr/SiO<sub>2</sub>.

For the analysis of the intrinsic properties of graphene, any damage or changes on the surface were evaluated through optical microscopy (OM), Raman spectroscopy and X-ray photoelectron spectroscopy (XPS) analyses (Fig. 2-3 f and Fig. 2-S3). The representative OM images clearly display that the graphene film was not damaged even after the fifth round of incubation cycle, and only a minimal part of stained spots were observed. The respective Raman spectra also supported that the original condition and quality of graphene were preserved over the fifth round of degradation cycle, by showing the respective 2D/G ratios of 3.72, 3.43,



4.30, and 3.84 for the graphene film respectively after the first, second, third, and fifth recycling (2D peak at  $2680\text{ cm}^{-1}$  and G peak at  $1580\text{ cm}^{-1}$ ). In general, the 2D/G ratio that exceeds 2 represents monolayer graphene, and a high 2D/G ratio typically corresponds to high intrinsic crystallinity. In addition, XPS analyses on the chemical composition of graphene pre- and post-phenol degradation exhibited essentially the same results, which corroborated that graphene was not severely oxidized by the surrounding hydrogen peroxide or organic molecules (Fig. 2-S3).

## 1.4. Conclusion

In summary, we have successfully demonstrated the potential application of a CVD graphene film for the oxidative destruction of phenols through a novel AOP method. Although the catalytic activity of the graphene film-based AOP system is relatively lower and thus requires a longer incubation time than the conventional metal-based catalysts, it overcomes the inevitable drawbacks of the previous methods including the need for pH adjustment, input of external energies, and further steps for residual salt removal. In addition, it is important to note that the graphene film's catalytic efficiency is markedly improved by enlarging the dimension of the film – which can be as large as 30 inches, produced by the roll-to-roll method – which is expected to be utilized as a recyclable catalyst with considerable catalytic effects for industrial applications. As graphene can also be transferred onto flexible substrates, the range of potential applications can be even more broadened to different areas that demand the use of powerful secondary radicals generated by the environment-friendly film catalyst.

## 1.5. Experimental

**Preparation of CVD Graphene Film.** Graphene was synthesised by the chemical vapour deposition (CVD) method on a highly pure copper foil (Alfa Aesar, 99.95 %) according to the previous work.<sup>13</sup> The growth was performed with flowing 40 sccm H<sub>2</sub> and 5 sccm CH<sub>4</sub> gas at 1000 °C. After coating a poly methyl methacrylate (PMMA) layer on a single side of as-grown graphene on Cu foil, the uncoated graphene was removed by oxygen plasma. The Cu foil was subsequently etched in ammonium persulfate (APS) solution (20 g/L) for 5 hours. The PMMA/Gr layer was then transferred onto SiO<sub>2</sub> substrate, followed by baking at 80 °C for 24 hours to improve the adhesion. Finally, the PMMA layer was removed by acetone.

**Characterisation.** Optical microscopy (OM) images were captured by a NIKON ECLIPSE LV 100 ND OM installed with NIS Elements D 4.20.00 software. A RENISHAW Raman spectrometer was used to characterise the quality and uniformity of the prepared graphene films. The Raman spectra were obtained using an Ar laser (514 nm) with a spot size of 1 mm. The samples were analysed by high resolution – transmission electron microscope (HR-TEM, JEM-3010, JEOL Ltd.) and Cs corrected STEM with Cold FEG (JEM-ARM200F, JEOL Ltd.) and the images were collected by Gatan Digital Camera (MSC-794) coupled to the microscope. XPS spectra for Gr/SiO<sub>2</sub> were obtained by K $\alpha$  XPS system (Thermo-Scientific) with an X-ray mono-chromator (Al K $\alpha$  Microfocused depth profiling EX06 Ion Source) with a spot size of 30 – 400  $\mu$ m.

**DCFH-DA Fluorescence Measurements.** The generation of secondary reactive oxygen species (ROS) was measured with the fluorescence of 2',7'-

dichlorofluorescein diacetate (DCFH-DA) probe (Sigma Aldrich, Ex/Em: 495 nm/529 nm, 2  $\mu$ M).<sup>16</sup> The measurements for all test groups were performed after designated amounts of incubation periods with 5 ml of total volume.

**Ion-exchange HPLC Analysis.** For the analysis of oxidative destruction of phenols, a hydrogen column (Aminex 87H column, 300x10 mm, Bio-Rad, USA) ion-exchange high performance liquid chromatography (HPLC, Dionex Ultimate3000) was utilised. Total injection volume was set to 10  $\mu$ l in all test samples with 0.01 N H<sub>2</sub>SO<sub>4</sub> eluent and the flow rate of 0.5 ml/min. Time-resolved HPLC analyses were performed over 90 minutes of injection time, and the intermediate structures were identified with the RI detector (ERC, RefractoMAX520, Japan). The identification of produced organic acid was carried out by the organic acid analysis coupled to the HPLC, based on the reference peaks and the retention times.

**pH and Temperature Measurements.** During graphene-based phenol degradation process, the pH and temperature changes were monitored by a pH meter equipped with a digital thermometer (Trans instruments, BP3001). The changes were measured 0, 1, 3, 6, 12, 24 hours post-incubation. The values were recorded after 5 minutes of each time point for stabilisation.

**X-ray Photoelectron Spectroscopy Analysis.** XPS spectra for Gr/SiO<sub>2</sub> were obtained by K $\alpha$  XPS system (Thermo-Scientific) with an X-ray mono chromator (Al K $\alpha$  Micro-focused depth profiling EX06 Ion Source) with a spot size of 30 – 400  $\mu$ m.

## 1.6. Supplementary Information

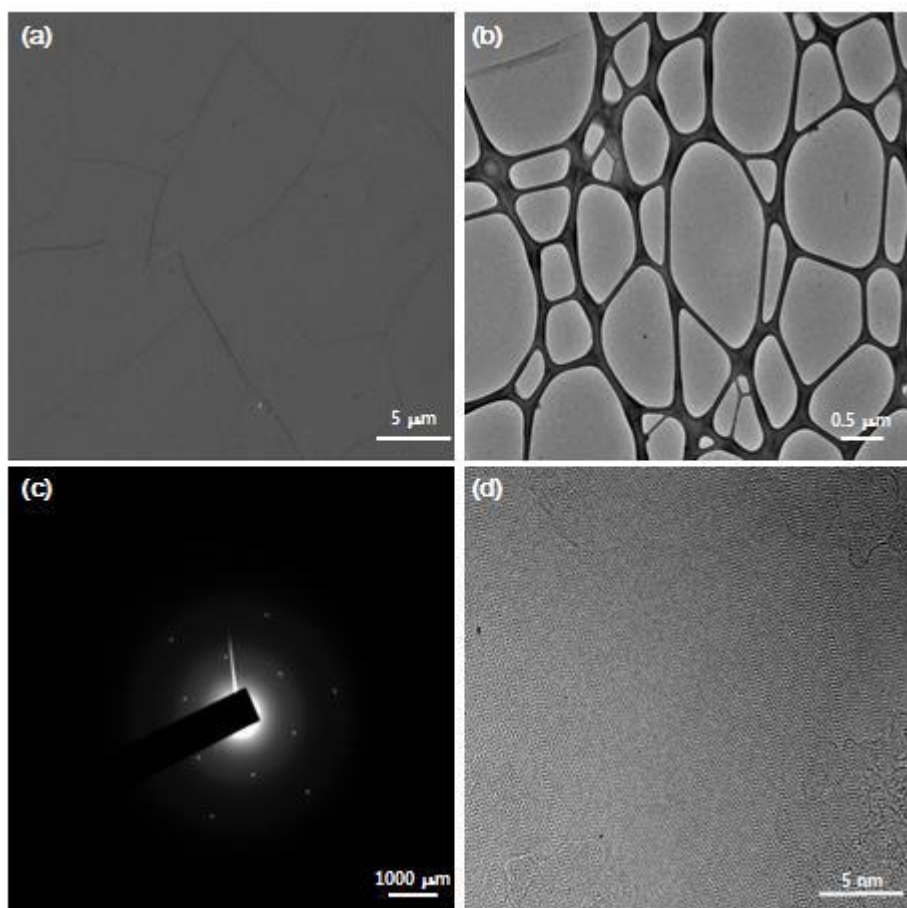


**Figure 2-S1.** (a) Representative SEM and (b) HRTEM images of the monolayer graphene film with (c) distinctive SAED pattern. (d) Representative Cs corrected STEM image of the monolayer graphene.

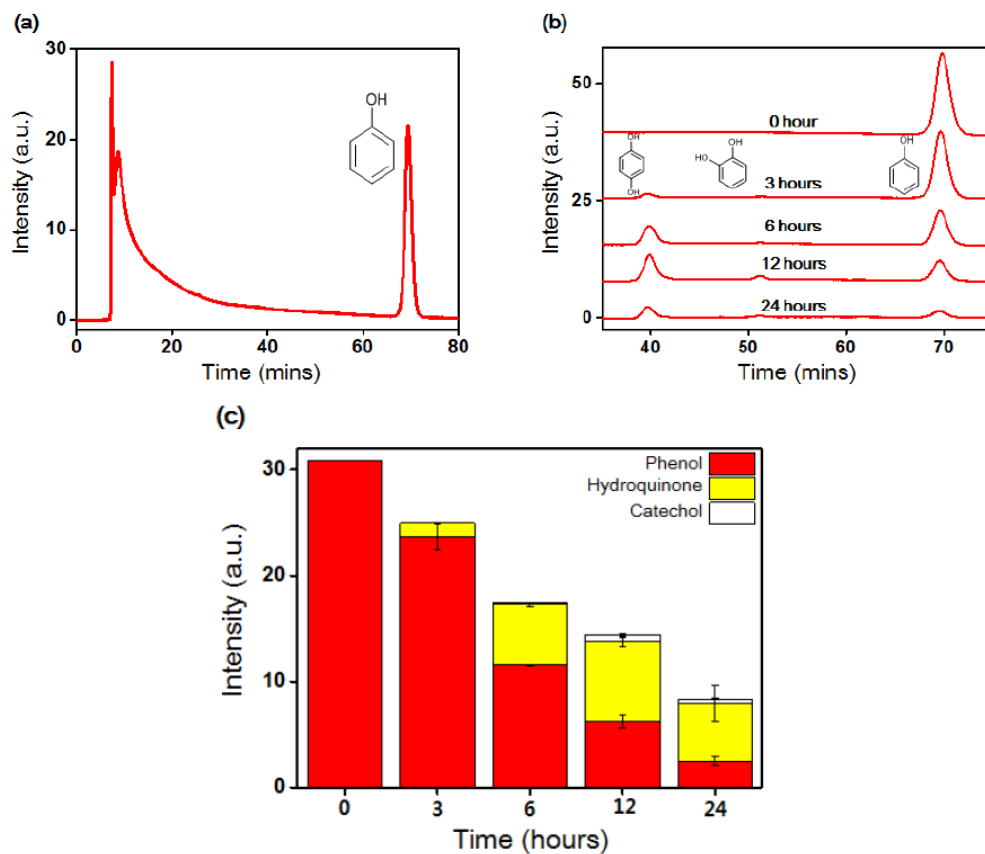


**Figure 2-S2.** (a) HPLC analysis of hydrogen peroxide (100 mM) and phenols (1 mM). Hydrogen peroxide show strong, broad signals peaking at 7.43 and 8.65 minutes. (b) Time-dependent HPLC analysis and (c) quantified intensities with 9 cm<sup>2</sup> graphene film after 0, 3, 6, 12 and 24 hours of incubation with 1 mM phenols and 100 mM hydrogen peroxide.

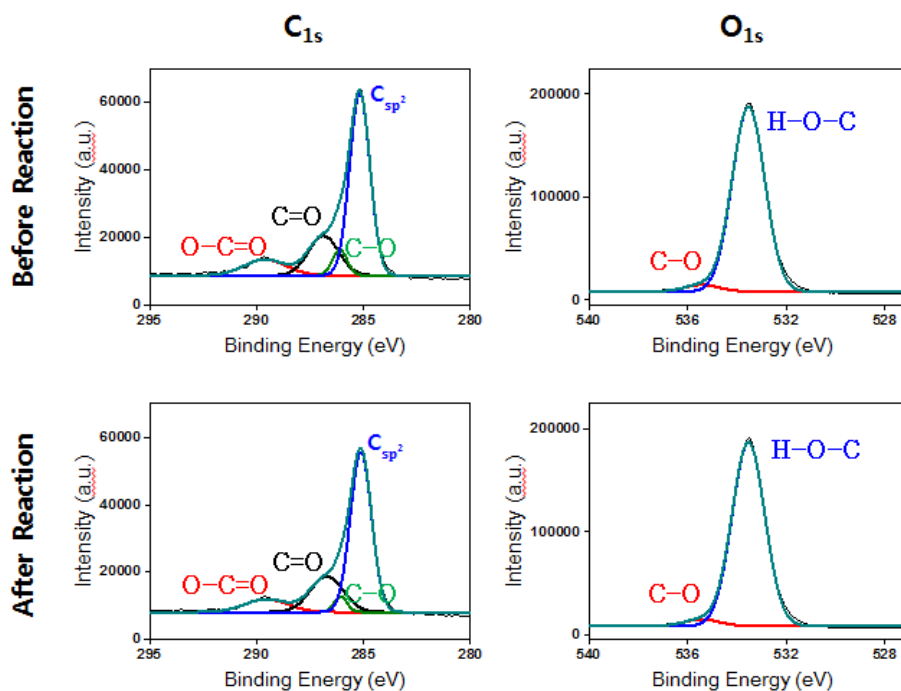


**Figure 2-S3.**  $C_{1s}$  (left) and  $O_{1s}$  (right) XPS analysis pre- and post-phenol degradation respectively from the top. The characteristic  $C_{1s}$  signals exhibited distinctive atomic ratio changes from  $0.12 \rightarrow 0.10$ ,  $0.2 \rightarrow 0.22$ ,  $0.06 \rightarrow 0.04$  and  $0.62 \rightarrow 0.64$  respectively at 289 eV ( $O-C=O$ ), 286.8 eV ( $C=O$ ), 286.1 eV ( $C-O$ ) and 285 eV ( $C_{sp^2}$ ). Likewise, the characteristic  $O_{1s}$  signals displayed atomic ratio changes from  $0.04 \rightarrow 0.04$  and  $0.96 \rightarrow 0.96$  at 535 eV ( $C-O$ ) and 533 eV ( $H-O-C$ ).

## 1.7. References

1. E. Halfon, *Environ. Sci. Technol.*, 1986, **20**, 1173–1179.
2. M. Pera-Titus, V. García-Molina, M. A. Baños, J. Giménez and S. Esplugas, *Appl. Catal., B*, 2004, **47**, 219–256.
3. P. R. Gogate and A. B. Pandit, *Adv. Environ. Res.*, 2004, **8**, 501–551.
4. J. A. Zazo, J. A. Casas, A. F. Mohedano, M. A. Gilarranz and J. J. Rodríguez, *Environ. Sci. Technol.*, 2005, **39**, 9295–9302.
5. J. J. Pignatello, E. Oliveros and A. MacKay, *Crit. Rev. Environ. Sci. Technol.*, 2006, **36**, 1–84.
6. R. Andreozzia, A. Insolab and R. Marottac, *Catal. Today*, 1999, **53**, 51–59.
7. P. V. Nidheesh, *RSC Adv.*, 2015, **5**, 40552–40577.
8. T. Soltani and M. H. Entezari, *Chem. Eng. J.*, 2014, **251**, 207–216.
9. C. C. Winterbourn, *Toxicol. Lett.*, 1995, **82–83**, 969–974.
10. M. L. Kremer, *J. Phys. Chem. A*, 2003, **107**, 1734–1741.
11. M. E. Ragoussi, G. Katsukis, A. Roth, J. Malig, G. de la Torre, D. M. Guldi and T. Torres, *J. Am. Chem. Soc.*, 2014, **136**, 4593–4598.
12. H. Sun, K. Dong, J. Ren and X. Qu, *ACS Nano*, 2014, **8**, 6202–6210.
13. P. L. Levesque, S. S. Sabri, C. M. Aguirre, J. Guillemette, M. Siaj, P. Desjardins, T. Szkopek and R. Martel, *Nano Lett.*, 2011, **11**, 132–137.
14. T. Hu and I. C. Gerber, *J. Phys. Chem. C*, 2013, **117**, 2411–2420.
15. S. J. Kim, T. Choi, B. Lee, S. Lee, K. Choi, J. B. Park, J. M. Yoo, Y. S. Choi, J. Ryu, P. Kim, J. Hone and B. H. Hong, *Nano Lett.*, 2015, **15**, 3236–3240.
16. S. Bae, H. Kim, Y. Lee, X. Xu, J. S. Park, Y. Zheng, J. Balakrishnan, T. Lei, H. R. Kim, Y. I. Song, Y. J. Kim, K. S. Kim, B. Ozyilmaz, J. H. Ahn, B. H. Hong and S. Iijima, *Nat. Nanotechnol.*, 2010, **5**, 574–578.
17. Y. Oyama, T. Uehab and K. Maekawac, *Brain Res.*, 1994, **635**, 113–117.
18. K. Setsukinai, Y. Urano, K. Kakinuma, H. J. Majima and T. Nagano, *J. Biol. Chem.*, 2003, **278**, 3170–3175.
19. S. Amirfakhri, D. Binny, J. Meunier and D. Berk, *J. Power Sources*, 2014, **257**,

- 356–363.
20. P. Wu, P. Du, H. Zhang and C. Cai, *Phys. Chem. Chem. Phys.*, 2013, **15**, 6920–6928.
21. H. Tachikawa, T. Iyama and H. Kawabata, *Jpn. J. Appl. Phys.*, 2013, **52**, 01AH01.
22. S. Akca, A. Foroughi, D. Frochtzawajg and H. W. C. Postma, *PLoS One*, 2011, **6**, e18442.
23. C. R. Martinez and B. L. Iverson, *Chem. Sci.*, 2012, **3**, 2191–2201.
24. S. Virendra, J. Daeha and Z. Lei, *Prog. Mater. Sci.*, 2011, **56**, 1178–1271.
25. M. Velicky, D. F. Bradley, A. Cooper, E. W. Kinloch, A. Mishchenko, K. S. Novoselov, H. V. Patten, P. S. Toth, A. T. Valota, S. D. Worrall and R. A. W. Dryfe, *ACS Nano*, 2014, **8**, 10089–10100.
26. A. Kütt, V. Movchun, T. Rodima, T. Dansauer, E. B. Rusanov, I. Leito, I. Kaljurand, J. Koppel, V. Pihl, I. Koppel, G. Ovsjannikov, L. Toom, M. Mishima, M. Medebielle, E. Lork, G.-V. Röschenthaler, I. A. Koppel and A. A. Kolomeitsev, *J. Org. Chem.*, 2008, **73**, 2607–2620.
27. M. G. Harris, J. Torres and L. Tracewell, *Am. J. Optom. Physiol. Opt.*, 1988, **65**, 527–535.
28. T. Wilke, M. Schneider and K. Kleinermanns, *Open J. Phys. Chem.*, 2013, **3**(2), 97–102.
29. A. Kiss, J. Molnar and C. Sandorfy, *Bull. Soc. Chim. Fr.*, 1949, **16**, 275–280.
30. M. J. S. Dewar, V. P. Kubba and R. Pettit, *J. Chem. Soc.*, 1958, 3076–3079.



## Chapter 3

# Graphene Quantum Dots Prevent $\alpha$ -synucleinopathy in Parkinson's Disease

### 1.1. Abstract

Though emerging evidence indicates that the pathogenesis of Parkinson's disease is strongly correlated to the accumulation<sup>1,2</sup> and transmission<sup>3,4</sup> of  $\alpha$ -synuclein ( $\alpha$ -syn) aggregates in the midbrain, no anti-aggregation agents have been successful at treating the disease in the clinic. Here, we show that graphene quantum dots (GQDs) inhibit fibrillization of  $\alpha$ -syn and interact directly with mature fibrils, triggering their disaggregation. Moreover, GQDs can rescue neuronal death and synaptic loss, reduce Lewy body and Lewy neurite formation, ameliorate mitochondrial dysfunctions, and prevent neuron-to-neuron transmission of  $\alpha$ -syn pathology provoked by  $\alpha$ -syn preformed fibrils<sup>5,6</sup>. We observe, *in vivo*, that GQDs penetrate the blood–brain barrier and protect against dopamine neuron loss induced by  $\alpha$ -syn preformed fibrils, Lewy body/Lewy neurite pathology and behavioural deficits.

---

\* This chapter is reproduced from: Donghoon Kim<sup>†</sup>, Je Min Yoo<sup>†</sup>, Heehong Hwang, Junghee Lee, Su Hyun Lee, Seung Pil Yun, Myung Jin Park, MinJun Lee, Seulah Choi, Sang Ho Kwon, Saebom Lee, Seung-Hwan Kwon, Sangjune Kim, Misaki Kinoshita, Young-Ho Lee, Seokmin Shin, Seung R. Paik, Sung Joong Lee, Seulki Lee, Byung Hee Hong<sup>\*</sup> and Han Seok Ko<sup>\*</sup>. *Nature Nanotechnology* (2018) **13**, 812-818. © Springer Nature

## 1.2. Results and Discussion

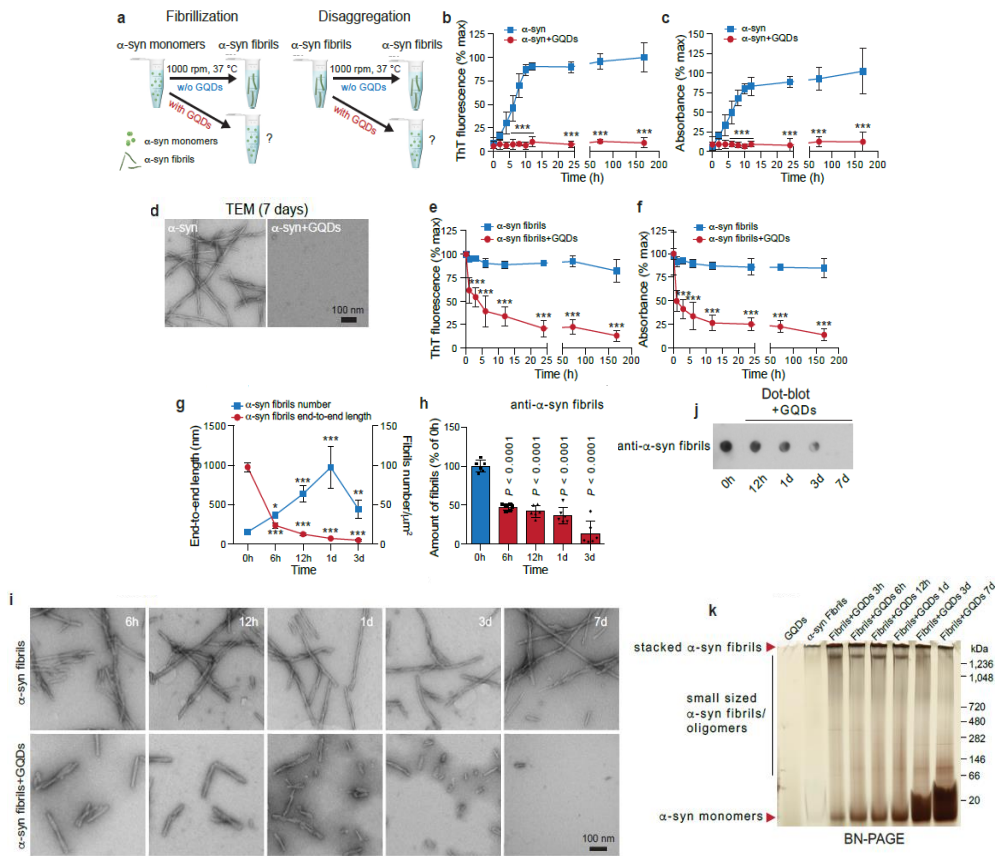


**Figure 3-1.** Effect of GQDs on  $\alpha$ -syn fibrillization and fibril disaggregation. **a**, Schematic representation of  $\alpha$ -syn fibrillization (5 mg/ml  $\alpha$ -syn monomers) and disaggregation (5 mg/ml  $\alpha$ -syn fibrils) in the presence and absence of GQDs (5 mg/ml). **b,c**, Kinetics of  $\alpha$ -syn fibrillization using aliquots of the reaction monitored by ThT fluorescence (**b**) and turbidity assays (**c**) ( $n=4$  biologically independent samples; two-way analysis of variance (ANOVA) with a post hoc Bonferroni test, \*\*\* $P < 0.001$ ; error bars are standard deviation, s.d.). Mean values and  $P$  values are provided in Supplementary Table 1. **d**, TEM images of  $\alpha$ -syn after fibrillization in the absence (left) and presence (right) of GQDs. **e,f**, Kinetics of preformed  $\alpha$ -syn fibrils after incubation with GQDs using aliquots of the reaction monitored by ThT fluorescence (**e**) and turbidity assays at various time points (**f**) ( $n=4$  biologically independent samples; two-way ANOVA with a post hoc Bonferroni test, \*\*\* $P < 0.001$ ; error bars are s.d.). Mean values and  $P$  values are provided in Supplementary Table 1. **g**, Quantifications of the end-to-end length and number of  $\alpha$ -syn fibrils per  $\mu\text{m}^2$ . Mean values of end-to-end length are 937.84, 245.52, 123.13, 66.27 and 51.02 nm at 0, 6, 12, 24 and 72 h ( $n=50$  fibrils at each time point; one-way ANOVA with a post hoc Bonferroni test,  $P <$

0.0001 at 6, 12, 24 and 72 h; error bars are s.d.). Mean values of number are 15.53, 37.01, 63.83, 97.52 and 44.38 per  $\mu\text{m}^2$  at 0, 6, 12, 24 and 72 h (n=6, biologically independent samples; one-way ANOVA with a post hoc Bonferroni test,  $P = 0.0483$ ,  $P < 0.0001$ ,  $P < 0.0001$  and  $P = 0.0050$  at 6, 12, 24 and 72 h, respectively; error bars are s.d.). h, Amount of remaining  $\alpha$ -syn fibrils (as % of number at 0 h), determined by multiplying the end-to-end length and number of  $\alpha$ -syn fibrils at the same time points (0, 6, 12, 24 and 72 h) in the presence of GQDs. Mean values are 100.00, 47.33, 42.00, 36.67 and 13.83 at 0, 6, 12, 24 and 72 h (n=6, biologically independent samples; one-way ANOVA with a post hoc Bonferroni test, error bars are s.d.). i, TEM images of preformed  $\alpha$ -syn fibrils at various time points (6 and 12 h, 1, 3 and 7 days) in the absence (top) and presence (bottom) of GQDs. j, Representative image of  $\alpha$ -syn fibrils dot-blot assay at various time points (0 and 12 h, 1, 3 and 7 days) with  $\alpha$ -syn filament specific antibody. These experiments were independently repeated three times with similar results. k, BN-PAGE analysis of  $\alpha$ -syn, prepared with aliquots of reaction run at various time points (0, 3, 6 and 12 h, 1, 3 and 7 days). These experiments were independently repeated three times with similar results.

Following the synthesis and analysis of graphene quantum dots (GQDs) (Fig. 3-S2a–c,e), we investigated the potential role of these in inhibiting  $\alpha$ -synuclein ( $\alpha$ -syn) fibrillization and disaggregating fibrils (Fig. 3-1 a). In the absence of GQDs,  $\alpha$ -syn monomers assembled into mature fibrils, as assessed by thioflavin T (ThT) fluorescence (Fig. 3-1 b), turbidity assays (Fig. 3-1 c) and transmission electron microscopy (TEM) analysis (Fig. 3-1 d). The same assessments showed that the GQDs predominantly inhibited  $\alpha$ -syn fibrillization. Moreover, GQDs induced the dissociation of  $\alpha$ -syn fibrils into short fragments (Fig. 3-1 e–i and Fig. 3-S3 a), with the average length of the fragments shortening from 1  $\mu\text{m}$  to 235 nm and 70 nm after 6 and 24 h, respectively (Fig. 3-1 g,i). The average number of the shortened fragments increased during the first 24 h of incubation, suggesting that the fibrils had dissociated from the inner parts of the  $\alpha$ -syn fibrils (Fig. 3-1 h). However, the number of fragments started to decrease at day 3 and they were no longer detectable at day 7, indicating complete dissociation of fibrils

over the course of time (Fig. 3-1 i). Time-dependent atomic force microscopy (AFM) images show the same dissociation process, where GQDs and fibrils can be differentiated by their distinguishing height profiles (Fig. 3-S3 b). Dot-blot assay and blue native polyacrylamide gel electrophoresis (BN-PAGE) analysis also revealed that incubation with GQDs results in the gradual reduction of fibrils in a time-dependent manner (Fig. 3-1 j,k). Similar effects of GQDs were also observed on sonicated  $\alpha$ -syn preformed fibrils (PFFs), which produced a higher population of monomers as the incubation period progressed (Fig. 3-S4 a–c).

To visualize the interaction between GQDs and  $\alpha$ -syn fibrils, GQDs were functionalized with PEGylated biotin (Fig. 3-S2 d–g). Using streptavidin-tagged ultra-small gold particles and TEM, direct binding between GQDs and  $\alpha$ -syn fibrils was visualized (Fig. 3-2 a,b). Two-dimensional  $^1\text{H}$ – $^{15}\text{N}$  heteronuclear single-quantum coherence correlation (HSQC) NMR spectroscopy was utilized to further analyse the interaction site of  $^{15}\text{N}$ -labelled  $\alpha$ -syn<sup>7,8</sup> for GQDs and their molecular interactions at the residue level in solution. Co-incubation with GQDs led to many residues with large chemical shifts while others had entirely disappeared (Fig. 3-S5). The residues that disappeared were centred on the N-terminal region, implying that the initial binding between GQDs and  $\alpha$ -syn is largely driven by the charge interaction between the negatively charged carboxyl groups of the GQDs (Fig. 3-S2 e) and the positively charged region of  $\alpha$ -syn (Fig. 3-2 c).

To better understand and elucidate the mechanism of  $\alpha$ -syn fibril dissociation by GQDs, a 200 ns molecular dynamics (MD) simulation was performed. The structure of the  $\alpha$ -syn fibril was adopted from the recently reported ssNMR (solid-state nuclear magnetic resonance) structure of pathologic human  $\alpha$ -syn<sup>9</sup>. To facilitate the simulation process, only the non-amyloid- $\beta$  component

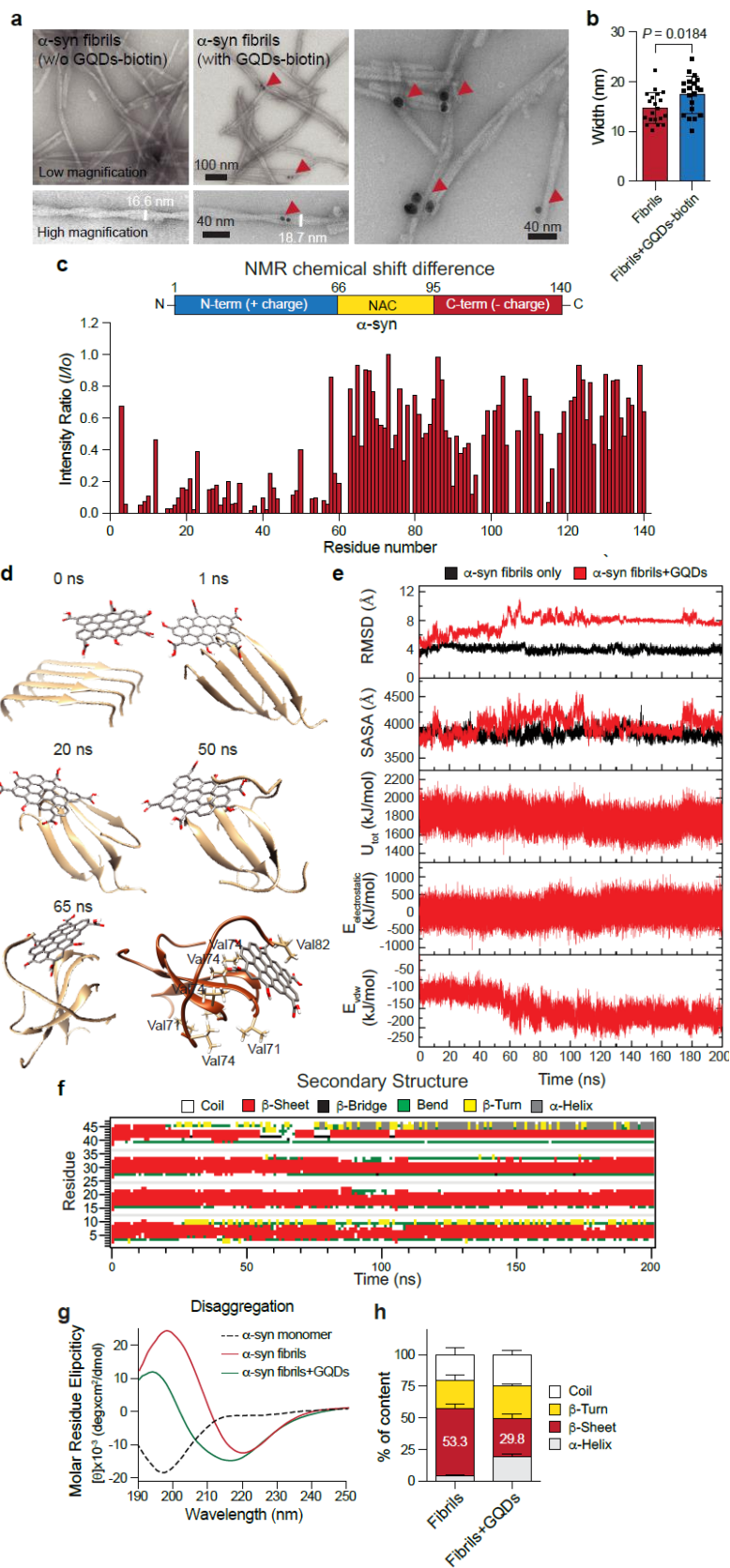


**Figure 3-2.** Detailed analysis of the interaction between GQDs and mature  $\alpha$ -syn fibrils during the dissociation process. a, TEM images for binding between biotinylated GQDs and  $\alpha$ -syn fibrils with low and high magnifications. Arrowheads indicate biotinylated GQDs enhanced with ultra-small gold–streptavidin nanoparticles. b, Quantification of the average width of  $\alpha$ -syn fibrils during the disaggregation process after 1 h of incubation (mean  $\pm$  s.d.):  $14.74 \pm 0.70$  nm and  $17.42 \pm 0.83$  nm for fibrils and fibrils + GQDs–biotin (n=20 for each group, two-tailed Student’s t-test). c, NMR chemical shift difference obtained from full  $^1\text{H}$ – $^{15}\text{N}$  HSQC spectra. The decreased intensity ratio of NMR chemical shifts is presented for each residue after binding with GQDs. d, Time course simulation dynamics of the interaction between GQDs and mature  $\alpha$ -syn fibrils, and 65 ns snapshot image (bottom right) of the interaction between GQDs and mature  $\alpha$ -syn fibrils with designated sidechains attributed for the major binding force. e, Time-dependent plots for r.m.s.d. of atomic positions, SASA for the  $\alpha$ -syn fibril only group and  $\alpha$ -syn fibril and GQDs group, total potential energy ( $\Delta U_{\text{tot}}$ ), electrostatic energy ( $\Delta E_{\text{elec}}$ ) and van der Waals energy ( $\Delta E_{\text{van}}$ ) for  $\alpha$ -syn fibril and GQDs group, respectively (from the top). f, Time-dependent secondary structure plot calculated by the DSSP algorithm. g, CD spectra of  $\alpha$ -syn monomers and  $\alpha$ -syn fibrils without and with GQDs after 7 days of incubation. h, Fractional secondary structure contents ratio of  $\alpha$ -syn fibrils and  $\alpha$ -syn fibrils disaggregated by GQDs calculated using the algorithm CONTIN/LL (n=5 biologically independent samples). Data presented as mean  $\pm$  s.d. (fibrils versus fibrils + GQDs (% of content); coil:  $20.13 \pm 5.74$  versus  $24.58 \pm 3.64$ ;  $\beta$ -turn:  $22.39 \pm 4.62$  versus  $25.89 \pm 1.34$ ;  $\beta$ -sheet:  $53.30 \pm 3.53$  versus  $29.76 \pm 3.35$ ;  $\alpha$ -helix:  $4.17 \pm 1.25$  versus  $19.74 \pm 1.52$ ).

(NAC) domain (residues 71 to 82) was taken, as it is essential for  $\alpha$ -syn fibrillization<sup>10</sup>. Following instantaneous binding between the GQDs and the N terminal cross- $\beta$  part of  $\alpha$ -syn at 1 ns, the  $\beta$ -sheet structure of the outer monomer was completely destroyed after 50 ns; its C-terminal part was released from the core and interacted with the opposite plane of the GQDs (Fig. 3-2 d). The time-dependent secondary structure plot, calculated by the dictionary of secondary structure of proteins (DSSP) algorithm, also shows a decrease in the  $\beta$ -sheet component of the outer monomer from 50 ns onwards, indicating critical structural disruption in the fibril (Fig. 3-2 f). For further analysis, changes in the root-mean-

square deviation (r.m.s.d.) of atomic positions, solvent accessible surface area (SASA) and the interaction energies of the fibril were plotted against time (Fig. 3-2 e). Though massive changes in the r.m.s.d. and SASA values are observed after 50 ns, the changes in the total potential energy ( $\Delta U_{\text{tot}}$ ) show a slight, yet continuous decline. It is confirmed that the major stabilizing/dissociation force is attributed to strong hydrophobic interactions, as changes in the van der Waals energy ( $\Delta E_{\text{van}}$ ) show a decline and the electrostatic energy ( $\Delta E_{\text{elec}}$ ) remains steady. The results are consistent with the 65 ns snapshot, which shows strong hydrophobic interactions between the GQDs' basal plane and valine residues (Fig. 3-2 d). To further analyse the changes in the secondary structure of  $\alpha$ -syn fibrils, circular dichroism (CD) spectra were obtained and the fractional secondary structures were analysed using the algorithm CONTIN/LL<sup>11,12</sup> (Fig. 3-2 g,h). After 7 days, changes in the secondary structure were observed, with the  $\beta$ -sheet component decreasing from  $53.3 \pm 3.5\%$  to  $29.8 \pm 3.4\%$  and the  $\alpha$ -helix/random coil components increasing from  $4.2 \pm 1.2\%$  to  $19.8 \pm 1.5\%$  and  $20.1 \pm 5.7\%$  to  $24.6 \pm 3.6\%$ , respectively. Collectively, the interaction between GQDs and  $\alpha$ -syn is initiated by the charge interactions, and fibril dissociation is driven chiefly by hydrophobic interactions, accompanied by structural changes.

Based on these results, the potential role of GQDs in preventing  $\alpha$ -syn PFF-induced pathology was explored in primary neurons.  $\alpha$ -syn PFF treatment leads to critical cell death, as assessed by various cell viability assays including terminal deoxynucleotidyl transferase dUTP nick end labelling (TUNEL) (Fig. 3-3 a and Fig. 3-S6 a), alamarBlue (Fig. 3-3 b), lactate dehydrogenase (LDH) (Fig. 3-3 c) and neurite outgrowth assays (Fig. 3-S6 b–d). In contrast, the presence of GQDs reduces  $\alpha$ -syn PFF-induced cell toxicity in the same assessments.

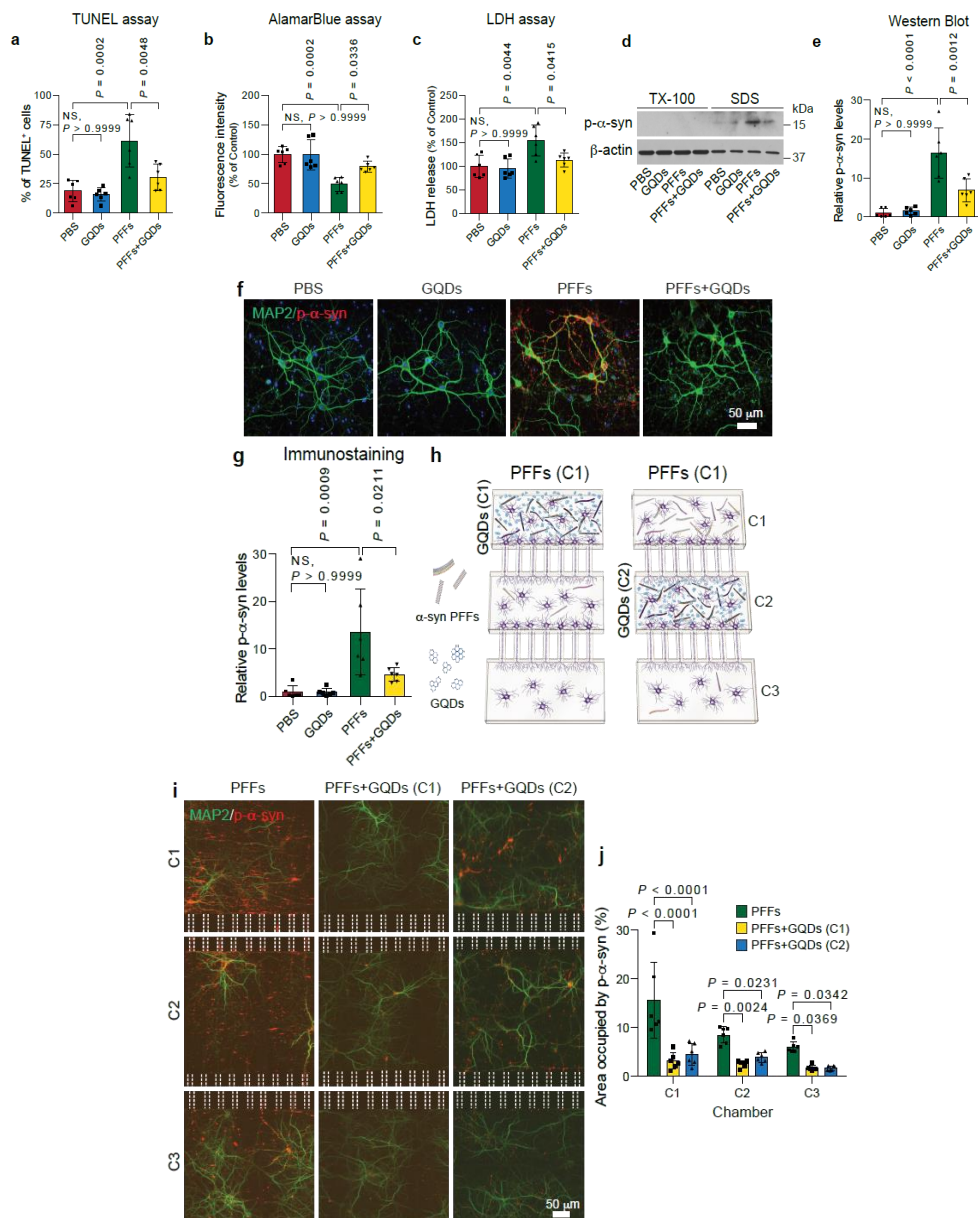


**Figure 3-3.** Effect of GQDs on  $\alpha$ -syn PFF-induced neuronal death, pathology and transmission *in vitro*. a–c, Neuronal death assessed by TUNEL (a), alamarBlue (b) and LDH assays (c) treated with  $\alpha$ -syn PFFs (1  $\mu$ g/ml) in the absence and presence of GQDs (1  $\mu$ g/ml) in 10 DIV mouse cortical neurons for 7 days. Mean values of TUNEL (% of TUNEL+ cells) are 18.94, 15.86, 61.39 and 30.45 for PBS, GQDs, PFFs and PFFs + GQDs; mean values of alamarBlue (% of control) are 100.00, 99.16, 49.33 and 78.86 for PBS, GQDs, PFFs and PFFs + GQDs; mean values of LDH assay (% of control) are 100.00, 95.43, 154.58 and 113.33 for PBS, GQDs, PFFs and PFFs + GQDs (n=6 biologically independent samples; two-way ANOVA with post hoc Bonferroni test; NS, not significant;



error bars are s.d.). d, Representative immunoblot levels with p- $\alpha$ -syn antibody. e, Quantifications of the SDS-insoluble fraction normalized to the levels of  $\beta$ -actin. Mean values are 1.00, 1.49, 16.35 and 6.86 for PBS, GQDs, PFFs and PFFs + GQDs (n=6 biologically independent samples; two-way ANOVA with post hoc Bonferroni test; NS, not significant; error bars are s.d.). f, Representative p- $\alpha$ -syn immunostaining micrographs with p- $\alpha$ -syn antibody. g, Quantifications of p- $\alpha$ -syn immunofluorescence intensities normalized to PBS control. Mean values are 1.00, 0.99, 13.62 and 4.69 for PBS, GQDs, PFFs and PFFs + GQDs (n=6 biologically independent samples; two-way ANOVA with post hoc Bonferroni test; NS, not significant; error bars are s.d.). h, Schematic representation of the microfluidic device for the transmission of pathologic  $\alpha$ -syn, composed of three connected chambers. i, Representative images of p- $\alpha$ -syn immunostained neurons in the microfluidic device 14 days post  $\alpha$ -syn PFFs addition. j, Quantifications of p- $\alpha$ -syn immunofluorescence intensities. Areas occupied by p- $\alpha$ -syn were measured in each chamber. Mean values of chamber 1 are 15.67, 3.12 and 4.52 for PFFs, PFFs + GQDs (C1) and PFFs + GQDs (C2); mean values of chamber 2 are 8.52, 2.56 and 3.90 for PFFs, PFFs + GQDs (C1) and PFFs + GQDs (C2); mean values of chamber 3 are 6.04, 1.72 and 1.67 for PFFs, PFFs + GQDs (C1) and PFFs + GQDs (C2) (n=6 biologically independent samples; two-way ANOVA with post hoc Bonferroni test; NS, not significant; error bars are s.d.).

In addition, treatment of  $\alpha$ -syn PFFs leads to a reduction in synaptic proteins such as SNAP25 and VAMP2, suggesting severe dysfunction in neuronal networks<sup>5</sup>. Importantly, GQDs restore the reduced synaptic protein levels provoked by  $\alpha$ -syn PFFs (Fig. 3-S6 e–g). Mitochondrial dysfunction is another major pathological hallmark during the progression of Parkinson's disease<sup>13</sup>. The effect of GQDs on mitochondrial dysfunction and subsequent cellular respiration was thus investigated by performing oxidative stress marker 8-hydroxyguanosine (8-OHG) staining, mitochondrial complex I activity assay, MitoTracker staining, TEM analysis and seahorse assay (Fig. 3-S7). The treatment of  $\alpha$ -syn PFFs causes mitochondrial damage characterized by shrinkage, decreased oxygen consumption rate and elevated reactive oxygen species (ROS) levels in neurons, but the addition of GQDs ameliorates these adverse effects.

The role of GQDs on  $\alpha$ -syn PFF-induced Lewy body (LB)/Lewy neurite (LN)-like pathology was then evaluated. After 7 days of  $\alpha$ -syn PFF treatment, accumulation of  $\alpha$ -syn in the SDS-insoluble fraction was analysed by western blot, showing decreased phosphorylated  $\alpha$ -syn (p- $\alpha$ -syn) accumulation with GQDs (Fig. 3-3 d,e). In addition, p- $\alpha$ -syn immunoreactivity is increased in primary neurons by  $\alpha$ -syn PFFs, whereas it is barely detectable in primary neurons treated with GQDs as assessed by  $\alpha$ -syn phosphoserine 129 immunostaining (Fig. 3-3 f,g). To investigate the effect of treatment time on  $\alpha$ -syn pathology, GQDs were treated simultaneously with and 3 days pre/post  $\alpha$ -syn PFF additions. Though the toxicity amelioration and inhibition effects on p- $\alpha$ -syn accumulation were slightly weaker when GQDs were applied 3 days after  $\alpha$ -syn PFF injection, the collective results practically show consistent effects (Fig. 3-S8 a-f). To verify the cellular localization of the inhibitory effects of GQDs, GQDs,  $\alpha$ -syn PFFs and the lysosome were distinctively labelled with fluorescent probes for live imaging (Fig. 3-S8 g,h). As shown from the time-course snapshots, fluorescence signals for  $\alpha$ -syn PFFs and GQDs are co-localized within the lysosome, where the signal for  $\alpha$ -syn PFFs gradually decreases and that of GQDs increases with time. It can be presumed that both GQDs and  $\alpha$ -syn PFFs are endocytosed, and the disaggregation of fibrillized  $\alpha$ -syn takes place in the lysosome by the surrounding GQDs.

One of the key features of the  $\alpha$ -syn PFFs neuron model is neuron-to-neuron transmission of pathologic  $\alpha$ -syn aggregates<sup>5</sup>. To examine the effect of GQDs, a triple-compartment microfluidic culture device was used, where transmission between neurons takes place sequentially from C1 to C3 (Fig. 3-3 h). At 14 days post- $\alpha$ -syn PFF treatment, the levels of p- $\alpha$ -syn were visualized by immunostaining in all test chambers. The levels of p- $\alpha$ -syn immunoreactivity are

greatly reduced in C2 and C3 with the presence of GQDs in C1, which suggests that GQDs prevent the seeds of endogenous  $\alpha$ -syn from forming aggregates (Fig. 3-3 i,j). Also, the levels of p- $\alpha$ -syn immunoreactivity are lowered in C2 and C3 when GQDs are added to C2, indicating that GQDs block the transmission of pathologic  $\alpha$ -syn to neighbouring neurons.

To address whether GQDs possess neuroprotective effects against  $\alpha$ -syn PFF-induced transmission and toxicity *in vivo*,  $\alpha$ -syn PFFs were stereotactically injected into the striatum of wild-type (WT) mice and GQDs were administered biweekly (that is, every two weeks) via intraperitoneal (i.p.) injection (Fig. 3-4a). Foremost, we sought to verify the blood–brain barrier (BBB) permeability of GQDs by using an *in vitro* BBB model<sup>14</sup> (Fig. 3-S9 a,b). The form and functionality of the BBB model were subsequently confirmed by measuring the transepithelial electrical resistance (TEER) and dextran fluorescence intensity (Fig. 3-S9 c,d). The *in vitro* permeability of GQDs was then ascertained by measuring the fluorescence intensity on the brain side. Intriguingly, the fluorescence signal gradually increased with time, and showed 100% permeability after 24 h (Fig. 3-S9 e). To corroborate the penetration process visually, GQD–biotin was utilized and linked to streptavidin–quantum dots for live fluorescence imaging. Before the study, the functional behaviour of GQD–biotin was assessed, and was found to exhibit similar BBB penetration rates and fibril dissociation effects as those of pristine GQDs (Fig. 3-S9 e–g). Live fluorescence imaging showed that the GQD–biotin complex is localized in the lysosome of both brain microvascular endothelial cells (BMECs) and astrocytes, and disappears through the exosome (Fig. 3-S9 h,i). This suggests that GQDs are endocytosed into BMECs on the blood side and released, then subsequently endocytosed by astrocytes on the brain side and

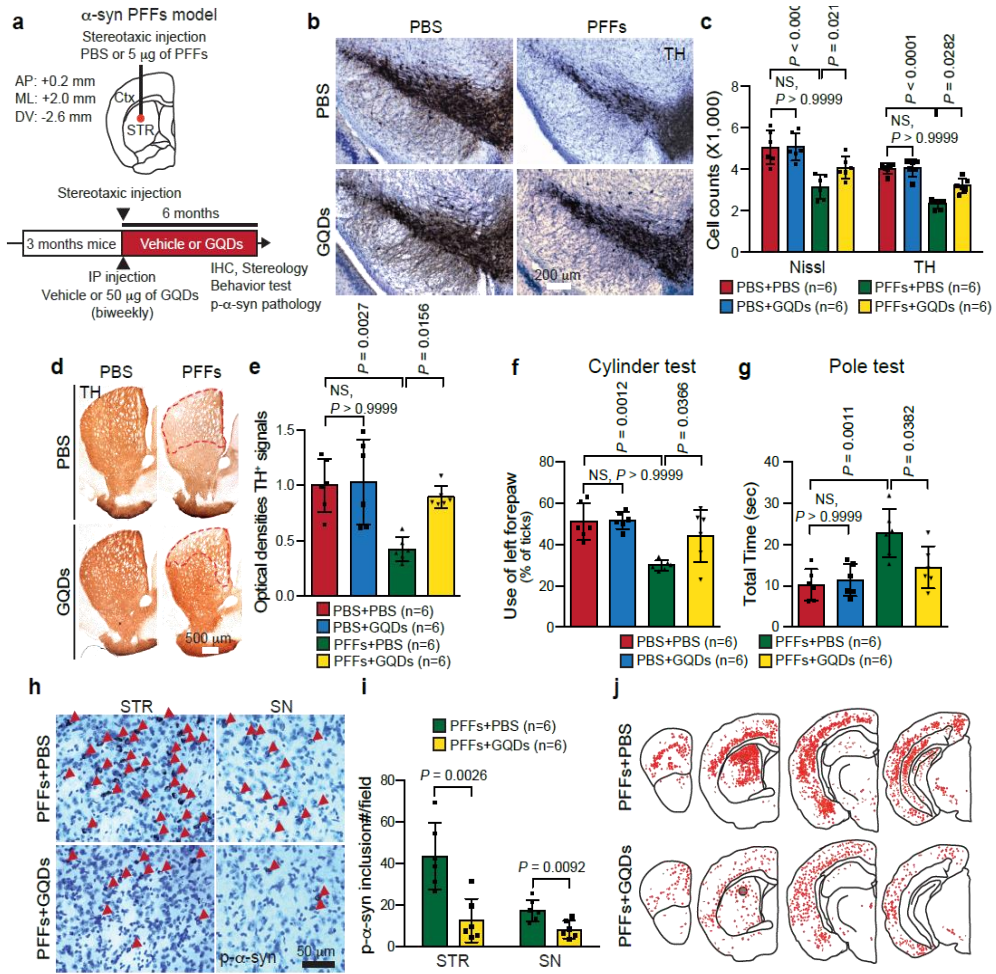


**Figure 3-4.** Effect of GQDs on  $\alpha$ -syn-induced pathologies *in vivo*. a, Schematic illustration of injection coordinates of  $\alpha$ -syn PFFs (5  $\mu$ g) for stereotaxic intrastriatal injection in C57BL/6 mice. As a treatment, 50  $\mu$ g of GQDs or PBS were i.p. injected biweekly for 6 months. AP, anteroposterior; ML, mediolateral; DV, dorsoventral; Ctx, cortex; STR, striatum; IHC, immunohistochemistry. b, Representative TH immunohistochemistry images in the substantia nigra of  $\alpha$ -syn PFF-injected hemisphere in the absence (top) and presence (bottom) of GQDs. c, Stereological counting of the number of TH- and Nissl-positive neurons in the substantia nigra via unbiased stereological analysis after 6 months of  $\alpha$ -syn PFF injection with and without GQDs injection. Mean values are 5,061, 5,096, 3,155 and 4,080 Nissl-positive neurons; 4,039, 4,068, 2,327 and 3,221 TH-positive neurons (n=6 biologically independent animals; two-way ANOVA with a post hoc Bonferroni test; NS, not significant; error bars are s.d.). d, Representative TH immunohistochemistry images in the striatum of  $\alpha$ -syn PFF-injected hemisphere. e, Quantifications of TH-immunopositive fibre densities in the striatum. Mean values for relative optical densities of TH<sup>+</sup> signals are

1.00, 1.03, 0.42 and 0.90 for PBS + PBS, PBS + GQDs, PFFs + PBS and PFFs + GQDs (n=6 biologically independent animals; two-way ANOVA with a post hoc Bonferroni test; NS, not significant; error bars are s.d.). f, Assessments of the behavioural deficits measured by the use of forepaws in the cylinder test. Mean values (% of ticks) are 51.00, 51.67, 29.83 and 44.17 for PBS + PBS, PBS + GQDs, PFFs + PBS, and PFFs + GQDs (n=6 biologically independent animals; two-way ANOVA with a post hoc Bonferroni test; NS, not significant; error bars are s.d.). g, Assessments of the behavioural deficits measured by the ability to grasp and descend from a pole. Mean values are 10.25, 11.38, 22.73 and 14.43 s for PBS + PBS, PBS + GQDs, PFFs + PBS and PFFs + GQDs (n=6 biologically independent animals; two-way ANOVA with a post hoc Bonferroni test; NS, not significant; error bars are s.d.). h, Representative p- $\alpha$ -syn immunostaining images in the striatum (STR) and substantia nigra (SN) of  $\alpha$ -syn PFF-injected hemisphere. i, Quantifications of p- $\alpha$ -syn immunoreactive neurons in the striatum and substantia nigra. Mean values (number of inclusions) are 43.33 and 12.50 for PFFs + PBS and PFFs + GQDs of striatum (STR); 17.67 and 8.00 for PFFs + PBS and PFFs + GQDs of substantia nigra (n=6 biologically independent animals; two-tailed Student's t-test; error bars are s.d.). j, Distribution of LB/LN-like pathology in the CNS of  $\alpha$ -syn PFF-injected hemisphere (p- $\alpha$ -syn positive neurons, red dots; p- $\alpha$ -syn positive neurites, red lines).

released through the exosome. The *in vivo* permeability of the BBB was studied by using GQD–biotin for immunohistochemical analysis of the brain. After i.p. injection, a considerable amount of GQD–biotin was detected in the entire central nervous system (CNS) region, including the olfactory bulb, neocortex, midbrain and cerebellum, indicating that GQDs also have the ability to penetrate the BBB *in vivo* (Fig. 3-S9 j–n).

At 180 days post- $\alpha$ -syn PFF injection, decreased tyrosine hydroxylase (TH)- and Nissl-positive neurons in the substantia nigra are observed in WT mice. On the other hand, mice administered with GQDs are protected against  $\alpha$ -syn PFF-induced loss of dopaminergic neurons (Fig. 3-4 b,c). Furthermore,  $\alpha$ -syn PFFs provoke a loss of TH-positive striatal fibre neurons, while GQDs also prevent loss in the striatum (Fig. 3-4 d,e). Finally, changes in the behavioural deficits were

assessed by cylinder and pole tests. Mice with GQD injection exhibited alleviated motor deficit, showing balanced use of both forepaws and decreased pole descending time, respectively, in the cylinder and pole tests (Fig. 3-4 f,g).

The levels of p- $\alpha$ -syn, a marker of LBs/LNs, were visualized in the striatum and substantia nigra of  $\alpha$ -syn PFF-injected mice. Stereotactically injected  $\alpha$ -syn PFFs provoke accumulation of p- $\alpha$ -syn in the striatum and substantia nigra, but administration of GQDs reduces p- $\alpha$ -syn levels (Fig. 3-4 h,i). The injection of  $\alpha$ -syn PFFs in the striatum also leads to propagation of  $\alpha$ -syn aggregates throughout the CNS region, whereas GQDs inhibit the transmission of pathological  $\alpha$ -syn (Fig. 3-4 j). In addition, GQDs injection ameliorates  $\alpha$ -syn PFF-induced gliosis in the substantia nigra accompanying decreased microglia density and glial fibrillary acidic protein (GFAP) levels in astrocytes (Fig. 3-S10). To further corroborate the therapeutic potential of GQDs against a transgenic *in vivo* Parkinson's disease model, 6 month human A53T  $\alpha$ -syn transgenic mice<sup>15</sup> were administered biweekly with GQDs for 4 months (Fig. 3-S11 a). Similar to the  $\alpha$ -syn PFF-induced model, GQDs administration reduces p- $\alpha$ -syn levels in the CNS region (Fig. 3-S11 b–d), as well as the microglia density and GFAP levels in astrocytes in the transgenic model (Fig. 3-S11 h–k). GQDs treatment also reduces the  $\alpha$ -syn aggregates induced by overexpression of human A53T  $\alpha$ -syn in HEK293 cells<sup>16</sup> (Fig. 3-S11 l,m). GQDs alleviate behavioural defects in the hA53T  $\alpha$ -syn Tg mice as well, as monitored by the pole and clasping tests (Fig. 3-S11 e–g). It must be noted that there is no loss of dopamine neurons, glial cells activation, behavioural abnormalities and organ damage in mice with 6 months of prolonged GQDs injection, demonstrating that GQDs manifest no appreciable long-term *in vitro* and *in vivo* toxicity and can be cleared from the body and excreted into urine

(Fig. 3-S12).

A few previous reports have discussed the potential therapeutic role of graphene oxides (GOs) and GQDs against Alzheimer's disease by inhibiting the fibrillization of beta-amyloid (A $\beta$ ) peptides<sup>17–19</sup>. In addition, computational evidence suggests that a hydrophobic graphene sheet could cause the destruction of amyloid fibrils<sup>20</sup>. To compare the therapeutic efficacy of GQDs with the results of previous studies, nano-sized GOs (nano-GOs, ranging from ~5 to 20 nm) and reduced GQDs (rGQDs) were prepared (Fig. 3-S13 a,b). As shown from the Fourier-transform infrared (FT-IR) spectra, pristine GQDs exhibit abundant carboxyl groups, while nano-GOs and rGQDs show much lower carboxyl group:aromatic carbon double bond ratios. The difference in the carboxyl functional group contents is directly reflected in cell viability assays, where nano-GOs and rGQDs show serious *in vitro* toxicities, unlike GQDs (Fig. 3-S13 c,d). Moreover, nano-GOs and rGQDs exhibit considerably weaker fibril-dissociation effects than GQDs (Fig. 3-S13 e–g). This can presumably be attributed to the presence of fewer carboxyl functional groups as well, as we have verified from the <sup>1</sup>H–<sup>15</sup>N HSQC analysis that the positively charged N-terminal region is the initial, but chief binding site with GQDs. It must also be noted that the BBB permeability of nano-GOs is much lower than that of GQDs and rGQDs, suggesting that size may be a decisive factor for the BBB permeability of graphene-based nanoparticles (Fig. 3-S13 h). Collectively, our results show that GQDs are the optimal therapeutic candidate for anti-Parkinson's disease and related  $\alpha$ -synucleinopathies therapy, with no appreciable *in vitro* and long-term *in vivo* toxicity, respectable fibril dissociation effects, and the ability to pass through the BBB.

### 1.3. Conclusion

To open new venues in clinical drug development against Parkinson's disease, a candidate desirably features outstanding anti-aggregation and dissociation properties towards  $\alpha$ -syn aggregates, without severe toxicity. GQDs are found to bind to  $\alpha$ -syn fibrils, inhibit transmission and possess unique neuroprotective effects against the neuropathological  $\alpha$ -syn aggregates/fibrils in both *in vitro* and *in vivo* models. It is expected that GQD-based drugs with appropriate modifications might provide a clue to support the development of new therapeutic agents for abnormal protein aggregation-related neurological disorders including Parkinson's disease.

### 1.4. Experimental

**Preparation of GQDs.** GQDs were synthesized by placing 0.9 g of carbon fibres (Carbon Make) in a mixture of strong acid (300 ml sulphuric acid and 100 ml nitric acid; Samchun Chemical) at 80 °C for 24 h. After acid removal, the solution was vacuum-filtered with a porous inorganic membrane filter (cat. no. 6809-5002, Whatman-Anodisc 47; GE Healthcare) to discard large particles. The solution was then subjected to rotary evaporation to yield the final product in powder form.

**AFM imaging.** For AFM imaging, 5  $\mu$ l of GQDs (10  $\mu$ g/ml) and  $\alpha$ -syn fibrils (10  $\mu$ g/ml) were prepared on a silicon substrate. The analyses were performed with an XE-100 AFM (Park Systems) via non-contact mode (scan size: 25  $\mu$ m<sup>2</sup> and scan rate: 0.8 Hz). The images were acquired by equipped XE data acquisition program (XEP 1.8.0).

**FT-IR measurements.** The samples were prepared through the conventional KBr



pellet method (no. of scans, 32; resolution, 4; wavenumber range, 4,000–40 cm<sup>-1</sup>).

The analysis was performed with a Nicolet 6700 FT-IR spectrometer (Thermo Scientific).

**ThT and turbidity assays.** Turbidity and ThT assays were used for the measurement of  $\alpha$ -syn fibrils. For the ThT assay, 50  $\mu$ l of each sample was centrifuged at 16,000 g for 30 min. The pellet was then re-suspended in 200  $\mu$ l of ThT assay solution consisted of 25  $\mu$ M ThT (cat. no. T3516, Sigma-Aldrich) in 10 mM glycine buffer (pH 9.0). The amount of  $\alpha$ -syn fibrils was determined by a fluorescence spectrophotometer with the ThT fluorescence measured at 482 nm (excitation at 440 nm). For the turbidity assay,  $\alpha$ -syn fibrils were diluted with PBS (1:10). The diluted  $\alpha$ -syn fibrils were loaded into the wells of Corning 96-well plates. The turbidity of each sample was determined by a microplate reader (absorbance at 360 nm).

**TEM imaging.** The  $\alpha$ -syn fibrils were adsorbed to glow discharge grids (EMS, 400 mesh carbon-coated copper grids) for 2 min and rinsed with three drops of Tris-HCl (50 mM, pH 7.4). The rinsed grids were floated with two drops of 0.75% uranyl formate. After drying, the images were captured by a Phillips CM 120 TEM (80 kV) with an AMT ER-80 charge-coupled device (8 megapixel). For primary cultured neurons, cells were seeded onto a poly-d-lysine-coated 35 mm dish at a density of 100,000 cells per well. Neurons were treated with 1  $\mu$ g/ml of PFFs with or without 1  $\mu$ g/ml of GQDs at days *in vitro* (DIV) 10. At DIV 17, cells were washed with 1% sodium nitrite containing PBS (pH 7.4) and fixed with 3% PFA, 100 mM cacodylate, 1.5% glutaraldehyde, 2.5% sucrose containing fixative (pH 7.4) for 1 h. TEM images were captured by a Philips EM 410 TEM with a Soft Imaging System Megaview III digital camera.

**Dot-blot assays.** Tris-buffered saline (TBS)-wetted nitrocellulose membrane (NC membrane, 0.45  $\mu$ m pore) was mounted on the Bio-Dot microfiltration apparatus (cat. no. 1706545, Bio-Rad). The samples were loaded into the wells of a microfiltration apparatus under mild vacuum. After washing with TBS, the NC membranes were blocked with 0.5% Tween-20 and 5% non-fat dry milk containing TBS blocking buffer and attached with anti- $\alpha$ -syn filament antibody (cat. no. ab209538, 1:1,000, abcam) at 4 °C for 12 h. After incubation with horseradish peroxidase (HRP)-conjugated rabbit second antibodies (GE Healthcare) at room temperature for 1 h, the signals from  $\alpha$ -syn aggregates were then visualized by enhanced chemiluminescence (ECL) solution. The data were analysed with ImageJ software (<http://rsb.info.nih.gov/ij/>, NIH).

**BN-PAGE and SDS-PAGE.** For BN-PAGE,  $\alpha$ -syn fibrils and  $\alpha$ -syn PFFs were prepared using a NativePAGE sample prep kit (cat. no. BN2008, Life Technologies) and run on NativePAGE Novex 4–16% bis-tris protein gels (cat. no. BN1002Box, Life Technologies) at 200 V for 90 min. Then, 50 mM tricine, 15 mM Bis-Tris, 0.02% Brilliant Blue G (pH 7.0) containing cathode buffer and 50 mM Bis-Tris (pH 7.0) containing anode buffer were used for BN-PAGE. After BN-PAGE, gels were stained with a SilverQuest silver staining kit (cat. no. LC6070, Life Technologies), following the manufacturer's protocols. For SDS-PAGE, 10 DIV cortical neurons were treated with  $\alpha$ -syn PFFs (5  $\mu$ g/ml) in the presence and absence of GQDs (5  $\mu$ g/ml) for 7 days. At DIV 17, the soluble proteins were isolated from the neurons with a 1% TX-100, protease inhibitors and phosphatase inhibitors cocktail (cat. no. PPC1010, Sigma-Aldrich) containing sample buffer. For insoluble protein isolation, the lysates of neurons were sonicated and centrifuged at 12,000 g for 30 min at 4 °C. The remaining pellet was

washed and suspended in 2% SDS containing PBS for preparation of insoluble protein. Laemmli sample buffer (2×, cat. no. 1610737, Bio-Rad) was used to dilute the soluble and insoluble protein samples. For SDS-PAGE, 20 µg of soluble or insoluble proteins was loaded onto the wells of Novex 8–16% tris-glycine gel (cat. no. XP08160BOX, Life Technologies) and electrophoresis was performed at 130 V for 85 min. After transfer of proteins onto the NC membrane, it was blocked with 0.1% Tween-20 and 5% non-fat dry milk containing TBS for 1 h and incubated at 4 °C overnight with SNAP25 (cat. no. 111-002, 1:2,000, Synaptic Systems), VAMP2 (cat. no. ab3347, 1:1,000, abcam) or anti-pS129- $\alpha$ -syn antibodies (cat. no. ab59264, 1:1,000, abcam). The NC membranes were then incubated with HRP-conjugated mouse or rabbit secondary antibodies (GE Healthcare) at room temperature for 1 h and visualized by ECL solution. The signals were measured by ImageJ software (<http://rsb.info.nih.gov/ij/>, NIH).

**Preparation of sonicated  $\alpha$ -syn PFFs.** The  $\alpha$ -syn PFFs were prepared following the method published in ref. 21. Briefly, full-length mouse recombinant  $\alpha$ -syn was cloned using the pRK172 bacterial expression vector. The plasmids were then transformed into BL21(DE3)RIL-competent *Escherichia coli* (cat. no. 230245, Life Technologies). The  $\alpha$ -syn monomers were purified through several steps including dialysis, anion exchange and size exclusion chromatography after bacterial growth. *In vitro*  $\alpha$ -syn fibrils were assembled in an Eppendorf orbital mixer (cat. no. 538400020) under specific agitation conditions (1,000 r.p.m., 37 °C, 7 days). For the formation of preformed fibrils,  $\alpha$ -syn fibrils were sonicated for a total of 60 pulses (20% amplitude, 0.5 s on, 0.5 s off) with a 1/8'' probe sonicator.

**Biotinylation of GQDs and binding assay.** GQDs (50 mg) were dissolved in conjugation buffer (pH 4.7), and 12.5 mg of EDC reagent (N-(3-

dimethylaminopropyl)-N''-ethylcarbodiimide hydrochloride; cat. no. 03449, Sigma-Aldrich) was subsequently added to replace the carboxyl groups. After 1 h of reaction with vigorous stirring, 25 mg of EZ-Link amine-PEG3-biotin (cat. no. 21347; Thermo Scientific) was added to EDC-activated GQDs. The solution was then subjected to dialysis and rotary evaporation to yield the final product in powder form. For the binding assay between GQDs and  $\alpha$ -syn fibrils, 5 mg/ml of  $\alpha$ -syn fibrils were incubated with 5 mg/ml of biotinylated GQDs and streptavidin conjugated 0.8 nm ultra-small gold particles (cat. no. 800.099, Aurion) for 1 h. Next, the streptavidin-conjugated ultra-small gold particles bound with high affinity to biotinylated-GQDs were enhanced with GoldEnhance EM Plus solution (cat.no. 2114, Nanoprobes) for 5 min. Non-reacted solution was removed by a 100 kDa molecular weight cut-off spin column (cat. no. UFC510024, Millipore-Sigma), followed by TEM analysis.

**Purification of  $^{15}\text{N}$ -labelled  $\alpha$ -syn.** The  $\alpha$ -syn gene cloned in pRK172 vector was transformed into E. coli BL21 (DE3) for  $\alpha$ -syn overexpression. For the preparation of isotope-labelled  $\alpha$ -syn, cells were grown in M9 minimal medium containing 0.5 g of  $^{15}\text{NH}_4\text{Cl}$  and 1 g of  $^{13}\text{C}$  glucose (Cambridge Isotope Laboratory) per litre at 37 °C with 100  $\mu\text{g/ml}$  ampicillin. After induction with isopropyl  $\beta$ -d-1 thiogalactopyranoside (IPTG), the heat-treated cell lysate was subjected to successive purifications using DEAE-Sephacel anion-exchange, Sephacryl S-200 size-exclusion and S-Sepharose cation-exchange chromatography. The purified  $\alpha$ -syn was dialysed against 12 L of fresh 20 mM 2-(N-morpholino)ethanesulfonic acid (MES) buffer (pH 6.5) three times, and stored in aliquots at a concentration of 1 mg/ml at -80 °C. The sample was concentrated to 5 mg/ml using Nanosep 10K membrane (Pall Gelman) at 4 °C immediately before the experiments.

**NMR spectroscopy analysis.** A detailed NMR study of the interaction between  $\alpha$ -syn and GQDs was performed using a 950 MHz spectrometer equipped with a cryo-genic probe (Bruker).  $^{15}\text{N}$ -labelled  $\alpha$ -syn (5 mg/ml, 100  $\mu\text{l}$ ) was reacted with GQDs (5 mg/ml, 100  $\mu\text{l}$ ) under 37 °C shaking incubation at 1,000 r.p.m. for 3 days.  $^{15}\text{N}$ -labelled  $\alpha$ -syn samples were prepared using 20 mM MES buffer (pH 6.5) containing 10% for  $^1\text{H}$ - $^{15}\text{N}$  HSQC measurements.  $^1\text{H}$ - $^{15}\text{N}$  HSQC spectra of both  $\alpha$ -syn and GQD-reacted  $\alpha$ -syn were acquired at 37 °C. The obtained data were processed by NMRPipe<sup>22</sup> and analysed by Sparky<sup>23</sup>.

**Simulation details.** The MS simulation (200 ns) was performed with Gromacs 5.1 to examine the interaction between GQDs and  $\alpha$ -syn fibrils at the molecular level<sup>24</sup>. The initial structure of the hydrophobic NAC domain (residues 71–82) of  $\alpha$ -syn was adapted from the ssNMR structure (PDB ID: 2N0A) with CHARMM forcefield<sup>25</sup>, and the structure of the GQDs was designed with CGenFF<sup>26</sup> by protocols from <https://cgenff.paramchem.org>.

**CD measurements.** The  $\alpha$ -syn fibrils (5 mg/ml, 100  $\mu\text{l}$ ) were mixed with GQDs solution (5 mg/ml, 100  $\mu\text{l}$ ) and depolymerized under 37 °C shaking incubation at 1,000 r.p.m. for 7 days. For far-ultraviolet CD measurements, the sample was diluted (1/2) with deionized water. CD spectra between 190 and 260 nm were measured at 0.5 nm intervals using a J-815 spectropolarimeter (Jasco) and a 0.2-mm-path-length quartz cuvette. The spectrum of the buffer solution was subtracted from the sample spectra. CD signals were normalized to the mean residue ellipticity,  $[\theta]$ , with units of  $\text{deg cm}^2 \text{dmol}^{-1}$ . The fractional secondary structure contents of the  $\alpha$ -syn fibrils and depolymerized  $\alpha$ -syn fibrils were calculated using the algorithm of CONTIN/LL on the DichroWeb online server (<http://dichroweb.cryst.bbk.ac.uk>). For the calculation using CONTIN/LL,

reference set 7 on Dichroweb was employed, which is optimized for the wavelength range 190–240 nm.

**Primary neuron culture.** Primary cortical neurons were isolated from the brain of embryonic day 15 C57BL/6 mice (Charles River) and seeded onto poly-d-lysine-coated dishes (cat. no. P6407, Sigma-Aldrich). The cultured neurons were maintained with complete culture medium composed of B27 supplement (cat. no. 17504044, Life Technologies), L-glutamine (cat. no. 25030149, Life Technologies) and neurobasal medium (cat. no. 21103049, Life Technologies) at 37 °C in a 7% CO<sub>2</sub> incubator. To inhibit the growth of glial cells in the neuron culture, 30 µM of 5-fluoro-2'-deoxyuridine (cat. no. F0503, Sigma-Aldrich) was added after 5 days of culture.

**Cell viability and cytotoxicity assays.** For cell viability and cytotoxicity assays, primary cortical neurons were seeded onto poly-d-lysine-coated glass coverslips at a density of 10,000 cells per cm<sup>2</sup>. The cells were then incubated in a 7% CO<sub>2</sub> incubator at 37 °C with complete neuronal culture medium. The cytotoxicity was measured with α-syn PFFs (1 µg/ml) in the absence and presence of GQDs (1 µg/ml) in 10 DIV primary mouse cortical neurons for 7 days. An LDH cytotoxicity assay kit (cat. no. 88954, Pierce) and TUNEL assay kit (cat. no. 12156792910, Roche) were used to measure cytotoxicity. The viability of mouse primary cortical neurons and SH-SY5Y cells was determined using an alamarBlue cell viability assay kit (cat. no. DAL1025, Molecular Probes) and a neurite outgrowth staining kit (cat. no. A15001, Molecular Probes), following the manufacturers' instructions.

***In vitro* immunofluorescence.** Mouse primary cortical neurons were seeded at a density of 20,000 cells per cm<sup>2</sup> onto poly-d-lysine-coated glass coverslips. After the cells were fixed with 4% PFA and blocked with 5% normal donkey serum

(NDS; cat. no. 017-000-121, Jackson ImmunoResearch), 2% bovine serum albumin (BSA; cat. no. A7030, Sigma-Aldrich) and 0.1% Triton X-100 (cat. no. T8787, Sigma-Aldrich) containing PBS at room temperature for 1 h. Subsequent incubations with anti-8-OHG (cat. no. ab62623, 1:1,000, abcam), anti-pS129- $\alpha$ -syn (cat. no. ab59264, 1:1,000, abcam) and anti-MAP2 (cat. no. MAB3418, 1:1,000, Millipore) antibodies were carried out overnight at 4 °C. The coverslips were washed with 0.1% Triton X-100 containing PBS and incubated with a mixture of FITC-conjugated (donkey anti-rabbit FITC, cat. no. 711-095-152; donkey anti-mouse FITC, cat. no. 715-095-151, Jackson ImmunoResearch) and Cy3-conjugated (donkey anti-rabbit CY3, cat. no. 711-165-152; donkey antimouse CY3, cat. no. 715-165-151, Jackson ImmunoResearch) second antibodies at room temperature for 1 h. The fluorescence images were captured using a Zeiss LSM 710 confocal microscope.

**Microfluidic chambers.** Before being fixed to the microfluidic devices (triple-chamber microfluidic devices, cat. no. TCND1000, Xona), the rectangular glass coverslips were prepared according to the method of ref. 5. Each chamber was plated at a density of 100,000 cells per chamber. At DIV 7, 0.5  $\mu$ g of GQDs were added to chamber 1 (C1) or chamber 2 (C2) before treatment with 0.5  $\mu$ g  $\alpha$ -syn PFFs to C1. To regulate the direction of flow of the channels, a 50  $\mu$ l difference in media volume was controlled through the chambers. At DIV 21, neurons in the chambers were fixed with 4% PFA containing PBS and blocked with 0.1% Triton X-100, 5% NDS and 2% BSA containing PBS at room temperature for 1 h. The chambers were then incubated with anti-pS129- $\alpha$ -syn (cat. no. ab59264, 1:1,000, abcam) and anti-MAP2 (cat. no. MAB3418, 1:1,000, Millipore) antibodies at 4 °C, overnight. After washing the chambers with 0.1% Triton X-100 containing PBS,

the chambers were incubated in a mixture of FITC-conjugated (Jackson ImmunoResearch) and Cy3-conjugated (Jackson ImmunoResearch) second antibodies for 1 h at room temperature. The fluorescent images were captured using a LSM 710 Zeiss confocal microscope.

**Complex I activity assay.** The commercial microplate assay kit (Cat#: ab109721; abcam) was used for measuring the complex I enzyme activity, following the manufacturer's instruction. Briefly, primary cortical neurons were plated onto poly-d-lysine coated 6 cm dishes at a density of 1,000,000 cells/dish. Neurons were then treated with 1  $\mu\text{g/ml}$  of  $\alpha\text{-syn}$  PFFs with or without 1  $\mu\text{g/ml}$  of GQDs at 10 days *in vitro*. After 7-day treatment, the cytosolic proteins were extracted using 1/10 volume detergent in PBS. The supernatant was isolated by centrifuging at  $12,000 \times g$  for 20 mins from 5.5 mg/ml of samples. Isolated samples were loaded and incubated for 3 hours at RT, and rinsed twice with washing buffer. After adding a 200  $\mu\text{l}$  assay solution, the mitochondrial complex I enzyme activity was measured at approximately 1-min intervals for 30 mins.

**Mitochondrial morphology assessment.** Primary cultured cortical neurons were plated onto poly-d-lysine coated glass coverslips at a density of 10,000 cells/cm<sup>2</sup>. The neurons were treated with 1  $\mu\text{g/ml}$  of  $\alpha\text{-syn}$  PFFs with or without 1  $\mu\text{g/ml}$  of GQDs at days *in vitro* (DIV) 10. At DIV 17, the mitochondria in neurons were stained with the MitoTracker® Orange CMTMRos probes (Cat#: M7510; Life technologies). Briefly, mitochondria were stained with the 100 nM of MitoTracker® Orange CMTMRos probes for 30 mins. After washing the stained mitochondria with a live cell imaging solution (Cat#: A1429DJ; Life technologies), the mitochondrial morphological characteristics were captured using a Zeiss confocal microscope (LSM 710). The length or aspect ratio (AP, the ratio between



the major and minor axis) were measured by ImageJ software (<http://rsb.info.nih.gov/ij/>, NIH).

**Determination of oxygen consumption rate.** The Seahorse XF cell mito stress test kit (Cat#: 103015; Agilent) was used for measuring the oxygen consumption rate (OCR). Briefly, the primary cultured cortical neurons were plated onto the 24 well culture plate at a density of 500,000 cells/well. Neurons were treated with 1  $\mu\text{g/ml}$  of  $\alpha\text{-syn}$  PFFs with or without 1  $\mu\text{g/ml}$  of GQDs at DIV 10. At DIV 17, the neurons were incubated in complete Seahorse assay medium at 37 °C for 1 hour after washing with warmed PBS. The assay plate was then loaded in an XF24 analyser (XF24 EX extracellular flux analyser, Seahorse Bioscience) and the OCR was calculated. The OCR was measured with specific measurement protocol (1-min mix, 1-min wait, and 2-min measurement). To assess the coupling of respiratory, chain, the basal respiration, and mitochondrial respiratory capacity, Oligomycin, carbonyl canide m-chlorophenylhydrazine (CCCP), and rotenone were sequentially injected to the Seahorse assay plate. The measured OCRs were normalised relative to the protein concentration in each well. Data are presented as the percentage of change as compared with control.

**Live imaging.** Primary cortical neurons were seeded onto poly-d-lysine coated glass bottom dish (Cat#: 150682; Nunc™) at a density 10,000 cells/  $\text{cm}^2$  and maintained in a 7%  $\text{CO}_2$  incubator at 37 °C. At DIV 7, the neurons were treated with 1  $\mu\text{g/ml}$  FITC labelled  $\alpha\text{-syn}$ -PFFs, 1  $\mu\text{g/ml}$  GQDs-biotin and streptavidin Qdot complex, and 100 nM LysoTracker™ Blue DND-22 (Cat#: L7525; Life technologies) containing live cell imaging solution for 1 hour. For time-lapse confocal live imaging, the temperature controlled  $\text{CO}_2$  incubation system equipped confocal microscope was used. The culture dish was mounted and time-lapse

images were taken at the indicated intervals with 488 nm and 561 nm laser excitations.

***In vitro* BBB permeability of GQDs.** For *in vitro* BBB experiments, 10-pups of C57BL/6 mouse were used for preparing primary mouse astrocytes as previously described<sup>30</sup>. Briefly, the cerebral cortex was isolated from 1-d-old C57BL/6 mice and the meninges were removed. The cerebral cortex was mechanically disrupted by 30-ml syringe with 19-gauge needle. The isolated cells were plated onto 75 cm<sup>2</sup> T-flasks with complete DMEM culture medium. After 2 weeks, the 95% pure astrocytes were isolated by an astrocyte isolation kit (Cat#: 130-096-053; Miltenyl Biotec). The primary brain microvascular endothelial cells (BMEC) from C57BL/6 mice were purchased from Cell Biologics as well. The purities of cultured astrocytes (>95%) and BMEC (>95%) were confirmed by fluorescence staining with cell specific marker GFAP (for astrocyte) and CD31 (for BMEC, Cat#: ab28364; 1:500; abcam). For the formation of an *in vitro* BBB, the isolated astrocytes were seeded at a density of 106 cells/ml onto the underside of the inserts (collagen-coated 0.4  $\mu$ m transwell inserts; Cat#: CLS3491; Sigma-Aldrich) and incubated for 48 hours at 37 °C in 5% CO<sub>2</sub> incubator. The inserts were then placed carefully into a 6-well plate where BMEC were plated at a density of 106 cells/ml on top of the inserts. The transepithelial electrical resistance (TEER) was determined to confirm the structural integrity of the *in vitro* BBB by the epithelial volt/ohm (TEER) meter (Cat#: 300523; EVOM2; world precision instruments) at 0, 2, 4, 6, and 8 days after BMEC seeding. BBB impermeable 3 kDa dextranfluorescein (Cat#: D3306; Life technologies) were loaded inside (the blood side) of the *in vitro* BBB to confirm the integrity and calculated the ratio using fluorescence spectrophotometer (Ex=494 nm / Em=521 nm for dextran-

fluorescein; Ex=555 nm / Em=580 nm for dextran rhodamine). The concentrations of remaining GQDs, GQDs-biotin, nano-GOs, and rGQDs were measured at 520 nm (Ex=310 nm) using the FluoroBrite™ DMEM media (Cat#: A1896701; Life technologies) of inside (the blood side) and outside (the brain side) of the inserts.

**Exosome isolation.** To measure the concentration of GQDs-biotin from the released exosome, BMEC or astrocytes were plated on 6 cm dishes and 5 µg of GQDs-biotin were treated for 12 hours. After 12 hours, the culture medium was changed, and the exosomes were isolated using an exosome isolation reagent (Cat#: 4478359; ThermoFisher) after 24 and 48 hours.

**Animals.** All animal-based experimental procedures followed the guidelines of the Laboratory Animal Manual of the NIH Guide to the Care and Use of Animals. The procedures were approved by the Animal Care and Use Committee of Johns Hopkins Medical Institute. The human  $\alpha$ -syn-A53T transgenic mice (stock no. 006823, B6.Cg-Tg, Prnp-SNCA\*A53T;23Mkle/J) were purchased from the Jackson Laboratory<sup>27</sup>.

***In vivo* BBB permeability of GQDs.** For *in vivo* immunostaining of GQDs-biotin, 8-week old C57BL/6 mice were i.p. injected with 2 mg/kg GQDs-biotin. The removed brains were fixed with 4% PFA for 6 hours. The brains were then stored in 30% sucrose for 48 hours for the following immunohistochemical staining. The biotin signals of the olfactory bulb, neocortex, midbrain and cerebellum were visualised using DAB staining kit. The GQDs-biotin positive signals in cells of the aforementioned regions were confirmed by immune-EM staining using GoldEnhance™EM Plus solution with 20-min incubation, following the manufacturer's instructions. For *in vivo* BBB experiments, 8-week old C57BL/6 mice were i.p. or i.v. injected with GQDs-biotin (2 mg/kg) or vehicle. At 7 days,

and 14 days, the brain and blood were harvested, and the brain was homogenated with 1% TX-100 in PBS. The plasma was prepared by clot removed with centrifuging at  $2,000 \times g$  for 10 mins after the whole blood storing at RT for 30 mins. The concentrations of GQDs-biotin were measured using QuantTag Biotin Kit (Cat# BDK-2000, Vector Laboratories). The ratio of brain/plasma concentration of GQDs-biotin was calculated against the brain/plasma ratio.

**$\alpha$ -syn aggregation formation assay.** HEK293T cells were purchased from American Type Culture Collection (ATCC) and authenticated by STR analysis. HEK293T cells were routinely tested and found to be negative of mycoplasma contamination. HEK293T cells were seeded on glass coverslides and transfected the pCMV5 vectors with myc-tagged A53T  $\alpha$ -syn mutant (kindly gifted by Dr. Thomas C. Südhof), followed by treatment with PBS (pH 7.4) or GQDs (0.1  $\mu\text{g/ml}$ ). 48 hours after the treatment, cells were washed three times with PBS and fixed for 20 mins at RT in 4% PFA containing PBS. The fixed cultures were permeabilised for 4 mins in 0.1% Triton X-100 containing PBS. The expression of  $\alpha$ -syn was monitored by immunostaining with  $\alpha$ -syn antibody (Cat#: 610787; 1:1,000; BD Biosciences). The subcellular localisation of  $\alpha$ -syn aggregates were determined by the confocal microscopy with serial excitations at 550 nm and 570 nm. The number of  $\alpha$ -syn aggregates per field was measured using ImageJ software (<http://rsb.info.nih.gov/ij/>, NIH).

**Stereological assessments.** C57BL/6 mice (8- to 10-week-old males) for stereological injection were purchased from the Jackson Laboratory. After anaesthetizing with 60 mg/kg of pentobarbital sodium solution, mice were injected with PBS (2  $\mu\text{l}$ ) or PFFs (5  $\mu\text{g}$  per 2  $\mu\text{l}$ ) by stereotaxic instruments (cat. no. Model 900, David KOPF instruments). The designated coordinate of the injection site of

the striatum was + 2.0 mm from the midline, + 2.6 mm beneath the dura, and + 0.2 mm relative to the bregma. As a treatment, 50  $\mu$ l of GQDs (50  $\mu$ g per mouse) were i.p. injected for 6 months on a biweekly (every two weeks) basis. After 6 months of GQDs injection, mice were perfused and fixed with 4% PFA containing PBS for 12 h, followed by cryoprotection with 30% sucrose. For TH and Nissl staining, 50  $\mu$ m coronal sections were cut using a cryostat (Bio-Rad), and every fourth section was used for stereological assessment. Sections were incubated with rabbit polyclonal anti-TH (cat. no. NB300-19, 1:1,000, Novus Biologicals) or rabbit polyclonal anti-pS129- $\alpha$ -syn (cat. no. ab59264, 1:1,000, abcam) with 5% NDS, 0.1% TX-100 containing PBS blocking solution. The sections were then incubated with streptavidin-conjugated HRP and biotinylated secondary antibodies (cat. no. PK-6101, Vector Laboratories). Immune-positive signals were visualized using a DAB kit (cat. no. SK-4100, Vector Laboratories). To identify the Nissl substance, the TH-stained tissues were counterstained with thionin-containing staining solution. The total number of TH- and Nissl-positive neurons in the SN region was quantified by microscopy with Stereo Investigator software (MBF Bioscience).

***In vivo immunohistochemistry.*** The isolated brains were perfused and fixed with 4% PFA containing PBS. After cryoprotection with 30% sucrose, mouse brain sections were incubated with anti-GFAP (cat. no. Z0334, 1:2,000, Dako) or anti-Iba-1 (cat. no. 019-19741, 1:1,000, Wako) antibodies with blocking solution. The brain sections were then followed by incubation with biotin-tagged anti-rabbit second antibody. After incubation with ABC solution (cat. no. PK-6101, Vector Laboratories), brain sections were developed using a DAB peroxidase substrate kit (cat. no. SK-4100, Vector Laboratories). The densities of astrocytes and total number of microglia were measured in the substantia nigra region by ImageJ

software (<http://rsb.info.nih.gov/ij/>, NIH). For histopathology of major organs such as the liver, kidney and spleen, 8- to 10-week-old male C57BL/6 mice were i.p. injected with 50 µg of GQDs on a biweekly basis for 6 months. After the 6 months of injections, mice were perfused with 4% PFA containing PBS. The liver, kidney and spleen were then stained with an H&E staining kit (cat. no. H-3502, Vector Laboratories).

**Behaviour analyses.** The cylinder test<sup>28</sup> was devised to identify any asymmetry in forelimb use. Every contact made by a forepaw in a 20-cm-wide clear glass cylinder was scored by a blinded observer using video clips. No habituation of the mice to the testing cylinder was allowed before making the video clips. A total of 20 to 30 wall touches were counted per animal (only contacts with fully extended forelimbs). The degree of impaired forelimb touches was converted to percentage based on the total forelimb use. The control group scored approximately 50% in this test. The mice were completely isolated from the test cylinder before actual testing.

For the pole test<sup>29</sup>, test mice were allowed to adapt to the behavioural room for 30 min before testing. A 75 cm metal pole with a diameter of 9 mm was prepared with bandage gauze wrapping. To initiate the test, each mouse was placed 7.5 cm from the top facing upwards. The scores were based on the total time taken to reach the bottom. The test animals were trained for two successive days before the actual trial, where each practice provided three different trials. No more than 60 s was allowed for each animal. The results for the turn down, climb down and the total time (in seconds) were recorded.

Clasping test<sup>31</sup>: For behaviour test of hA53T  $\alpha$ -syn mice, the hindlimb clasping function was tested. After clearing all surrounding objects, the test

animals were lifted by grasping their tails near the base and their hindlimb positions were observed for 10 secs. The clasping functional scores are rated on the following criteria: 1) Score 0: hindlimbs are spread outwards and away from the abdomen. 2) Score 1: For more than 5 secs, single hindlimb is drawn back towards the abdomen. 3) Score 2: For more than 5 secs, both hindlimbs are partially drawn back towards the abdomen. 4) Score 3: For more than 5 secs, both hindlimbs are completely drawn back towards the abdomen.

**Preparation of nano-GOs and rGQDs.** To prepared nano-GOs, pristine GOs were synthesized by improved Hummer's method according a previous literature<sup>32</sup>. Obtained GOs powder was subsequently tip-sonicated in DI water (10 mg/ml) for 3 hours to yield nano-GOs. The reduction of GQDs was achieved by the autoclave-based hydrothermal method at 200 °C for 2 hours.

**The viability assay of human neuroblastoma cell line.** SH-SY5Y (ATCC® CRL-2266™) was purchased from ATCC and authenticated by STR analysis. Cells were routinely tested for mycoplasma contamination and found to be negative. SH SY5Y cells were plated at a density 50,000 cells/well in 48-well plate and incubated in 5% CO<sub>2</sub> incubator at 37 °C. The viability of SH-SY5Y cells was quantified by alamarBlue cell viability assay kit (Cat#: DAL1025; Molecular Probes™), following the manufacturer's instructions.

**Statistics.** Mean  $\pm$  s.d. values were determined from more than three independent experiments. To determine the statistical significance, P values were determined by Student's t-test or ANOVA with Bonferroni correction. Prism6 software was used for statistics analysis.

## 1.5. Supplementary Information

Figures	Sample	0h		2h		4h		6h		8h	
		Mean $\pm$ s.d.	P value	Mean $\pm$ s.d.	P value	Mean $\pm$ s.d.	P value	Mean $\pm$ s.d.	P value	Mean $\pm$ s.d.	P value
Figure 1b	$\alpha$ -syn	5.63 $\pm$ 5.25	$P > 0.9999$	7.83 $\pm$ 5.65	$P > 0.9999$	6.45 $\pm$ 3.31	$P = 0.0003$	7.43 $\pm$ 5.18	$P < 0.0001$	8.13 $\pm$ 2.10	$P < 0.0001$
	$\alpha$ -syn+GQDs	8.75 $\pm$ 5.68		16.63 $\pm$ 4.67		30.48 $\pm$ 11.70		46.10 $\pm$ 13.67		70.40 $\pm$ 12.83	
Figure 1c	$\alpha$ -syn	9.08 $\pm$ 10.69	$P > 0.9999$	9.43 $\pm$ 7.20	$P > 0.9999$	9.65 $\pm$ 5.21	$P = 0.0143$	9.63 $\pm$ 3.64	$P < 0.0001$	8.05 $\pm$ 3.79	$P < 0.0001$
	$\alpha$ -syn+GQDs	6.89 $\pm$ 5.26		20.02 $\pm$ 5.13		34.82 $\pm$ 5.13		50.40 $\pm$ 14.50		69.29 $\pm$ 10.12	

Figures	Sample	10h		12h		24h		72h		168h	
		Mean $\pm$ s.d.	P value	Mean $\pm$ s.d.	P value	Mean $\pm$ s.d.	P value	Mean $\pm$ s.d.	P value	Mean $\pm$ s.d.	P value
Figure 1b	$\alpha$ -syn	6.40 $\pm$ 4.08	$P < 0.0001$	10.18 $\pm$ 5.23	$P < 0.0001$	7.43 $\pm$ 3.71	$P < 0.0001$	10.80 $\pm$ 2.29	$P < 0.0001$	9.23 $\pm$ 5.48	$P < 0.0001$
	$\alpha$ -syn+GQDs	86.88 $\pm$ 5.95		90.45 $\pm$ 4.28		89.80 $\pm$ 5.95		95.63 $\pm$ 8.30		100.00 $\pm$ 15.77	
Figure 1c	$\alpha$ -syn	7.58 $\pm$ 3.97	$P < 0.0001$	9.45 $\pm$ 3.55	$P < 0.0001$	8.33 $\pm$ 9.26	$P < 0.0001$	13.38 $\pm$ 7.02	$P < 0.0001$	13.40 $\pm$ 13.89	$P < 0.0001$
	$\alpha$ -syn+GQDs	80.27 $\pm$ 6.11		83.78 $\pm$ 11.65		89.01 $\pm$ 6.72		93.40 $\pm$ 13.80		100.00 $\pm$ 26.97	

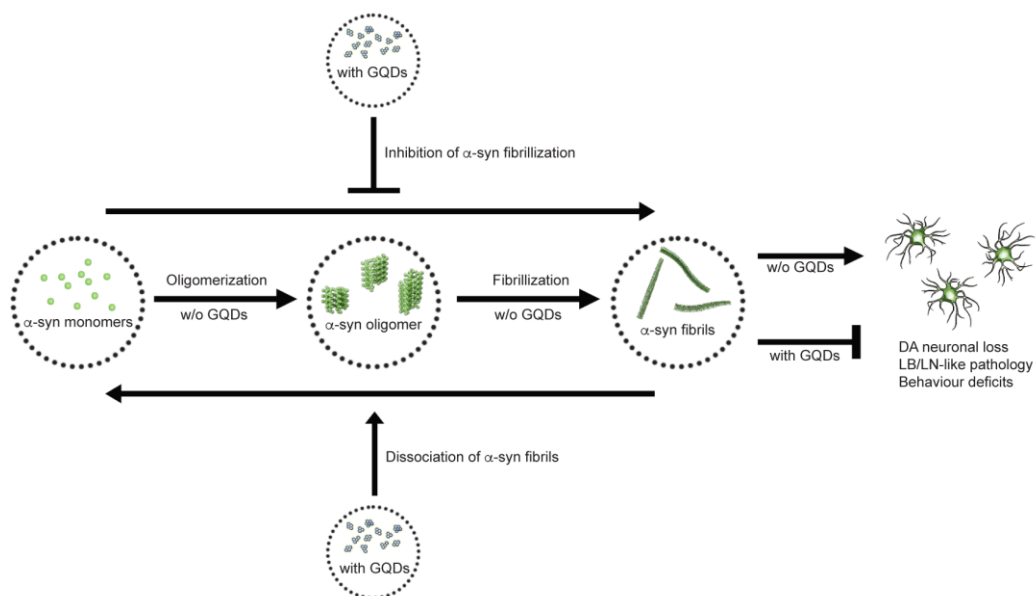
Figures	Sample	0h		1h		3h		6h	
		Mean $\pm$ s.d.	P value	Mean $\pm$ s.d.	P value	Mean $\pm$ s.d.	P value	Mean $\pm$ s.d.	P value
Figure 1e	$\alpha$ -syn fibrils	100.00 $\pm$ 1.88	$P > 0.9999$	94.98 $\pm$ 3.51	$P < 0.0001$	95.53 $\pm$ 3.21	$P < 0.0001$	90.05 $\pm$ 4.88	$P < 0.0001$
	$\alpha$ -syn fibrils+GQDs	99.98 $\pm$ 1.88		61.58 $\pm$ 13.21		54.38 $\pm$ 10.05		39.43 $\pm$ 16.53	
Figure 1f	$\alpha$ -syn fibrils	100.00 $\pm$ 22.7	$P > 0.9999$	91.48 $\pm$ 5.53	$P < 0.0001$	92.73 $\pm$ 3.48	$P < 0.0001$	89.45 $\pm$ 4.60	$P < 0.0001$
	$\alpha$ -syn fibrils+GQDs	98.43 $\pm$ 3.84		49.70 $\pm$ 11.09		41.13 $\pm$ 10.17		33.58 $\pm$ 14.54	

Figures	Sample	12h		24h		72h		168h	
		Mean $\pm$ s.d.	P value	Mean $\pm$ s.d.	P value	Mean $\pm$ s.d.	P value	Mean $\pm$ s.d.	P value
Figure 1e	$\alpha$ -syn fibrils	88.83 $\pm$ 3.78	$P < 0.0001$	90.40 $\pm$ 2.45	$P < 0.0001$	92.18 $\pm$ 6.15	$P < 0.0001$	82.18 $\pm$ 11.91	$P < 0.0001$
	$\alpha$ -syn fibrils+GQDs	34.00 $\pm$ 10.34		21.03 $\pm$ 8.85		22.55 $\pm$ 7.70		13.45 $\pm$ 5.96	
Figure 1f	$\alpha$ -syn fibrils	86.95 $\pm$ 4.39	$P < 0.0001$	85.68 $\pm$ 8.86	$P < 0.0001$	85.32 $\pm$ 3.18	$P < 0.0001$	84.58 $\pm$ 10.53	$P < 0.0001$
	$\alpha$ -syn fibrils+GQDs	26.48 $\pm$ 8.09		25.08 $\pm$ 7.02		22.50 $\pm$ 6.50		13.55 $\pm$ 6.13	

**Figure 3-ST1.** Mean  $\pm$  s.d. values and P values of Figure 1b, c, e, and f.





**Figure 3-S1.** Schematic overview of the therapeutic effect of GQDs on the pathogenesis of PD. Without GQDs, pathological  $\alpha$ -syn monomers undergo spontaneous fibrillization to form fibrillary aggregates, which ultimately induces loss of dopaminergic neurons, LB/LN like pathology and behavior deficits. On the other hand, GQDs treatment inhibits  $\alpha$ -syn fibrillization and disaggregates mature fibrils to monomers and thereby prevents dopaminergic neuron loss, LB/LN-like pathology and behavior deficits provoked by abnormal  $\alpha$ -syn fibrillization.

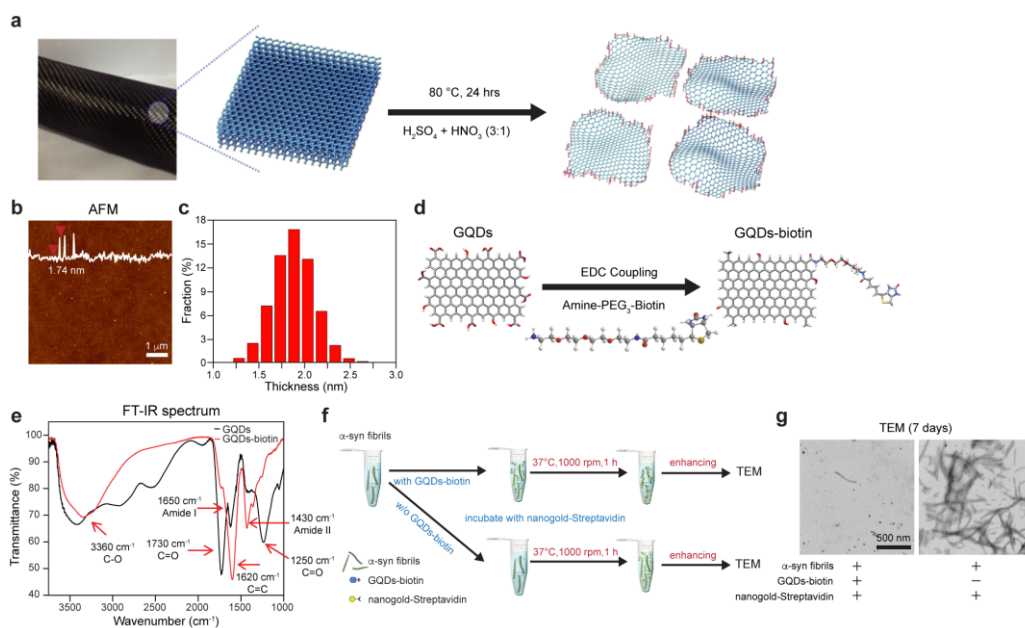


**Figure 3-S2.** Synthesis and biotinylation of QDs and binding assay between QDs-biotin and  $\alpha$ -syn fibrils. a, Schematic representation of synthetic procedure from carbon fibre. b, AFM image of synthesised QDs. c, Fractions of QDs with different thicknesses. d, Schematic representation of synthetic procedure of biotinylation on QDs. e, FT-IR spectrum of QDs (black line) and biotinylated QDs (red line) with designated peaks and shifts for the functional groups. f, Schematic representation of the preparation steps for the binding assay between biotinylated QDs and nanogold-streptavidin tagged  $\alpha$ -syn fibrils. g, TEM images of preformed  $\alpha$ -syn fibrils after 7 days in the presence of QDs-biotin-nanogold-streptavidin complex (left) and nanogold-streptavidin only (right).

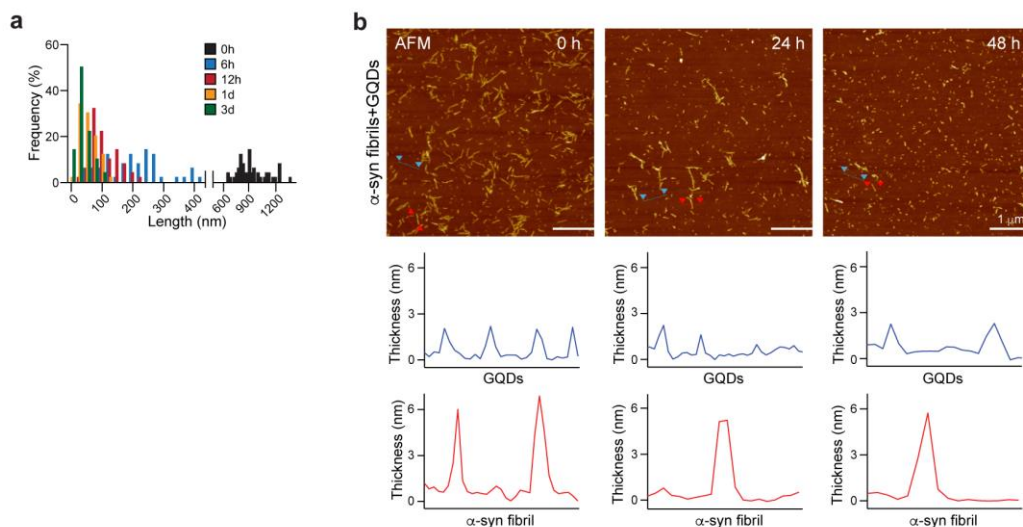


**Figure 3-S3.** The effect of GQDs on disaggregation of  $\alpha$ -syn fibrils. a, The distribution of  $\alpha$ -syn fibril lengths at various time points (0, 6, 12, 24, and 72 hours,  $n=50$  fibrils at each time point). b, AFM images of  $\alpha$ -syn fibrils with GQDs after various time points (0, 24, and 48 hours) and the representative line profiles of the designated regions, marked by blue (GQDs) and red ( $\alpha$ -syn fibrils) arrows at each time point.

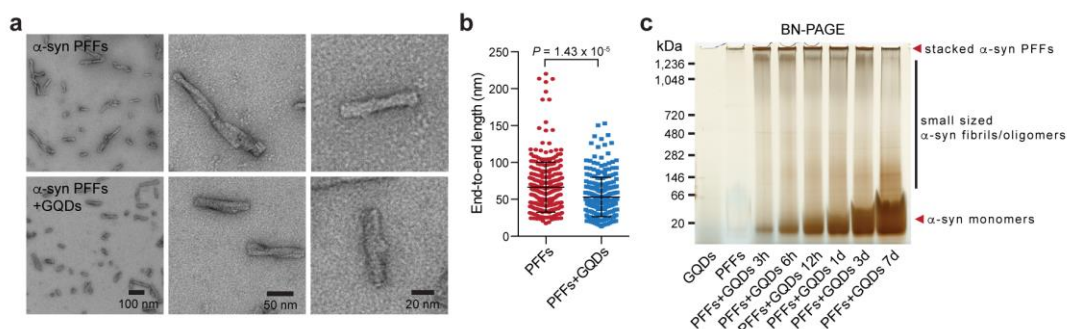


**Figure 3-S4.** The effect of GQDs on disaggregation of  $\alpha$ -syn PFFs. a, Representative TEM images of fibrillized  $\alpha$ -syn PFFs (5 mg/ml) incubated in the absence of (top) and in the presence of (bottom) GQDs (5 mg/ml) for 1 hour. b, The end-to-end length of  $\alpha$ -syn PFFs after 1 hour of incubation. Mean  $\pm$  s.d. values are  $66.52 \pm 34.53$  and  $54.49 \pm 26.74$  for PFFs and PFFs+GQDs ( $n=286$ : PFFs,  $n=249$ : PFFs + GQDs; two-tailed Student's t-test). c, The amount of remaining  $\alpha$ -syn PFFs and disaggregated  $\alpha$ -syn PFFs assessed by BN-PAGE after various incubation periods. These experiments were independently repeated three times with similar results.

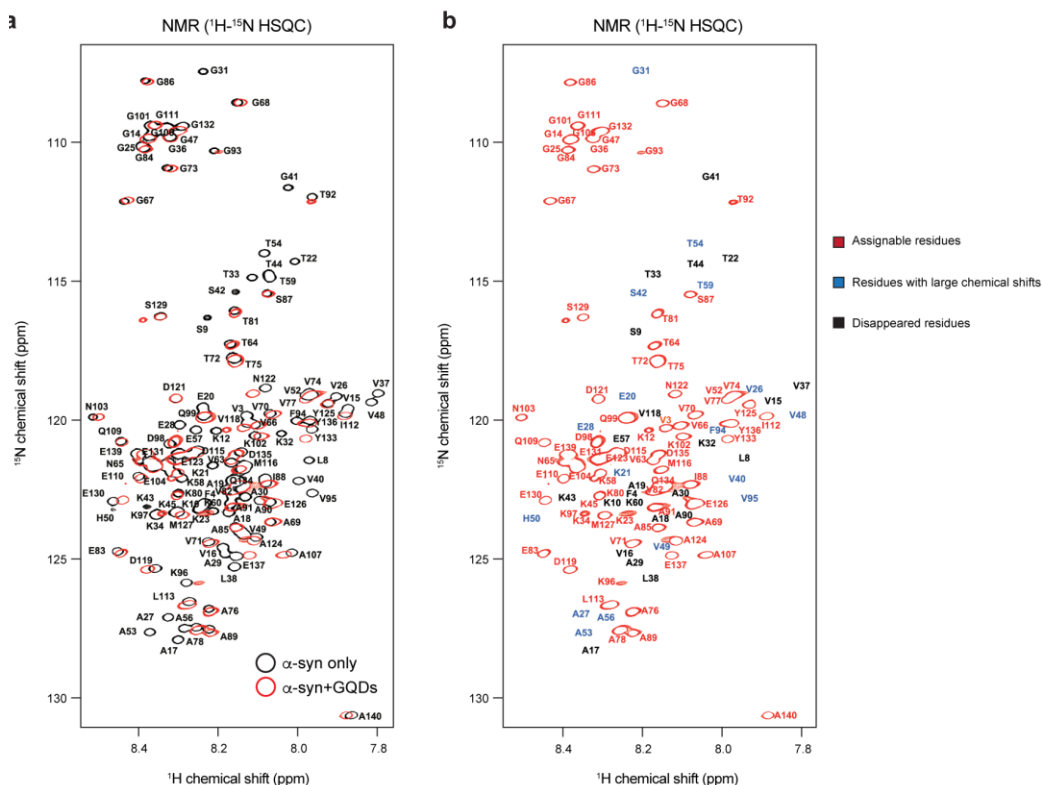


**Figure 3-S5.**  $^1\text{H}$ - $^{15}\text{N}$  HSQC spectral analysis. a, Full, overlapped  $^1\text{H}$ - $^{15}\text{N}$  HSQC spectra of  $^{15}\text{N}$ -labelled  $\alpha$ -syn monomers only (black) and after incubation with GQDs (red). The assigned residues designate  $^{15}\text{N}$ -labelled  $\alpha$ -syn monomers only group. b, A full HSQC spectrum of  $^{15}\text{N}$ -labelled  $\alpha$ -syn monomers incubated with GQDs. Based on the peak intensity of  $^{15}\text{N}$ -labelled  $\alpha$ -syn monomers only group, the residues with no or minimal decrease in peak intensity (red), the residues with significant decrease in peak intensity (blue), and the disappeared residues (black) are distinctively assigned.

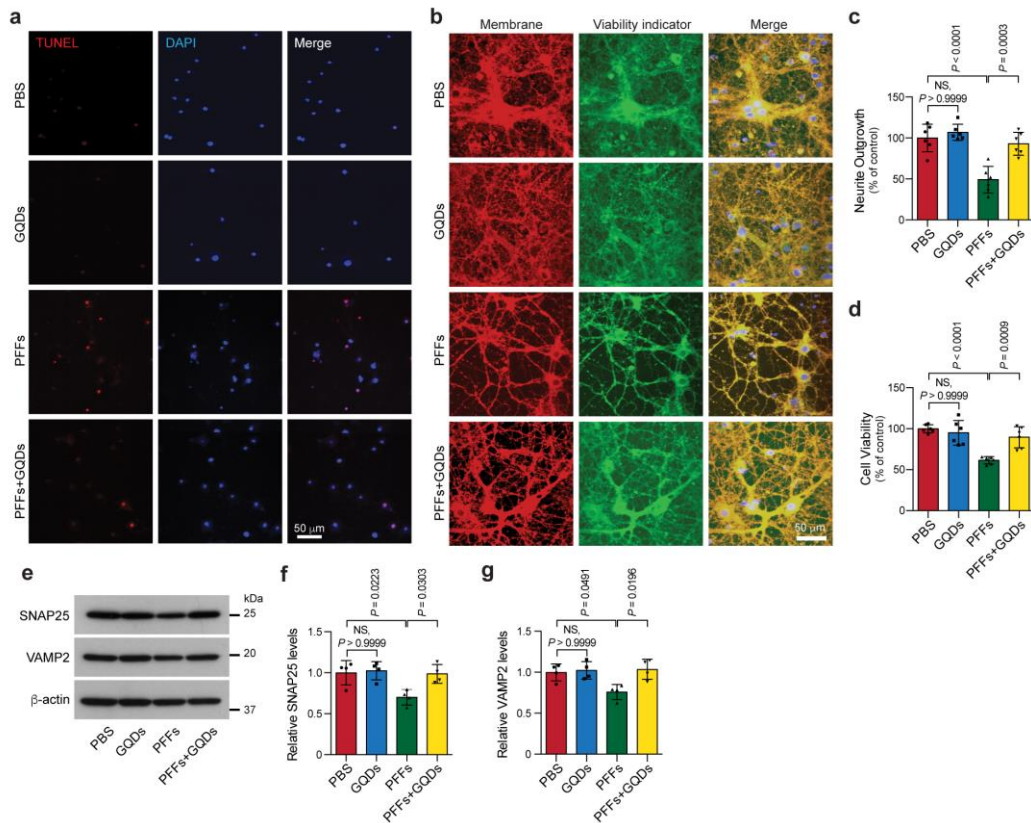


**Figure 3-S6.** The effect of GQDs on  $\alpha$ -syn PFFs-induced cell death and restricted neurite outgrowth. a, Representative TUNEL-positive neurons. DIV 10 primary cortical neurons were treated with  $\alpha$ -syn PFFs (1  $\mu$ g/ml) in the absence and presence of GQDs (1  $\mu$ g/ml). TUNEL assay was performed after 7 days of incubation. b, Representative micrographs of neurite outgrowth and cell viability assays stained by outer cell membrane (red) and cell-permeable viability indicator (green). c-d, Quantifications of neurite outgrowth and neuron viability from the stained images. Mean values of the neurite outgrowth are 100.00, 106.89, 49.08, and 92.98 for PBS, GQDs, PFFs, and PFFs+GQDs; mean values of the cell viability are 100.00, 95.08, 61.43, and 89.68 for PBS, GQDs, PFFs, and PFFs+GQDs (n=6, biologically independent samples; two-way ANOVA with a post hoc Bonferroni test; NS, not significant; error bars are the standard deviation). e, Representative immunoblot analysis of SNAP25 and VAMP2 protein levels. 10 DIV primary cortical neurons were treated with  $\alpha$ -syn PFFs (5  $\mu$ g/ml) in the absence and presence of GQDs (5  $\mu$ g/ml) and incubated for 7 days. f, The expression levels of SNAP25 were normalised to  $\beta$ -actin level and quantified. Mean values are 100.00, 102.6, 69.98, and 98.68 for PBS, GQDs, PFFs, and PFFs+GQDs (n=4, biologically independent sample; two-way ANOVA with a post hoc Bonferroni test; NS, not significant; error bars are the standard deviation). g, VAMP2 were normalised to  $\beta$ -actin level and quantified. Mean values are 100.00, 102.33, 75.80, and 103.55 for PBS, GQDs, PFFs, and PFFs+GQDs (n=4, biologically independent samples; two-way ANOVA with a post hoc Bonferroni test; NS, not significant; error bars are the standard deviation).

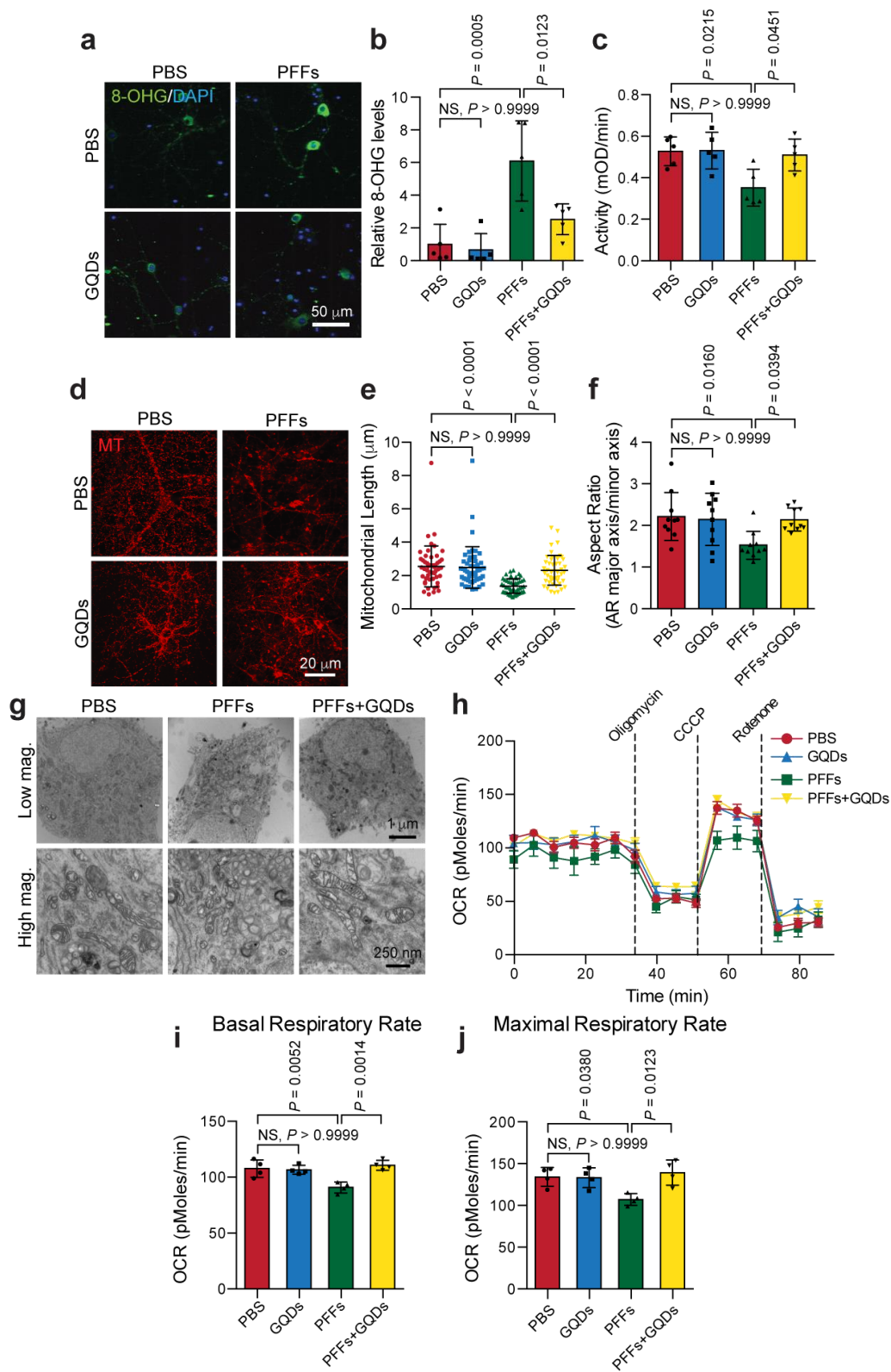


**Figure 3-S7.** The effect of GQDs on  $\alpha$ -syn PFFs-induced mitochondrial dysfunction and oxidative stress. a, Representative 8-OHG immunostaining images in primary cortical neurons treated with  $\alpha$ -syn PFFs (1  $\mu$ g/ml) in the absence and presence of GQDs (1  $\mu$ g/ml) and incubated for 7 days. b, Quantifications of 8-OHG content by the immunofluorescence levels. Mean values are 1.00, 0.66, 6.01, and 2.54 for PBS, GQDs, PFFs, and PFFs+GQDs (n=5, biologically independent samples; two-way ANOVA with a post hoc Bonferroni test; NS, not significant; error bars are the standard deviation). c, Measurements of the mitochondrial complex I activity after 7 days of  $\alpha$ -syn PFFs (1  $\mu$ g/ml) incubation. Mean values are 0.52, 0.53, 0.35, and 0.51 for PBS, GQDs, PFFs, and PFFs+GQDs (n=5, biologically independent samples; two-way ANOVA with a post hoc Bonferroni test; NS, not significant; error bars are the standard deviation). d, Representative MitoTracker positive micrographs. 10 DIV primary cortical neurons were treated with  $\alpha$ -syn PFFs (1  $\mu$ g/ml) in the absence and presence of GQDs (1  $\mu$ g/ml). After 7 days of incubation, mitochondria were labelled with MitoTracker® Orange CMTMRos (Red). e, Quantifications of the length of the stained mitochondria. Mean values are 2.55, 2.49, 1.38, and 2.33 for PBS, GQDs, PFFs, and PFFs+GQDs (n=50, biologically independent samples; two-way ANOVA with a post hoc Bonferroni test; NS, not significant; error bars are the standard deviation). f, Aspect ratio of the stained mitochondria. Mean values are 2.22, 2.15, 1.53, and 2.14 for PBS, GQDs, PFFs, and PFFs+GQDs (n=10, biologically independent samples; two-way ANOVA with a post hoc Bonferroni test; NS, not significant; error bars are the standard deviation). g, Representative TEM images with low and high magnifications after the same preparation steps. h, Microplate-based respirometry readings for neurons. The oxygen consumption rate was measured in an XF 24 Seahorse analyser in primary cortical neurons treated with  $\alpha$ -syn PFFs (1  $\mu$ g/ml) in the absence and presence of GQDs (1  $\mu$ g/ml) for 24 hours. Mean values are 111.84, 116.36, 103.08, 107.07, 105.15, 111.79, 94.42, 54.67, 55.42, 50.81, 139.74, 137.09, 127.98, 28.09, 32.08, and 32.68 for PBS group; 106.87, 107.41, 105.22, 108.21, 113.83, 107.85, 100.25, 61.22, 58.81, 60.01, 140.25, 131.73, 128.53, 37.23, 47.80, and 37.92 for GQDs group; 91.65, 104.99, 93.36, 90.06, 94.11, 100.81, 86.56, 47.58, 56.70, 53.91, 109.52, 112.07, 108.72, 23.60, 27.08, and 35.31 for PFFs group; 104.20, 115.69, 109.04, 115.20, 113.70, 111.38, 106.44, 66.55, 66.09, 65.96, 147.19, 135.62, 129.37, 37.86, 40.70, and 46.95 for PFFs+GQDs (n=4, biologically independent experiments). i, Quantifications of the basal respiratory rate. Mean values are 107.84, 106.68, 90.91, and 110.78 for PBS, GQDs, PFFs, and PFFs+GQDs (n=4, biologically independent experiments; two-way ANOVA with a post hoc Bonferroni test; NS, not significant; error bars are the standard deviation). j, Quantifications of the maximal respiratory rates from the respirometry results. Mean values are 134.32, 133.26, 107.14, and 139.37 for PBS, GQDs, PFFs, and PFFs+GQDs (n=4, biologically independent experiments; two-way ANOVA with a post hoc Bonferroni test; NS, not significant; error bars are the standard deviation).



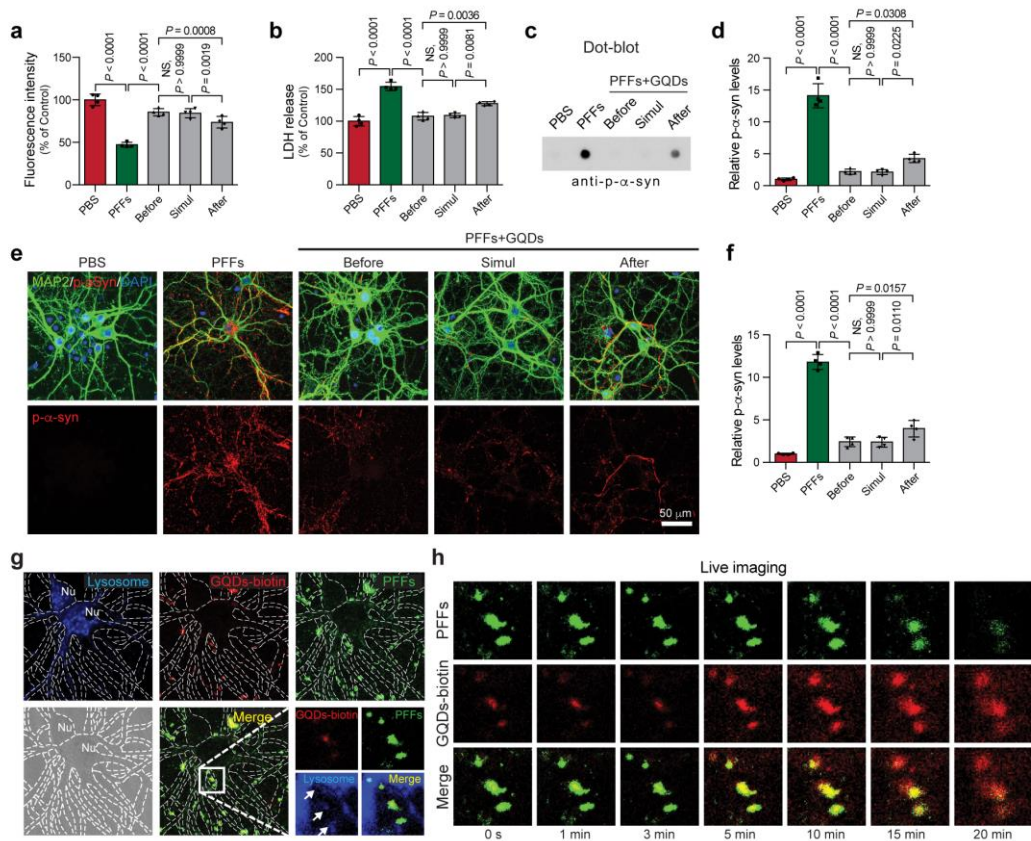


**Figure 3-S8.** The effect of GQDs on  $\alpha$ -syn PFFs-induced primary neuronal toxicity and pathology at different treatment points of GQDs and live cell imaging. **a**, Neuronal toxicities assessed by alamarBlue and **b**, LDH assays. 10 DIV mouse cortical neurons were treated with  $\alpha$ -syn PFFs (1  $\mu$ g/ml) with 3 days pre- (n=4, Before), simultaneous (n=4, Simul), and 3 days post-incubation (n=4, After) of GQDs (1  $\mu$ g/ml) for 7 days. Mean values are 100.00, 47.14, 85.27, 84.52, and 73.72 for PBS, PFFs, Before, Simul, and After of alamarBlue assay; 100.00, 154.64, 107.72, 109.11, and 127.62 for PBS, PFFs, Before, Simul, and After of LDH assay (n=4, biologically independent samples; two-way ANOVA with a post hoc Bonferroni test; NS, not significant; error bars are the standard deviation). **c**, Representative images of p- $\alpha$ -syn by dot-blot analysis and **d**, quantified intensities normalised to the PBS control. Mean values are 1.00, 14.11, 2.21, 2.14, and 4.26 for PBS, PFFs, Before, Simul, and After (n=4, biologically independent samples; two-way ANOVA with a post hoc Bonferroni test; NS, not significant; error bars are the standard deviation). **e**, Representative p- $\alpha$ -syn immunostaining micrographs with p- $\alpha$ -syn antibody at 7 days post-incubation. **f**, Quantifications of p- $\alpha$ -syn immunofluorescence intensities normalised to the PBS control. Mean values are 1.00, 11.82, 2.44, 2.39, and 3.98 for PBS, PFFs, Before, Simul, and After (n=4, biologically independent samples; two-way ANOVA with a post



hoc Bonferroni test; NS, not significant; error bars are the standard deviation). g, Representative images show that GQDs and  $\alpha$ -syn PFFs are co-localised in the lysosome of primary cultured neuron with live imaging. The LysoTracker (blue), GQDs-biotin-streptavidin Qdot complex (red), and FITC-labelled  $\alpha$ -syn PFFs (green) were used. h,  $\alpha$ -syn PFFs disaggregation process by GQDs was monitored by time-lapse fluorescence signals during live imaging. Experiment was independently repeated three times with duplication with similar results.

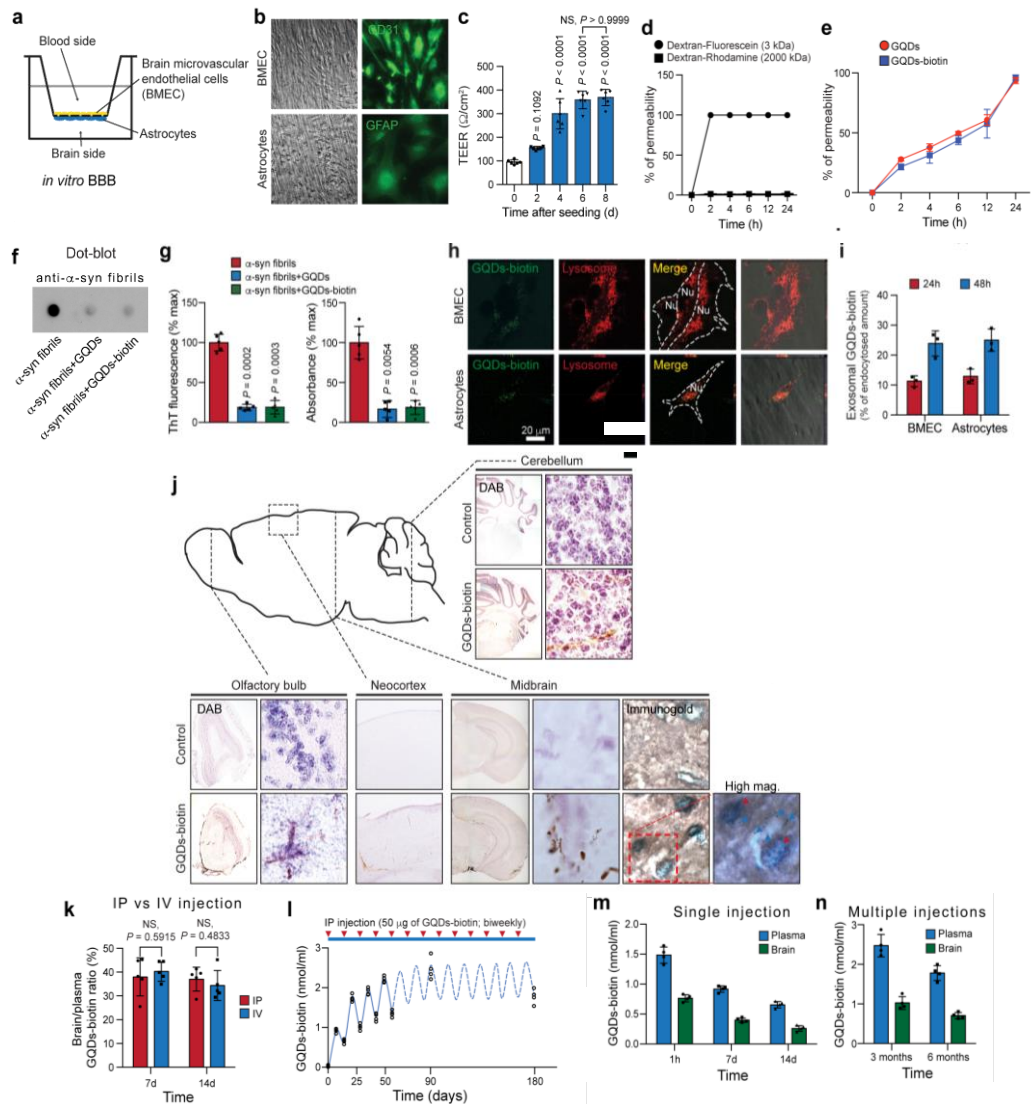


**Figure 3-S9.** The BBB permeability of GQDs. **a**, Schematic illustration of the *in vitro* BBB model. **b**, The confluent monolayer formations of the brain microvascular endothelial cells (BMEC) and astrocytes were determined by immunofluorescence staining with CD31 (endothelial cell marker) or GFAP (astrocyte marker) antibodies, respectively. **c**, The transepithelial electrical resistance (TEER) was measured at various time points. Mean values are 95.95, 154.67, 299.98, 358.35, and 368.88 at 0, 2, 4, 6, and 8 d (n=6, biologically independent samples; one-way ANOVA with a post hoc Bonferroni test, NS, not significant; error bars are the standard deviation). **d**, The permeabilities of endothelial cell monolayer and astrocyte were monitored by measuring the ratio between the blood side and the brain side using dextran-fluorescein (3 kDa) and dextran-rhodamine (2,000 kDa) (n=4, biologically independent samples). **e**, Quantifications of permeability of GQDs and GQDs-

biotin over time. Mean  $\pm$  s.d. values are  $27.86 \pm 1.29$ ,  $37.71 \pm 3.07$ ,  $49.65 \pm 1.52$ ,  $60.78 \pm 4.28$ , and  $93.652.55$  at 2, 4, 6, 12, and 24 hours of GQDs;  $21.65 \pm 2.46$ ,  $31.29 \pm 6.65$ ,  $43.85 \pm 3.69$ ,  $57.60 \pm 11.93$ , and  $96.14 \pm 2.27$  at 2, 4, 6, 12, and 24 hours of GQDs-biotin (n=4, biologically independent samples). f, The  $\alpha$ -syn fibril disaggregation abilities of pristine GQDs and GQDs-biotin monitored by dot-blot (n=3, biologically independent samples), g, ThT, and turbidity assays. Mean  $\pm$  s.d. values are  $100.00 \pm 9.35$ ,  $19.04 \pm 4.14$ , and  $19.81 \pm 8.33$  of  $\alpha$ -syn fibril,  $\alpha$ -syn fibril+GQDs, and  $\alpha$ -syn fibril+GQDs-biotin for ThT assay;  $100.00 \pm 20.35$ ,  $18.26 \pm 7.60$ , and  $18.79 \pm 8.64$  of  $\alpha$ -syn fibril,  $\alpha$ -syn fibril+GQDs, and  $\alpha$ -syn fibril+GQDs-biotin for turbidity assay (n=5, biologically independent samples; one-way ANOVA with a post hoc Bonferroni test). h, Confocal laser scanning microscope images of primary cultured BMEC and astrocyte after 1 hour incubation with GQDs-biotin. GQDs-biotin are shown with Qdot™ streptavidin, whereas the lysosomes labelled by LysoTracker orange. i, Quantifications of the exosomal GQDs-biotin from BMEC or astrocytes. The amount of GQDs-biotin was measured from the isolated exosome at 24 and 48 hours after endocytosis. Mean  $\pm$  s.d. values are  $11.30 \pm 1.80$  and  $23.91 \pm 4.22$  for 24 h and 48 h of BMEC;  $12.91 \pm 2.46$  and  $25.04 \pm 3.77$  for 24 h and 48 h of astrocytes (n=3, biologically independent samples). j, Immunohistochemical analysis of i.p. injected GQDs-biotin (2 mg/kg) by staining the olfactory bulb, neocortex, midbrain, and cerebellum with avidin-biotin complex method or immunogold method at 7 days after injection. The DAB positive stained signals were detected in GQDs-biotin-injected mice compared to vehicle-injected control group. Immunogold positive signals were observed inside (red triangles) or outside of neurons (blue triangles). k, The comparison between intraperitoneal (IP; red bar) and intravenous (IV; blue bar) injections of GQDs-biotin. Mean  $\pm$  s.d. values are  $38.02 \pm 7.97$  and  $40.26 \pm 4.10$  for IP and IV at 7 d;  $37.06 \pm 5.02$  and  $34.42 \pm 6.27$  for IP and IV at 14 d (n=5, biologically independent animals; two-tailed Student's t-test; NS, not significant). l, The GQDs-biotin concentrations of the plasma were measured from the non-injected control after 1 week, 2 weeks, 3 weeks, 4 weeks, 5 weeks, 6 weeks, 7 weeks, 8 weeks, 3 months, and 6 months (n=4, each group) after biweekly GQDs-biotin injections using biotin quantification kit. m, The brain (green bar) and plasma (blue bar) concentrations were measured from 1 hour, 7 days, and 14 days after single i.p. injection (2 mg/kg of GQDs-biotin. Mean values are 1.46 and 0.77 for plasma and brain of 1 hour; 0.92 and 0.40 for plasma and brain of 7 days; 0.66 and 0.26 for plasma and brain of 14 days. (n=4, biologically independent animals; error bars are the standard deviation). n, 3 months and 6 months after multiple biweekly injections. NS, not significant; Student's ttest, error bars are the standard deviation. Mean values are 2.47 and 1.03 for plasma and brain of 3 months; 1.78 and 0.71 for plasma and brain of 7 months (n=4, biologically independent animals; error bars are the standard deviation).

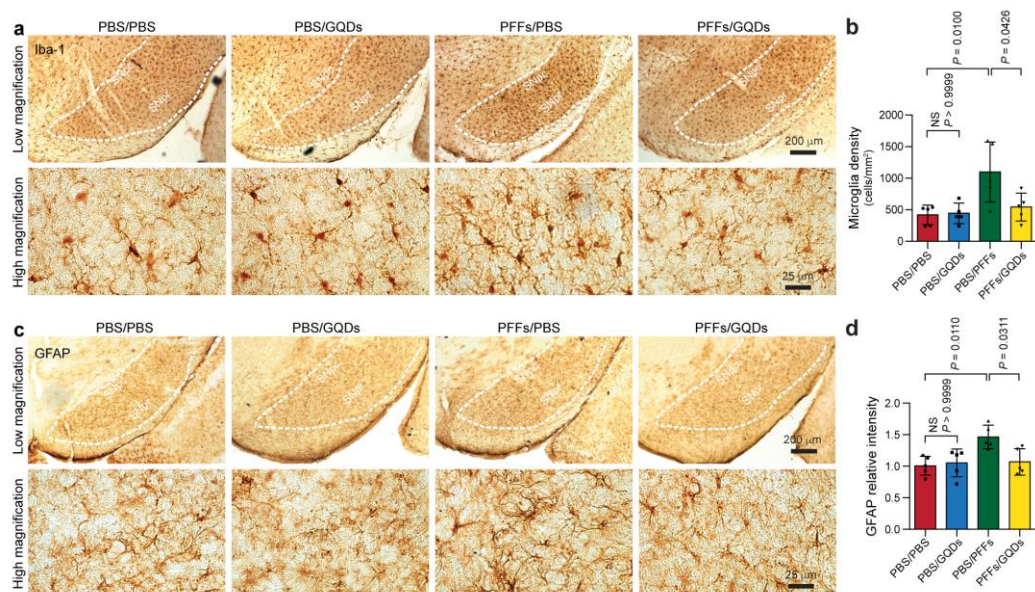


**Figure 3-S10.** The effect of GQDs on  $\alpha$ -syn PFFs-induced glial cell activation in the SN. a, Representative immunohistochemistry images for Iba-1 in the SN with low and high magnifications. Microglia in the SN of  $\alpha$ -syn PFFs-injected hemisphere were stained with specific microglial marker Iba-1 (ionised calcium binding protein; specific marker of microglia/macrophage). b, Quantifications of Iba-1-positive microglia. Mean values are 420.42, 445.54, 1099.80, and 544.20 for PBS/PBS, PBS/GQDs, PFFs/PBS, and PFFs/GQDs (n=5, biologically independent animals; two-way ANOVA with a post hoc Bonferroni test, error bars are the standard deviation). c, Representative immunohistochemistry images for GFAP in the SN with low and high magnifications. Astrocytes in the SN of  $\alpha$ -syn PFFs-injected hemisphere were stained with GFAP (glial fibrillary acidic protein; specific marker of astrocytes) antibody. d, Quantifications of GFAP intensity. The relative GFAP intensities were normalised against the PBS-injected control group. Mean values are 1.00, 1.05, 1.46, and 1.07 for PBS/PBS, PBS/GQDs, PFFs/PBS, and PFFs/GQDs (n=5, biologically independent animals; two-way ANOVA with a post hoc Bonferroni test, error bars are the standard deviation).

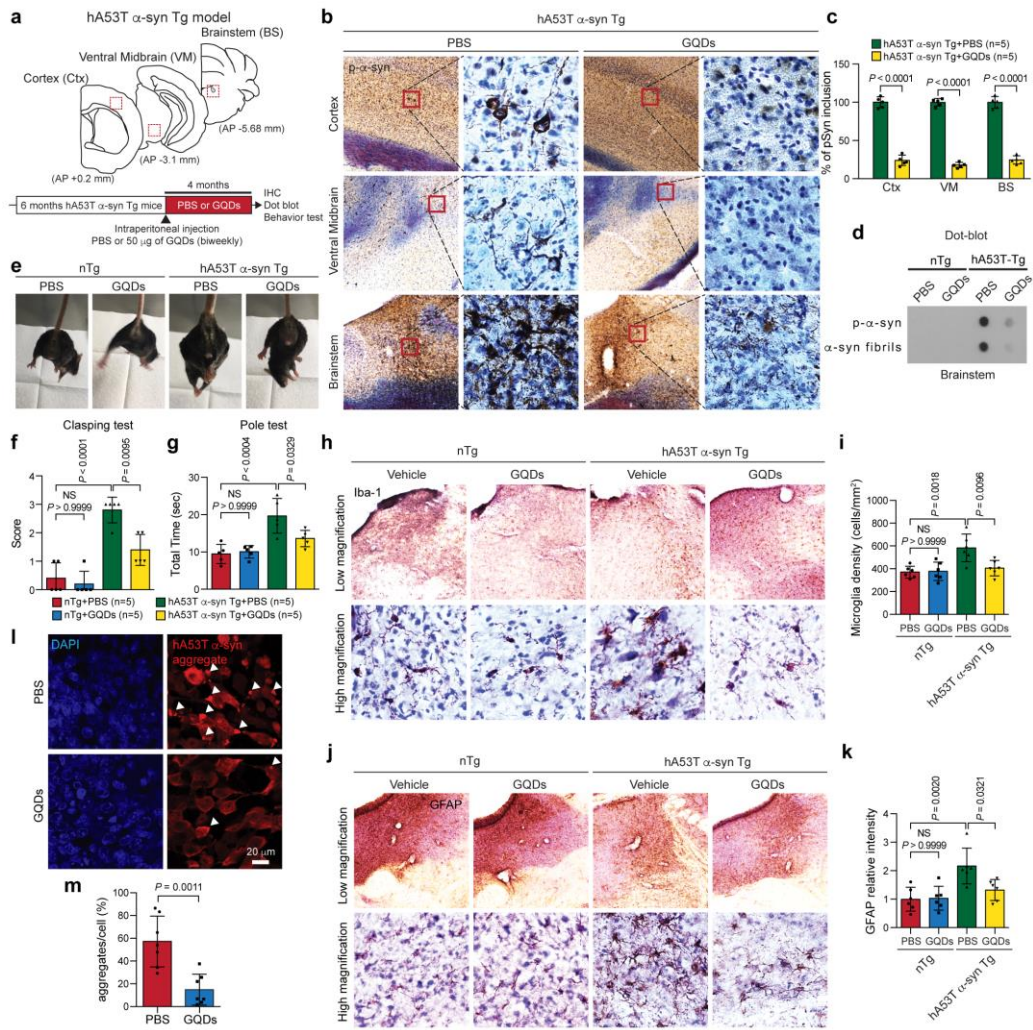


**Figure 3-S11.** The effect of GQDs on pathologies and glial cell activation of hA53T  $\alpha$ -syn transgenic mice. **a**, Schematic illustration of the observing areas of hA53T  $\alpha$ -syn Tg model. As a treatment, 50  $\mu$ g of GQDs or PBS were i.p. injected biweekly for 4 months. **b**, Representative p- $\alpha$ -syn immunostaining images in the cortex, ventral midbrain, and brainstem of hA53T  $\alpha$ -syn Tg. **c**, Quantifications of p- $\alpha$ -syn immunoreactive neurons in the cortex (Ctx), ventral midbrain (VM), and brainstem (BS). Mean values are 100.00 and 23.80 for PBS and GQDs of Ctx; 100.00 and 17.80 for PBS and GQDs of VM; 100.00 and 24.60 for PBS and GQDs of BS (n=5, biologically independent animals; two-tailed Student's t-test; error bars are the standard deviation). **d**, Representative dot-blot assay of p- $\alpha$ -syn and  $\alpha$ -syn fibrils. Experiment was independently repeated three times with similar results. **e**, Hindlimb clasping dystonic phenotypes of hA53T  $\alpha$ -syn Tg mice were compared with GQDs-injected group. **f**, Assessment of the behavioural deficits measured by the clasping scores. Mean values are 0.4, 0.2, 2.8, and 1.4 for nTg+PBS, nTg+GQDs, hA53T



$\alpha$ -syn Tg+PBS, and hA53T  $\alpha$ -syn Tg+GQDs (n=5, biologically independent animals; two-way ANOVA with a post hoc Bonferroni test, NS, not significant; error bars are the standard deviation). g, Assessment of the behavioural deficits measured by the pole tests. Mean values are 9.49, 10.05, 19.69, and 13.60 for nTg+PBS, nTg+GQDs, hA53T  $\alpha$ -syn Tg+PBS, and hA53T  $\alpha$ -syn Tg+GQDs (n=5, biologically independent animals; two-way ANOVA with a post hoc Bonferroni test, NS, not significant; error bars are the standard deviation). h, Representative immunohistochemistry images of microglia in the LC of the brainstem with low and high magnifications. Microglia in the brainstem of nTg or hA53T  $\alpha$ -syn Tg were stained with Iba-1. i, Quantifications of Iba-1-positive microglia. Mean values are 371.17, 378.83, 583.67, and 405.67 for nTg/PBS, nTg/GQDs, hA53T  $\alpha$ -syn Tg/PBS, and hA53T  $\alpha$ -syn Tg/GQDs (n=6, biologically independent animals; two-way ANOVA with a post hoc Bonferroni test, NS, not significant; error bars are the standard deviation). j, Representative immunohistochemistry images of GFAP in the brainstem with low and high magnifications. k, Quantifications of GFAP intensity. The relative GFAP intensities were normalized against the PBS-injected control group. Mean values are 1.00, 1.03, 2.17, and 1.32 for nTg/PBS, nTg/GQDs, hA53T  $\alpha$ -syn Tg/PBS, and hA53T  $\alpha$ -syn Tg/GQDs (n=6, biologically independent animals; two-way ANOVA with a post hoc Bonferroni test, NS, not significant; error bars are the standard deviation). l, The effect of GQDs on  $\alpha$ -syn aggregate formation in HEK293 cells with hA53T  $\alpha$ -syn overexpression. HEK293T cells were transfected with pCMV5-myc-A53T  $\alpha$ -syn and the test groups were treated with GQDs (0.1  $\mu$ g/ml). After 48 hours, cells were immunostained with  $\alpha$ -syn antibodies. m, The number of immuno-positive aggregates per field was quantified and normalised. Mean  $\pm$  s.d. values are  $57.29 \pm 8.45$  and  $14.94 \pm 5.15$  for PBS and GQDs (n=7, biologically independent samples; two-tailed Student's t-test). Single-headed arrows mark  $\alpha$ -syn aggregates.

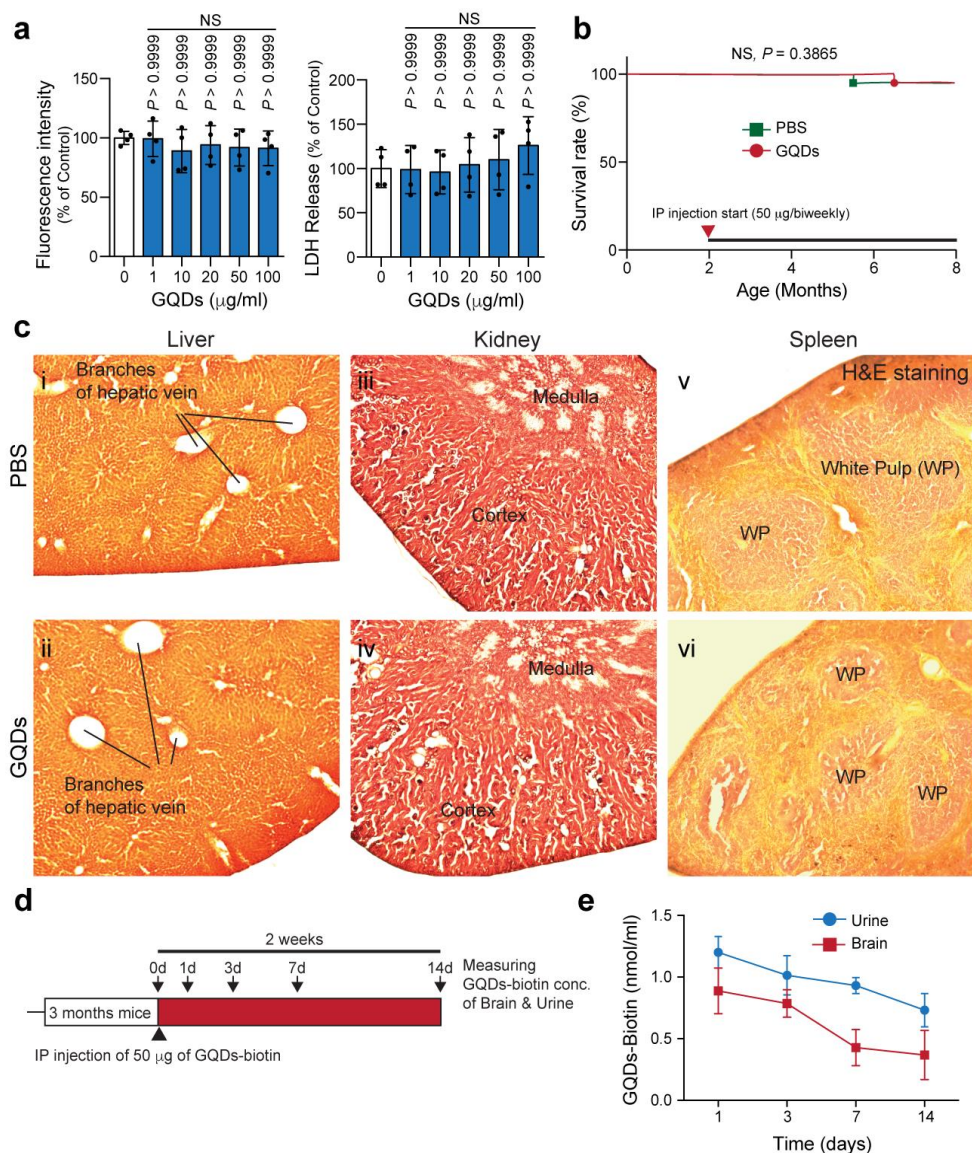


**Figure 3-S12.** Long-term *in vitro* and *in vivo* toxicity of GQDs. **a**, Cytotoxicity measurements of GQDs on DIV 10 primary cortical neurons after 7 days of incubation with alamarBlue and LDH assays. Mean  $\pm$  s.d. values are  $100.00 \pm 5.65$ ,  $99.33 \pm 15.08$ ,  $89.03 \pm 18.25$ ,  $94.10 \pm 16.30$ ,  $91.95 \pm 15.50$ , and  $91.35 \pm 7.31$  for alamarBlue assay;  $100.00 \pm 21.21$ ,  $99.02 \pm 27.10$ ,  $96.14 \pm 24.87$ ,  $104.31 \pm 30.70$ ,  $110.13 \pm 34.19$ , and  $126.05 \pm 32.53$  for LDH assays. ( $n=4$ , biologically independent samples; oneway ANOVA with a post hoc Bonferroni test, NS, not significant). **b**, Survival curves of GQDs injected mice.  $50 \mu\text{g}$  of GQDs or vehicle were i.p. injected in C57BL/6 mice biweekly for 6 months and *in vivo* toxicity of GQDs was monitored ( $n=20$ , biologically independent animals; Log-rank test; NS, not significant). Statistically, there is no significant difference between GQDs and vehicle-injected control groups after 8 months. **c**, Representative haematoxylin and eosin

(H&E) staining images of the major organs. The nuclei and eosinophilic structure of the liver, kidney, and spleen of GQDs-injected group (n=3, biologically independent animals) were compared to the PBS-injected control group (n=3, biologically independent animals). d, Schematic illustration of the injection and sampling methods for *in vivo* tracking of GQDs-biotin. e, 50  $\mu\text{g}$  of GQDs-biotin were i.p. injected in C57BL/6 mice. The concentrations of GQDs-biotin were measured using the brain (red) or urine (blue) of GQDs-biotin-injected mice at various time points (1, 3, 7, and 14 days). Mean  $\pm$  s.d. values are  $1.21 \pm 0.13$ ,  $1.02 \pm 0.16$ ,  $0.92 \pm 0.07$ , and  $0.73 \pm 0.14$  at 1, 3, 7, and 14 days for Urine;  $0.89 \pm 0.19$ ,  $0.79 \pm 0.11$ ,  $0.43 \pm 0.15$ , and  $0.37 \pm 0.20$  at 1, 3, 7, and 14 days for Brain (n=4, biologically independent animals).



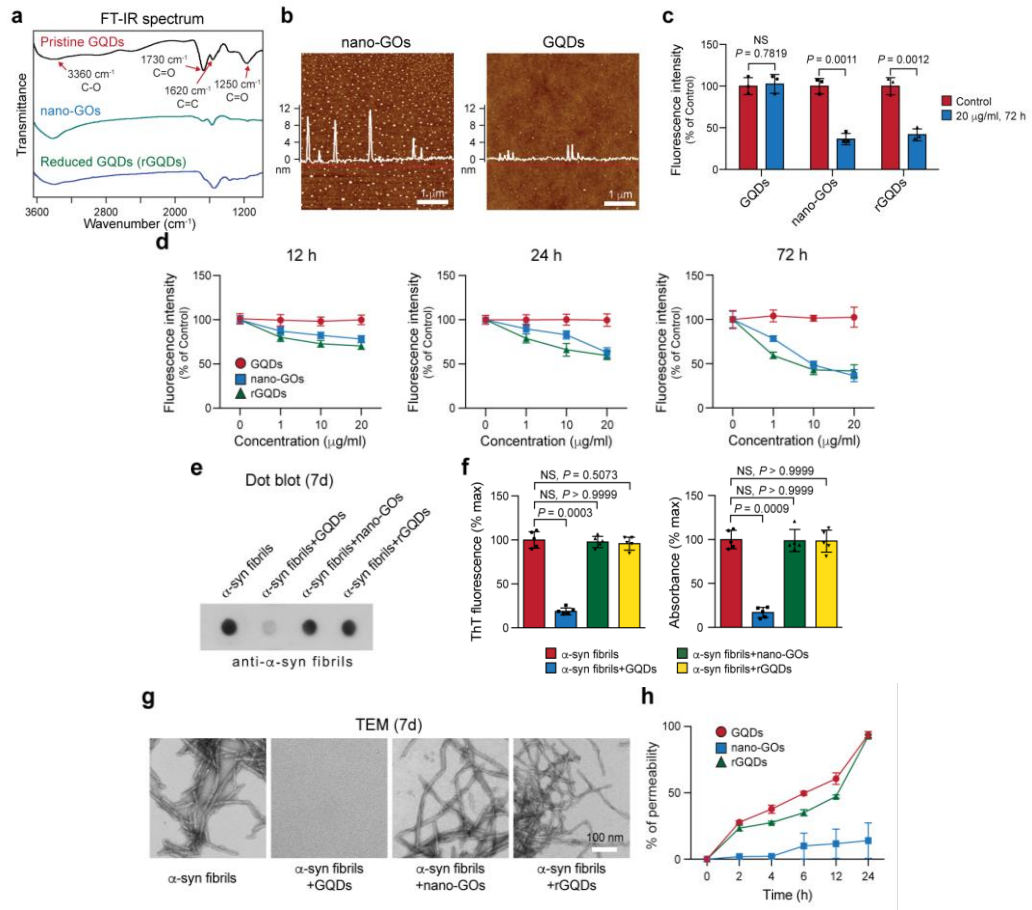


**Figure 3-S13.** The comparative effects of nano-GOs and rGQDs on  $\alpha$ -syn PFFs induced primary neuronal toxicity, disaggregation of fibrils and the BBB permeability. a, FT-IR spectra of pristine GQDs (black), nano-GOs (green), and reduced GQDs (rGQDs, purple) with designated peaks for the functional groups. b, AFM images of nano-GOs and GQDs with representative line profiles. c, Quantifications of the cell toxicities after 72 hours of incubation with 20  $\mu$ g/ml of each material. Mean  $\pm$  s.d. values are 100.00  $\pm$  10.17, 102.59  $\pm$  11.26, 100.00  $\pm$  9.27, 36.52  $\pm$  6.92, 100.00  $\pm$  10.11, and 41.66  $\pm$  7.23 for GQDs-control, GQDs-72 h, nano-GOs-control, nano-GOs-72 h, rGQDs-control, and rGQDs-72 h (n=3, biologically independent samples; two-tailed Student's t-test; NS, not significant). d, The cell toxicities monitored in SH-SY5Y cells by alamarBlue assay at 12, 24, and 72 hours with various concentrations of each material (1, 10, and 20  $\mu$ g/ml). Mean  $\pm$  s.d. values are 100.00  $\pm$  5.86, 99.56  $\pm$  5.29, 98.23  $\pm$  4.88, and 99.98  $\pm$  5.43 at 12 hours with PBS, 1, 10, and 20  $\mu$ g/ml of GQDs; 100.00  $\pm$  4.62, 87.11  $\pm$  4.12, 82.47  $\pm$  3.49, and 78.23  $\pm$  3.86 at 12 hours with PBS, 1, 10, and 20  $\mu$ g/ml of nano-GOs; 100.00  $\pm$  4.62, 80.30  $\pm$  4.76, 72.83  $\pm$  3.78, and 70.46  $\pm$  3.92 at 12 hours with PBS, 1, 10, and 20  $\mu$ g/ml of rGQDs; 100.00  $\pm$  5.08, 99.90  $\pm$  5.81, 100.12  $\pm$  6.18, and 99.65  $\pm$  6.88 at 24 hours with PBS, 1, 10, and 20  $\mu$ g/ml of GQDs; 100.00  $\pm$  5.08, 99.90  $\pm$  5.81, 100.12  $\pm$  6.18, and 99.65  $\pm$  6.88 at 24 hours with PBS, 1, 10, and 20  $\mu$ g/ml of nano-GOs; 100.00  $\pm$  5.08, 99.90  $\pm$  5.81, 100.12  $\pm$  6.18, and 99.65  $\pm$  6.88 at 24 hours with PBS, 1, 10, and 20  $\mu$ g/ml of rGQDs.

GQDs;  $100.00 \pm 5.31$ ,  $89.91 \pm 5.39$ ,  $82.98 \pm 4.62$ , and  $63.00 \pm 5.48$  at 24 hours with PBS, 1, 10, and 20  $\mu\text{g/ml}$  of nano-GOs;  $100.00 \pm 3.21$ ,  $78.96 \pm 5.21$ ,  $66.12 \pm 7.08$ , and  $59.73 \pm 4.56$  at 24 hours with PBS, 1, 10, and 20  $\mu\text{g/ml}$  of rGQDs;  $100 \pm 10.17$ ,  $104.03 \pm 6.78$ ,  $101.38 \pm 3.27$ , and  $102.59 \pm 11.26$  at 72 hours with PBS, 1, 10, and 20  $\mu\text{g/ml}$  of GQDs;  $100.00 \pm 9.27$ ,  $78.34 \pm 3.30$ ,  $48.53 \pm 4.28$ , and  $36.52 \pm 6.92$  at 72 hours with PBS, 1, 10, and 20  $\mu\text{g/ml}$  of nano-GOs;  $100.00 \pm 10.11$ ,  $59.37 \pm 3.67$ ,  $43.04 \pm 5.47$ , and  $41.66 \pm 7.23$  at 72 hours with PBS, 1, 10, and 20  $\mu\text{g/ml}$  of rGQDs. (n=3, biologically independent samples). e, The comparative dissociation effects of GQDs, nano-GOs, and rGQDs assessed by dot blot, f, ThT and turbidity assays. Mean  $\pm$  s.d. values are  $100.00 \pm 9.35$ ,  $18.86 \pm 4.11$ ,  $97.86 \pm 6.57$ , and  $95.42 \pm 8.77$  for  $\alpha$ -syn fibrils,  $\alpha$ -syn fibrils+GQDs,  $\alpha$ -syn fibrils+nano-GOs, and  $\alpha$ -syn fibrils+GQDs of ThT assay and  $100.00 \pm 10.46$ ,  $17.06 \pm 5.99$ ,  $98.84 \pm 12.86$ , and  $98.14 \pm 12.35$  for  $\alpha$ -syn fibrils,  $\alpha$ -syn fibrils+GQDs,  $\alpha$ -syn fibrils+nano-GOs, and  $\alpha$ -syn fibrils+GQDs of turbidity assay (n=5, biologically independent animals; one-way ANOVA with a post hoc Bonferroni test, NS, not significant). g, TEM images after 7 days of incubation (each with 5 mg/ml concentration; n=3, independent experiments). h, *In vitro* BBB permeabilities of GQDs, nano-GOs, and rGQDs using the *in vitro* BBB model in Fig. 3-S9. Mean  $\pm$  s.d. values are  $27.9 \pm 1.29$ ,  $37.71 \pm 3.07$ ,  $49.65 \pm 1.52$ ,  $60.78 \pm 4.28$ , and  $93.65 \pm 2.55$  at 2, 4, 6, 12, 24 hours of GQDs;  $1.92 \pm 0.90$ ,  $2.22 \pm 0.20$ ,  $9.97 \pm 9.55$ ,  $11.73 \pm 11.06$ , and  $14.06 \pm 13.29$  at 2, 4, 6, 12, 24 hours of nano-GOs;  $23.33 \pm 4.27$ ,  $27.70 \pm 1.97$ ,  $35.10 \pm 4.73$ ,  $47.29 \pm 2.24$ , and  $92.74 \pm 2.28$  at 2, 4, 6, 12, 24 hours of rGQDs (n=4, biologically independent samples).

## 1.6. References

1. Dawson, T. M. & Dawson, V. L. Molecular pathways of neurodegeneration in Parkinson's disease. *Science* **302**, 819–822 (2003).
2. Spillantini, M. G. *et al.* Alpha-synuclein in Lewy bodies. *Nature* **388**, 839–840 (1997).
3. Li, J. Y. *et al.* Lewy bodies in grafted neurons in subjects with Parkinson's disease suggest host-to-graft disease propagation. *Nat. Med.* **14**, 501–503 (2008).
4. Desplats, P. *et al.* Inclusion formation and neuronal cell death through neuron-to-neuron transmission of alpha-synuclein. *Proc. Natl Acad. Sci. USA* **106**, 13010–13015 (2009).
5. Volpicelli-Daley, L. A. *et al.* Exogenous alpha-synuclein fibrils induce Lewy body pathology leading to synaptic dysfunction and neuron death. *Neuron* **72**, 57–71 (2011).
6. Luk, K. C. *et al.* Pathological alpha-synuclein transmission initiates Parkinson-like neurodegeneration in nontransgenic mice. *Science* **338**, 949–953 (2012).
7. Varela, L., Bell, C. H., Armitage, J. P. & Redfield, C.  $^1\text{H}$ ,  $^{13}\text{C}$  and  $^{15}\text{N}$  resonance assignments for the response regulator CheY3 from *Rhodobacter sphaeroides*. *Biomol. NMR Assign.* **10**, 373–378 (2016).
8. Bodner, C. R., Dobson, C. M. & Bax, A. Multiple tight phospholipid-binding modes of alpha-synuclein revealed by solution NMR spectroscopy. *J. Mol. Biol.* **390**, 775–790 (2009).
9. Tuttle, M. D. *et al.* Solid-state NMR structure of a pathogenic fibril of full-length human alpha-synuclein. *Nat. Struct. Mol. Biol.* **23**, 409–415 (2016).
10. Giasson, B. I., Murray, I. V. J., Trojanowski, J. Q. & Lee, V. M. Y. A hydrophobic stretch of 12 amino acid residues in the middle of alpha-synuclein is essential for filament assembly. *J. Biol. Chem.* **276**, 2380–2386 (2001).
11. van Stokkum, I. H., Spoelder, H. J., Bloemendal, M., van Grondelle, R. & Groen, F. C. Estimation of protein secondary structure and error analysis from circular dichroism spectra. *Anal. Biochem.* **191**, 110–118 (1990).

12. Sreerama, N. & Woody, R. W. Estimation of protein secondary structure from circular dichroism spectra: comparison of CONTIN, SELCON, and CDSSTR methods with an expanded reference set. *Anal. Biochem.* **287**, 252–260 (2000).
13. Lin, M. T. & Beal, M. F. Mitochondrial dysfunction and oxidative stress in neurodegenerative diseases. *Nature* **443**, 787–795 (2006).
14. Czupalla, C. J., Liebner, S. & Devraj, K. In vitro models of the blood–brain barrier. *Methods Mol. Biol.* **1135**, 415–437 (2014).
15. Lee, M. K. *et al.* Human  $\alpha$ -synuclein-harboring familial Parkinson’s disease-linked Ala-53→ Thr mutation causes neurodegenerative disease with  $\alpha$ -synuclein aggregation in transgenic mice. *Proc. Natl Acad. Sci. USA* **99**, 8968–8973 (2002).
16. Brahmachari, S. *et al.* Activation of tyrosine kinase c-Abl contributes to  $\alpha$ -synuclein-induced neurodegeneration. *J. Clin. Invest.* **126**, 2970–2988 (2016).
17. Li, Q. *et al.* Modulating A $\beta$  33–42 peptide assembly by graphene oxide. *Chem. Eur. J.* **20**, 7236–7240 (2014).
18. Mahmoudi, M., Akhavan, O., Ghavami, M., Rezaee, F. & Ghiasi, S. M. A. Graphene oxide strongly inhibits amyloid beta fibrillation. *Nanoscale* **4**, 7322–7325 (2012).
19. Liu, Y. *et al.* Graphene quantum dots for the inhibition of beta amyloid aggregation. *Nanoscale* **7**, 19060–19065 (2015).
20. Yang, Z. X. *et al.* Destruction of amyloid fibrils by graphene through penetration and extraction of peptides. *Nanoscale* **7**, 18725–18737 (2015).
21. Volpicelli-Daley, L. A., Luk, K. C. & Lee, V. M. Addition of exogenous alpha-synuclein preformed fibrils to primary neuronal cultures to seed recruitment of endogenous alpha-synuclein to Lewy body and Lewy neurite-like aggregates. *Nat. Protoc.* **9**, 2135–2146 (2014).
22. Delaglio, F. *et al.* NMRPipe: a multidimensional spectral processing system based on UNIX pipes. *J. Biomol. NMR* **6**, 277–293 (1995).
23. Lee, W., Tonelli, M. & Markley, J. L. NMRFAM-SPARKY: enhanced

- software for biomolecular NMR spectroscopy. *Bioinformatics* **31**, 1325–1327 (2015).
24. Abraham, M. J. *et al.* GROMACS: High performance molecular simulations through multi-level parallelism from laptops to supercomputers. *SoftwareX* **1-2**, 19–25 (2015).
25. Mackerell, A. D.Jr., Feig, M. & Brooks, C. L. III Extending the treatment of backbone energetics in protein force fields: limitations of gas-phase quantum mechanics in reproducing protein conformational distributions in molecular dynamics simulations. *J. Comput. Chem.* **25**, 1400–1415 (2004).
26. Yu, W., He, X., Vanommeslaeghe, K. & MacKerell, A. D. Jr. Extension of the CHARMM General Force Field to sulfonyl-containing compounds and its utility in biomolecular simulations. *J. Comput. Chem.* **33**, 2451–2468 (2012).
27. Lee, M. K. *et al.* Human  $\alpha$ -synuclein-harboring familial Parkinson's disease-linked Ala-53 $\rightarrow$  Thr mutation causes neurodegenerative disease with  $\alpha$ -synuclein aggregation in transgenic mice. *Proc. Natl Acad. Sci. USA* **99**, 8968–8973 (2002).
28. Peelaerts, W. *et al.*  $\alpha$ -Synuclein strains cause distinct synucleinopathies after local and systemic administration. *Nature* **522**, 340–344 (2015).
29. Mao, X. *et al.* Pathological  $\alpha$ -synuclein transmission initiated by binding lymphocyte-activation gene 3. *Science* **353**, aah3374 (2016).
30. Park, C. *et al.* TLR3-mediated signal induces proinflammatory cytokine and chemokine gene expression in astrocytes: differential signaling mechanisms of TLR3-induced IP-10 and IL-8 gene expression. *Glia* **53**, 248-256, doi:10.1002/glia.20278 (2006).
31. Guyenet, S. J. *et al.* A simple composite phenotype scoring system for evaluating mouse models of cerebellar ataxia. *J Vis Exp*, doi:10.3791/1787 (2010).
32. Marcano, D. C. *et al.* Improved synthesis of graphene oxide. *ACS Nano* **4**, 4806-4814, doi:10.1021/nn1006368 (2010).

## ***Chapter 4***

### ***Graphene Quantum Dots Alleviate Impaired Functions in Niemann-Pick Type C Disease in vivo***

#### **1.1. Abstract**

While the neuropathological features in Niemann-Pick type C disease (NPC) are fatal, development of clinically available therapeutic agent remains as a challenge to date. Here we report graphene quantum dots (GQDs) as a potential candidate against impaired functions in NPC *in vivo*. In addition to the previous findings that GQDs exhibit negligible long-term toxicity with an ability to penetrate the blood-brain barrier (BBB), GQDs treatment decreases the accumulation of intracellular cholesterol through physical interactions both *in vitro* and *in vivo*. GQDs are also found to induce autophagy to restore compromised autophagic flux, which eventually reduces the atypical accumulation of autophagic vacuoles. Moreover, GQDs injection prevents the loss of Purkinje cells in the cerebellum with decreased microglial activation. The finding that GQDs alleviate impaired functions in NPC provides a promising potential for the treatment of NPC and related lysosomal storage disorders (LSDs).

---

\* This chapter is reproduced from: Insung Kang<sup>†</sup>, Je Min Yoo<sup>†</sup>, Donghoon Kim, Dong Jin Kim, Seung Eun Lee, Juhee Kim, Byung-Chul Lee, Jin Young Lee, Jae-Jun Kim, Nari Shin, Young-Ho Lee, Byung Hee Hong and Kyung-Sun. (In Preparation)

## 1.2. Introduction

Niemann-Pick type C disease (NPC) is a representative lysosomal storage disorder (LSD) characterized by heterogeneous neurovisceral symptoms including hepatosplenomegaly, cerebellar ataxia, and dementia at various age onsets.<sup>1</sup> The pathogenesis of NPC is associated with the deficiency in either protein: NPC1 or NPC2, which harbour in the late endosomal/lysosomal (LE/LY) compartments. As the proteins play pivotal roles in intracellular cholesterol efflux machinery, defective expression of either protein leads to abnormal accumulation of unesterified cholesterol in the LE/LY compartments.<sup>2-4</sup>

While the pathological manifestations are observed throughout the body, neuronal dysfunction and degeneration pertaining to the cerebellum involve the most deleterious and ultimately fatal features in patients.<sup>4,5</sup> The progression of neurodegeneration in NPC is known to be provoked by multiple factors. Foremost, the atypical cholesterol confinement disrupts cholesterol-derived cellular events including neurosteroidogenesis.<sup>6</sup> The inclusions in the LE/LY compartments are recognized as damage-associated molecular patterns (DAMPs) as well, which eventually induce prolonged neuroinflammation indicated by activation of microglia/astrocytes.<sup>7-8</sup> In addition, recent findings have revealed the role of NPC1 in amphisome formation; compromised autophagic flux by defective NPC1 expression contributes to the accumulation of autophagic vacuoles and subsequent cell death in NPC.<sup>9</sup> Despite the urgent demand to treat neurodegenerative pathophysiology, no clinical drug is available for NPC patients thus far.<sup>10</sup> While the recent outcomes with hydroxypropyl  $\beta$ -cyclodextrin (HP $\beta$ CD) through phase 1-2 clinical trials showed delays in disease progression, the major drawbacks of

HP $\beta$ CD remain unsolved.<sup>11-13</sup> Namely, not only is HP $\beta$ CD unable to penetrate the blood-brain barrier (BBB), but also known to interfere with the autophagic flux to further complicate the relevant issues.

In the current study, we sought to investigate the potential efficacy of graphene quantum dots (GQDs) against defective functions in NPC. GQDs are gaining growing interests in the field of nanomedicine by virtue of their notable properties. In particular, our group recently reported GQDs' therapeutic role against  $\alpha$ -synucleinopathy in Parkinson's disease (PD), through which their negligible long-term toxicity and ability to penetrate the BBB have been validated *in vivo*.<sup>14</sup> Moreover, different studies have shown graphene-based materials' ability to interact with cholesterol<sup>15,16</sup> and GQDs' role in the promotion of autophagic flux,<sup>17,18</sup> which are seemingly advantageous to manage the impaired functions in NPC.

### 1.3. Results and Discussion

GQDs were synthesized by thermo-oxidative cutting of carbon fibres in strong acid, and the properties were analysed with transmission electron microscopy (TEM), Raman spectroscopy, atomic force microscopy (AFM) and Fourier transform infrared spectroscopy (FT-IR) (Fig. 4-S1). To evaluate GQDs' therapeutic potential *in vitro*, NPC patient-derived induced neural stem cells (NPC-iNSCs) were generated according to the previous reports.<sup>19-20</sup> Preliminarily, the relative levels of NSC-specific markers: SOX2, PAX6, Nestin, Ki67 in H9-derived human NSCs, wild-type NSCs (WT-NSCs) and NPC-iNSCs were measured to ensure the proper induction of neural lineage in NPC-iNSCs (Fig. 4-S2). The



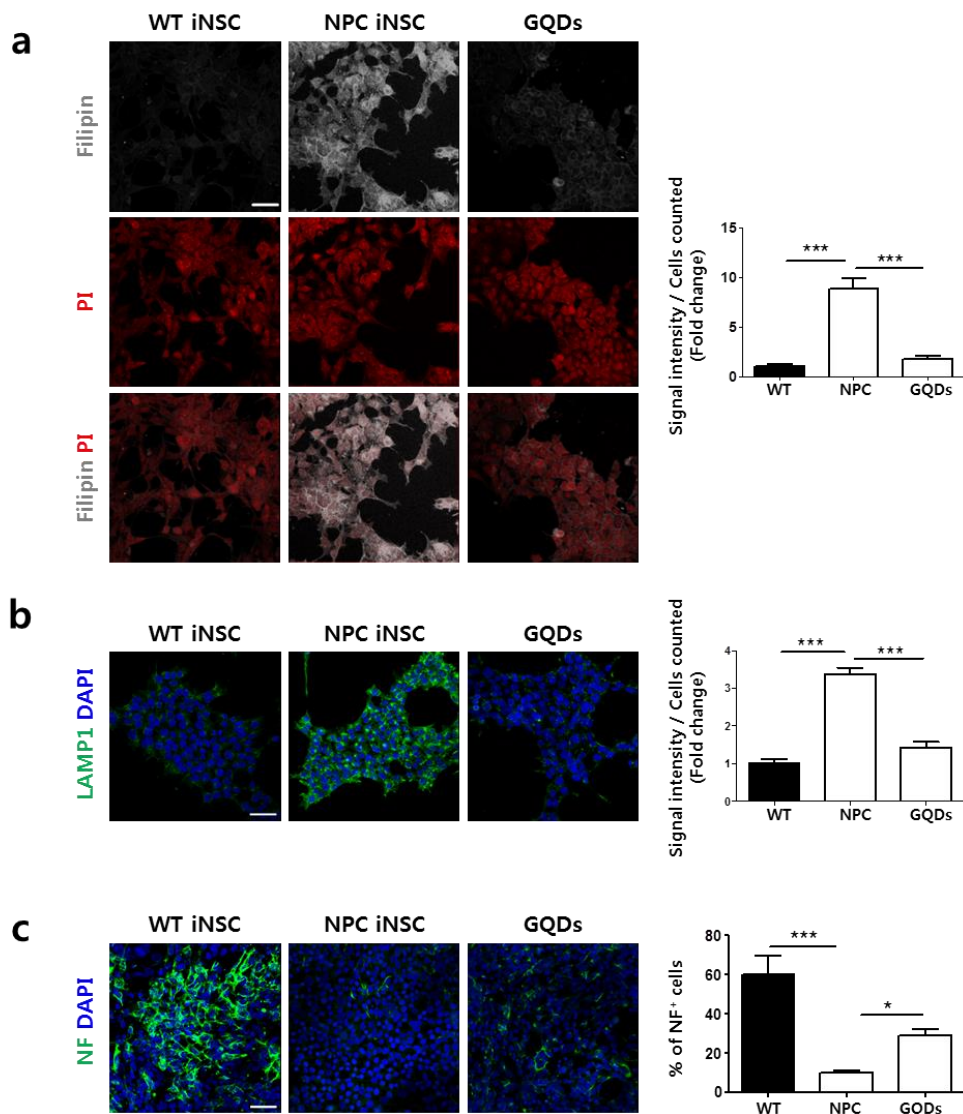


**Figure 4-1. The effect of GQDs on abnormal characteristics in NPC-iNSC.** **a**, Cholesterol accumulation assessed by filipin assay treated in WT iNSC and the presence and absence of GQDs (1  $\mu$ g/ml) in NPC iNSC for 3 days. **b**, Aggregation of lysosomes was visualized by fluorescence images of LAMP1 antibody in NPC iNSC was compared with WT iNSC and GQDs (1  $\mu$ g/ml) treated NPC iNSC. **c**, Staining for Neurofilament (NF) in WT iNSC and NPC iNSC treated with or without GQDs (1  $\mu$ g/ml) for 3days. Scale bars, 100  $\mu$ m. Data are presented as mean  $\pm$  standard error of the mean (s.e.m) from three independent experiments. Significance levels are expressed as asterisks: \* $P < 0.05$ , \*\*\* $P < 0.001$  via one-way ANOVA with Tukey's multiple comparisons test.

pathological hallmarks of NPC were subsequently investigated by quantifying the levels of intracellular cholesterol and lysosomal-associated membrane protein 1 (LAMP1) by immunostaining with filipin and LAMP1 antibody (Fig. 4-1a,b). While the levels of cholesterol and LAMP1 respectively exhibited 6-fold and 2-fold increases in NPC-iNSCs, the same analyses showed the predominant reduction of atypical accumulations 3 days post-GQDs treatment. It should also be noted that the decreased ability to differentiate in NPC-iNSCs, indicated by immature neuronal marker neurofilament (NF), was significantly recovered by GQDs as well (Fig. 4-1c).

As hinted from the previous reports that discussed graphene-based materials' specific interactions with cholesterol, we sought to elucidate the mechanism of cholesterol depletion by GQDs through proton nuclear magnetic resonance ( $^1\text{H}$  NMR) spectroscopy at the molecular level (Fig. 4-2a and Fig. 4-S3).<sup>15,16</sup> Since cholesterol is only soluble in a few organic solvents including dimethyl sulfoxide (DMSO), all samples were prepared in 2% DMSO solution. Even in 2% DMSO, the NMR peak intensities of cholesterol were not strong enough to analyse. This is likely to be associated with the slow tumbling effect (i.e. fast relaxation of transverse magnetization) observed from molecules with high molecular weight, which suggests that cholesterol exists as huge aggregates in solution. Notably, the  $^1\text{H}$  NMR spectra of cholesterol exhibited distinct peak changes by the presence of GQDs. In particular, the peak intensities in 3.2 – 4.0 ppm region considerably increased with a few newly appeared sharp signals (Fig. 4-2a). The outcome suggests the compelling evidence for physical interactions between GQDs and cholesterol, and subsequent solubilization of cholesterol to yield the new peaks. The result is in line with the previous finding where GQDs

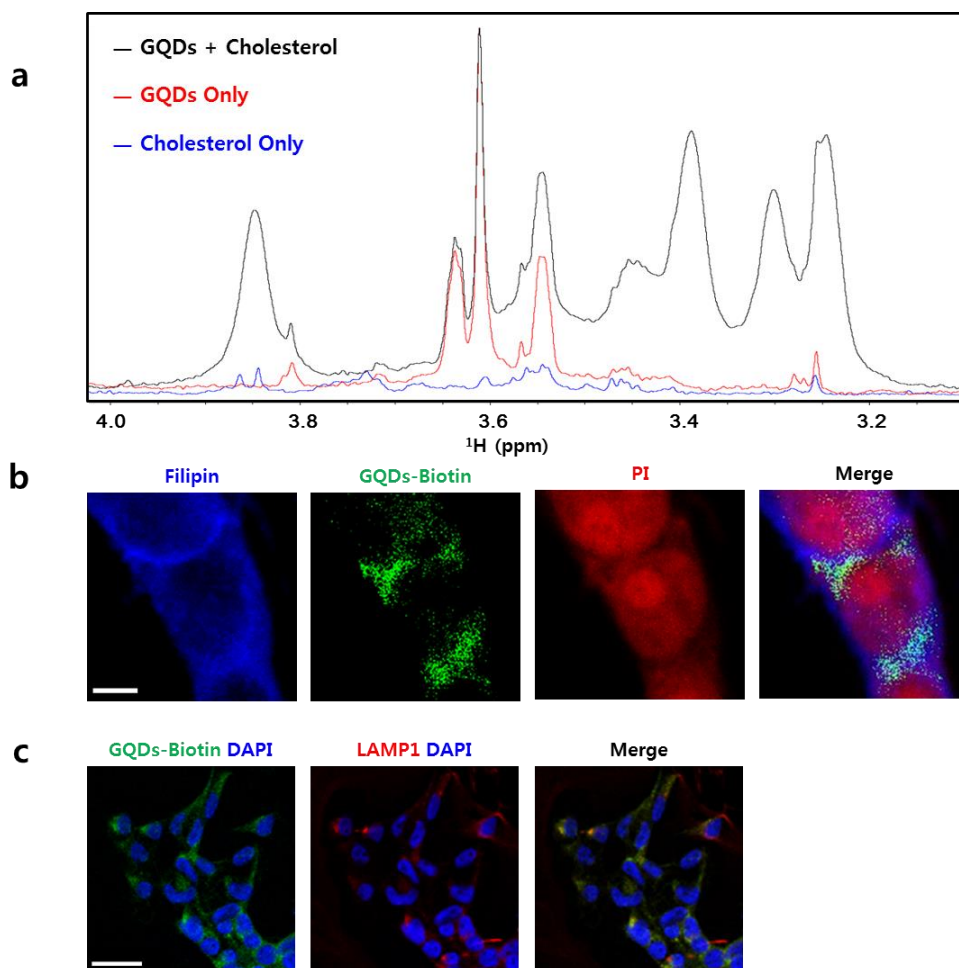


**Figure 4-2. Analysis of the interaction between GQDs and cholesterol in NPC-iNSC. a,** One-dimensional  $^1\text{H}$  NMR spectra. NMR spectra of cholesterol only (blue), GQDs only (red), and cholesterol in the presence of GQDs (black). **b,** Magnified fluorescence images showing the GQDs-Biotin merge with cholesterol (Filipin) of NPC-iNSC cells. The concentration of GQDs-Biotin was 1  $\mu\text{g}/\text{ml}$  and treated for 24 hours. Nuclei were stained with PI (red). Scale bar, 10  $\mu\text{m}$ . **c,** Co-localization studies of GQDs-Biotin (green) and lysosome (red) using LAMP1 antibody. Scale bar, 50  $\mu\text{m}$ .

disaggregated insoluble  $\alpha$ -synuclein aggregates in solution.<sup>14</sup> To visually corroborate the interactions intracellularly, co-immunostaining of filipin and biotinylated GQDs was performed in NPC-iNSCs (Fig. 4-2b and Fig. 4-S4b). As shown from the image, GQDs-biotin and filipin exhibited strong co-localized

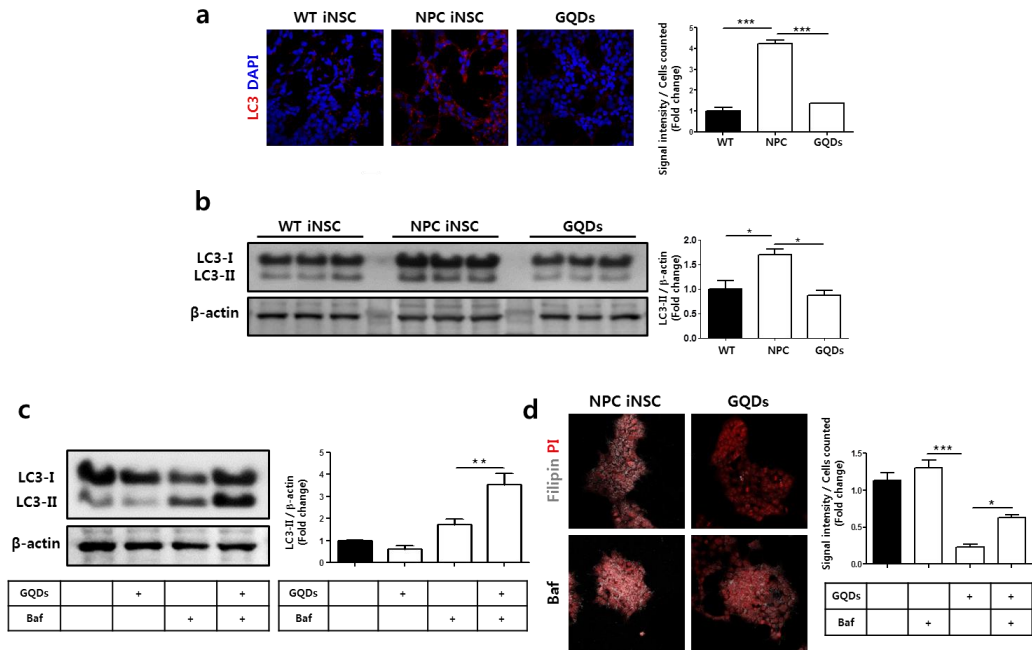


**Figure 4-3. The effect of GQDs on impaired autophagy *in vitro*.** **a**, Fluorescence images of LC3 (red) of WT iNSC and NPC iNSC in the presence and absence of GQDs (1  $\mu$ g/ml) treated for 3 days. Nuclei were stained with DAPI (blue). **b**, Immunoblot of LC3 antibody in protein samples from WT iNSC, NPC iNSC and NPC iNSC + GQDs. **c**, Representative immunoblot levels with LC3 antibody in NPC1 iNSC, NPC1 iNSC + GQDs, following 24 h treatment with baf1. **d**, Filipin staining for unesterified cholesterol in NPC1 iNSC treated with baf1, GQDs. Scale bars, 100  $\mu$ m. Data are presented as mean  $\pm$  standard error of the mean (s.e.m) from three independent experiments. Significance levels are expressed as asterisks: \* $P < 0.05$ , \*\* $P < 0.01$ , \*\*\* $P < 0.001$  via one-way ANOVA with Tukey's multiple comparisons test.

signals throughout the cell bodies after 24 hours of incubation. In accordance with Figure 1A and Figure S4A, the levels of filipin gradually decreased in time and showed significant reduction 3 days post-GQDs-biotin treatment. Co-immunostaining of GQDs-biotin and LAMP1 antibody was also performed to verify lysosomal localization of GQDs to confirm GQDs-mediated cholesterol depletion in the lysosome (Fig. 4-2c). Indeed, GQDs-biotin was heavily localized

in the lysosome, which is in agreement with the GQDs-mediated  $\alpha$ -synuclein disaggregation in the lysosome. Taken together, intracellular cholesterol depletion by GQDs mainly takes place in the lysosome, through their physical interactions.

As mentioned, defective expression of NPC1 compromises autophagic pathway by disabling the fusion of autophagosome and late endosome to form amphisome.<sup>9</sup> Therefore, the role of GQDs in the autophagic flux and subsequent accumulation of autophagic vacuoles was explored. The atypical accumulation of autophagic vacuoles can be measured by the level of microtubule-associated protein 1 light-chain 3 (LC3). In particular, the amount of phosphatidylethanolamine-conjugated LC3 (LC3-II) increases as it correlates with the level of the autophagosome. As shown in Fig. 4-3a and b, the levels of LC3-I and LC3-II were dramatically elevated in NPC-iNSCs as assessed by Western blot and immunohistochemistry analyses. On the other hand, the same assessments exhibited normal levels in the presence of GQDs. To further investigate the effect of GQDs on LC3-II accumulation and autophagic flux, bafilomycin A1 (Baf A1) was treated to block autophagic degradation (Fig. 4-3c). Although Baf A1 treatment aggravates LC3-II accumulation by inhibiting clearance, it does not promote the synthesis of the autophagosome. Surprisingly, co-treatment of GQDs and Baf A1 caused significant increases in LC3-II accumulation. This indicates GQDs' robust induction of autophagy, which seems to play the pivotal role in the clearance/maturation of LC3-II in NPC-iNSCs. In addition, GQDs and Baf A1 co-treatment complicated intracellular cholesterol accumulation; GQDs-mediated autophagy induction is strongly associated with GQDs-mediated cholesterol clearance as well (Fig. 4-3d).

To evaluate GQDs' therapeutic potential against the impaired functions *in*

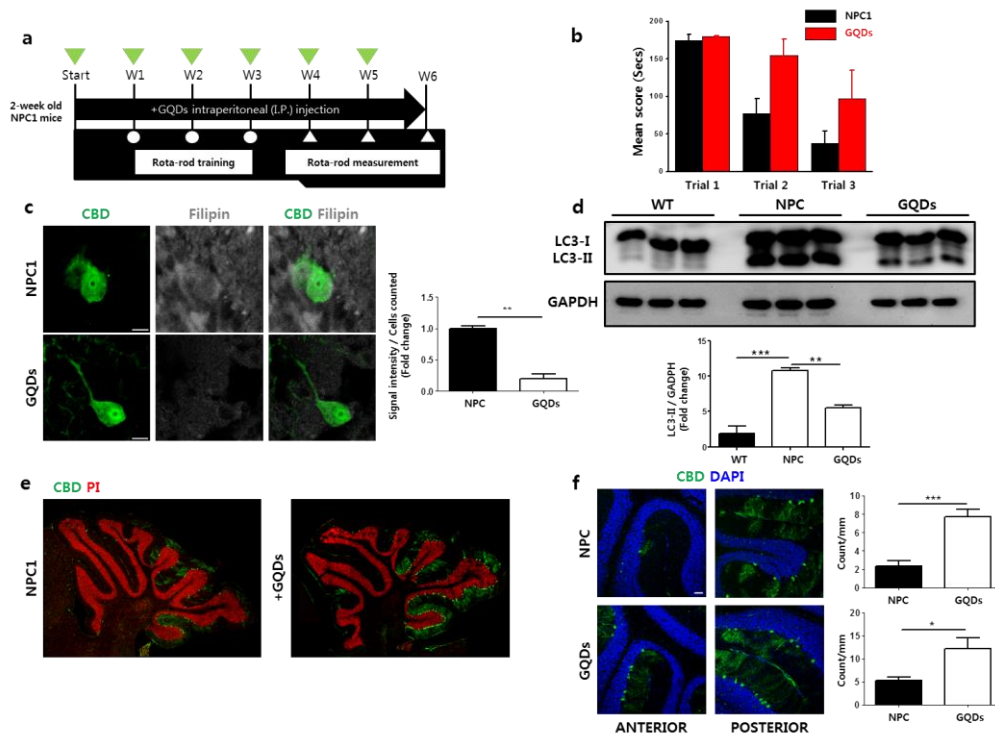


**Figure 4-4. The effect of GQDs on NPC1 pathologies *in vivo*.** **a**, Schematic representation of injection of GQDs (50 µg/ml) for intraperitoneal injection in NPC1 mutant mice. GQDs were injected weekly for 6 weeks. **b**, Assessments of the behavioral deficits measured by Rota-rod test. Mean values are ~ for NPC1 and NPC1+GQDs (n=7). **c**, Representative calbindin (CBD) immunostaining purkinje cells co-stained with filipin. Quantification of filipin intensities in CBD area normalized to NPC1. Mean values are 1.00 and 0.19 for NPC1 and NPC1+GQDs. Scale bar 10 µm. **d**, Immunoblot analysis of LC3 in the cerebellum tissues of WT, NPC1 and NPC1+GQDs. LC3-II level was analyzed and quantified by normalizing to WT. Mean values are 1.88, 10.80 and 5.49 for WT, NPC1 and NPC1+GQDs. **e**, Representative immunohistochemistry image of the cerebella labeled with anti-CBD for purkinje cells of NPC1 and NPC1+GQDs. Nuclei were stained with PI. **f**, Purkinje cells were labeled with anti-CBD in the anterior and posterior of NPC1 and NPC1+GQDs cerebellum. Nuclei were counterstained with DAPI. Quantification of purkinje cells were counted divided by the length of the cerebella lobe. Data are presented as mean ± standard error of the mean (s.e.m) from three independent experiments. Significance levels are expressed as asterisks: \*P < 0.05, \*\*P < 0.01, \*\*\*P < 0.001 via one-way ANOVA with Tukey's multiple comparisons test.

*vivo*, GQDs (2 mg/kg; 50 µg) were administered into 2-week old NPC1 knockout mice weekly via intraperitoneal (i.p.) injection (Fig. 4-4a). Prior to any assessments, the BBB permeability of GQDs was re-evaluated (Fig. 4-S5). As it has already thoroughly verified from the previous report, we focused on: 1) *In vitro* permeability to ensure the reproducibility and 2) *In vivo* cerebellar localization of GQDs. As expected, GQDs exhibited 100% *in vitro* permeability after 24 hours and considerable amount of GQDs-biotin was found in the cerebellum without any appreciable toxicity. From 4 to 6 weeks post-GQDs injection, the rota-rod tests were carried out to monitor the changes in NPC-provoked motor deficits (Fig. 4b). While NPC1 mice showed significantly aggravating motor dysfunctions in time, GQDs-treated mice displayed respectably improved latency to fall.

At 6 weeks post-GQDs injection, mice were sacrificed to analyze biochemical alterations of the pathological features in the cerebellum. As the loss Purkinje cells is the most striking and detrimental histological change in NPC1 mice, the atypical cholesterol accumulation in Purkinje cells was explored by immunohistochemical analysis (Fig. 4-4c). While considerable amount of cholesterol accumulation was detected in Purkinje cells of NPC1 mice, GQDs injection markedly prevented the abnormal accumulation. The accumulation of LC3-II autophagic vacuoles was also measured by Western blot analysis, showing predominant reduction by GQDs (Fig. 4-4d). Furthermore, GQDs' protective effect of on the loss of Purkinje cells was monitored by Calbindin-D 28K (CBD) staining in the cerebellum (Fig. 4-4e,f).<sup>21</sup> Remarkably, the Purkinje cells in GQDs-administered NPC1 mice were significantly protected against NPC1-induced loss over the entire cerebellum. It should be also noted that GQDs-injected NPC1 mice showed decreased amount of activated microglia in the cerebellum, assessed by

immunostaining with Iba1 antibody (Fig. 4-S6). This indicates only negligible involvement of inflammatory response by the presence of GQDs, which is likely associated with the rescue of Purkinje cells.

## 1.4. Conclusion

In this study, we investigated the potential role of GQDs against the impaired functions in NPC. In addition to the previous finding that revealed GQDs' negligible long-term toxicity and ability to penetrate the BBB *in vivo*, GQDs were found to deplete intracellular cholesterol and promote autophagic flux. As GQDs' neuroprotective effects against  $\alpha$ -synucleinopathy in Parkinson's disease (PD) have been validated as well, their therapeutic potential against other types of LSDs including Gaucher's disease would also be noteworthy as the disease manifests the pathological features of both NPC and PD. In any case, we expect GQDs-based drugs will open new venues in clinical drug discovery against neurodegenerative diseases in the near future.

## 1.5. Experimental

**Synthesis of GQDs.** GQDs were synthesized by thermo-oxidatively cut carbon fibres (0.9 g, Carbon Make) in 400 ml 3:1 sulphuric acid and nitric acid (Samchun Chemical) at 80 °C for 1 day. The solution was dialyzed in DI water to remove acid and filtered with 20  $\mu$ m membrane filter (Cat#: 6809-5002; Whatman-Anodisc 47; GE Healthcare). The final product in powder form was obtained after subsequent rotary evaporation and freeze drying procedures.

**GQDs characterisation and biotinylation.** For TEM imaging, 10  $\mu$ l (10  $\mu$ g/ml)



GQDs solution was dropped onto a TEM grid and analysed with a high-resolution TEM (HR-TEM, JEM-3010, JEOL Ltd.). For Raman spectrum, 10 mg GQDs powder was prepared on a silicon substrate and measured with an Ar laser (514 nm)-based Raman spectrometer (RENISHAW). For AFM imaging, 5  $\mu$ l (10  $\mu$ g/ml) GQDs solution was dropped onto a silicon substrate. The sample was analysed in non-contact mode with an XE-100 AFM (Park Systems). XE data acquisition program was to acquire the final image (XEP 1.8.0). For biotinylation, 10 ml GQDs solution (5 mg/ml) was prepared in EDC conjugation buffer (pH 4.7). After gentle vortex, 12.5 mg EDC reagent (N-(3-Dimethylaminopropyl)-N'-ethylcarbodiimide hydrochloride, Sigma-Aldrich) was added and stirred for 1 hour. After replacing the carboxyl groups with EDC reagent, 25 mg of amine-PEG3-Biotin (EZ-Link, Thermo Scientific) was added and vigorously stirred for 1 day. The solution was dialysed and freeze-dried to yield the final GQD-biotin in powder form.

**Generation of patient specific iNSCs and differentiation.** iNSCs were generated from wild type human dermal fibroblasts (hDF) (GM5659; Coriell Institute for Medical research, Camden, NJ) and NPC patient-derived hDFs (GM03123; Coriell Institute for Medical research, Camden, NJ) according to the previous report<sup>20</sup>. In short, retroviral pMX-SOX2 and pMX-HMGA2 were transfected into 293 FT cells along with VSV-G and gag/pol plasmids using Fugene 6 transfection reagent (Roche, Indianapolis, IN, USA). The supernatants were collected at 48 and 72 hours post-transfection and used to infect hDFs with 5  $\mu$ g/ml polybrene (Sigma-Aldrich, Sigma, Ronkonkoma, NY, USA). After expansion of the infected cells, the medium was changed to the NSC maintenance medium (ReNcell NSC maintenance media; Millipore) with bFGF (Sigma) and EGF (Sigma) for neural stem cell induction. When colonies were visible they were picked and cultured in

neurosphere culture condition. For expansion, the cells were cultured as attached cells on PLO/FN-coated dishes. And for random differentiation, coverslips were coated with PLO/FN in 24-well plate and 5,000 cells of iNSCs were seeded and medium (Gibco BRL) with Gmax (Gibco) were added and cultured for 2 weeks.

**Immunocytochemistry.** Cells cultured in 24-well plate were washed with phosphate buffer saline (PBS; Gibco) and fixed with 4% paraformaldehyde (PFA) for 5 minutes at room temperature. To permeabilize the cell membrane and blocking stage, fixed cells were exposed to 0.5% Triton X-100 for 15 minutes and incubated with blocking solution containing 5% normal goat serum (NGS; zymed, San Francisco, CA, USA) for 1 hour at room temperature. Primary antibodies were used according to the manufacturer's recommended dilution, and cells exposed to primary antibody were incubated overnight at 4 °C. For secondary antibodies, Alexa 488- or Alexa 594-labeled antibodies (Molecular Probes, OR, USA) was used and incubated at 1 hour room temperature. 4',6-diamidino-2phenylindole (DAPI;Sigma) was used for nuclei staining. Images were captured on a confocal microscope (Nikon, Eclipse TE200, Japan).

**NMR Measurement.** All NMR spectra were recorded on Bruker Biospin Avance 700 MHz NMR spectrometer (1H frequency of 700.4 MHz) equipped with a cryogenic probe (Avance III, Bruker Biospin, Switzerland) at 37 °C. A standard pulse sequence with excitation sculpting (zgpg30 from Bruker Topspin using the standard parameter set) was employed as this pulse sequence allows better suppression of the water signal with the excellent flat baseline through the selective excitation of H<sub>2</sub>O during spin-echo and the use of purge gradients. Cholesterol of 0.05 mg/ml in 2% *dimethylsulfoxide-d<sub>6</sub>* (final concentration) and GQDs of 0.5 mg/ml were used for NMR measurements.

**LDH and TUNEL assays.** Primary cortical neurons were cultured and seeded on

poly-d-lysine-coated coverslip (10,000 cells/cm<sup>2</sup>). The cytotoxicity assays (LDH cytotoxicity assay kit, Pierce; TUNEL assay kit, Roche) were performed with different concentrations of GQDs in 10 DIV cortical neurons for a week.

***In vitro* and *in vivo* BBB permeability.** The procedures for *in vitro* and *in vivo* BBB permeability studies were reproduced from the previous report<sup>14</sup>. Briefly for *in vitro* permeability test, glial cells were harvested from 1-d-old C57BL/6 mice and seeded (100,000 cells/ml) under a transwell insert (Sigma-Aldrich) and incubated in a 5% CO<sub>2</sub> incubator for 2 days. Separately harvested brain microvascular endothelial cells (BMECs) were then plated (100,000 cells/ml) on top of the insert. The concentrations of GQDs and GQDs-biotin were measured with the FluoroBrite™ DMEM media inside (BMECs) and outside (glial cells) of the insert. For *in vivo* permeability, GQDs-biotin was i.p. injected in 8-week old C57BL/6 mice. After fixing the brain with 4% PFA for 6 hours, it was stored in 30% sucrose for 2 days. The DAB-based biotin signals were visualised with a DAB staining kit and the signals in the cerebellum and brainstem were confirmed with GoldEnhance™ EM Plus solution for immune-EM staining.

**Animal model.** A breeding pair of heterozygous Balb/c NPC<sup>+/-</sup> mice was purchased from Jackson Laboratories (Bar Harbor, MA). Wild-type control (WT; NPC<sup>+/+</sup>) and NPC1-knockout (NPC1; NPC<sup>-/-</sup>) mice were generated by breeding, and genotyping was carried out as previously described<sup>22</sup>. All experiments were approved and followed by regulation of the Institute of Laboratory Animals Resources (SNU IACUC Approval No: SNU-170816-2, Title of proposal: The efficacy of graphene quantum dots (GQDs) against NPC mouse; Institutional Animal Care and Use Committee, Seoul National University, Korea). All animals were maintained by an authorized animal facility under strict management.

***In vivo* administration of GQDs.** Beginning at 2 weeks of age, 200 µl of GQDs

(50 µg per mouse) were i.p. injected for 6 weeks on a weekly basis. At 8 weeks of age, the mice were sacrificed and the brains were sampled for immunoblotting or immunohistochemistry.

**Behaviour analyses.** The rotarod treadmill (7650 Accelerating model, Ugo Basile Biological Research Apparatus, Comerio, Italy) was used to coordinate the motor function ability. The mice were trained for 2 weeks prior to having their motor function tested from 6 to 8 weeks of age, tested once per week. The rotarod speed was set at 10 rpm and a maximum duration of 180 seconds. Representative records of the subjects were adopted as the mean performance time from 4 attempts<sup>23</sup>.

***In vivo* filipin staining and immunohistochemistry.** The isolated brains were perfused with 0.1 M PBS (pH 7.4) followed by 4% paraformaldehyde in 0.1 M PBS. Isolated brains were soaked in 4% paraformaldehyde in 0.1 M PBS overnight for post-fixation and cryo-protected with 30% sucrose. The brain tissues were transferred to a mold filled with an infiltration mixture (OCT compound; Sakura Finetek, Tokyo, Japan) and were maintained at 70 °C overnight until they were cryosectioned at 20 µm thick on a cryostat (CM 3050, Leica, Wetzlar, Germany). The sections were stained with filipin as previously described to compare the levels of accumulated cholesterol<sup>22</sup>. For the immunohistochemistry analysis, mouse brain sections were incubated with anti-calbindin (Abcam, Cambridge, MA) antibodies with blocking solution. Followed by being extensively washed with PBS and incubated with anti-rabbit secondary antibody conjugated with Alexa Fluor 488 (Molecular Probes, Eugene, OR, USA) for 1 h. Hoechst 33238 (1 µg/ml, Sigma-Aldrich) staining was used to visualize the cell nuclei. The densities of purkinje cells and total number were measured in the cerebella by ImageJ software (<http://rsb.info.nih.gov/ij/>, NIH).

**Immunoblotting.** At 8 weeks of age, the mice brain was removed and the

cerebella were separated from the whole brain. With lysis buffer (Pro-PREP, Inton Biotechnology, Korea), the cerebellum was homogenized. DC assay kit (Bio-Rad, Berkeley, USA) was used for quantification of the protein concentration. Equal amount of protein (20 µg) were injected in the wells of 10-15% sodium dodecyl sulfate-polyacrylamide gel electrophoresis (SDS-PAGE) and transferred to nitrocellulose membranes. After blocking the membranes with 3% bovine serum in a Tris-buffered saline with Tween (TBST: 20 mM Tris-HCl [pH 7.6], 137 mM NaCl, 1% Tween 20) and incubated with primary antibody (LC3, Novus). Proteins were detected by secondary antibody according to the manufacturer's specifications [horseradish peroxidase (HRP)-conjugated antibody (1:2000; Invitrogen, Carlsbad, USA; G21234)] followed with addition of enhanced chemiluminescence (ECL) detection kit (Amersham Pharmacia Biotech, Amersham, UK). The relative band intensities were determined by ImageJ software (<http://rsb.info.nih.gov/ij/>, NIH).

**Quantification and Statistical Analysis.** Mean  $\pm$  SD values were shown for more than three independent experiments. Through Graphic Pad Prism (v5.0, GraphPad), statistical analysis of the significance was calculated using with unpaired Student's t-test and one-way ANOVA followed by Bonferroni post hoc analysis.

**Data Availability.** There is no data relevant to accession codes or unique identifiers non-publicly available. The data that support the plots within this paper and other findings of this study are available from the corresponding authors upon reasonable request.

## 1.6. Supplementary Information

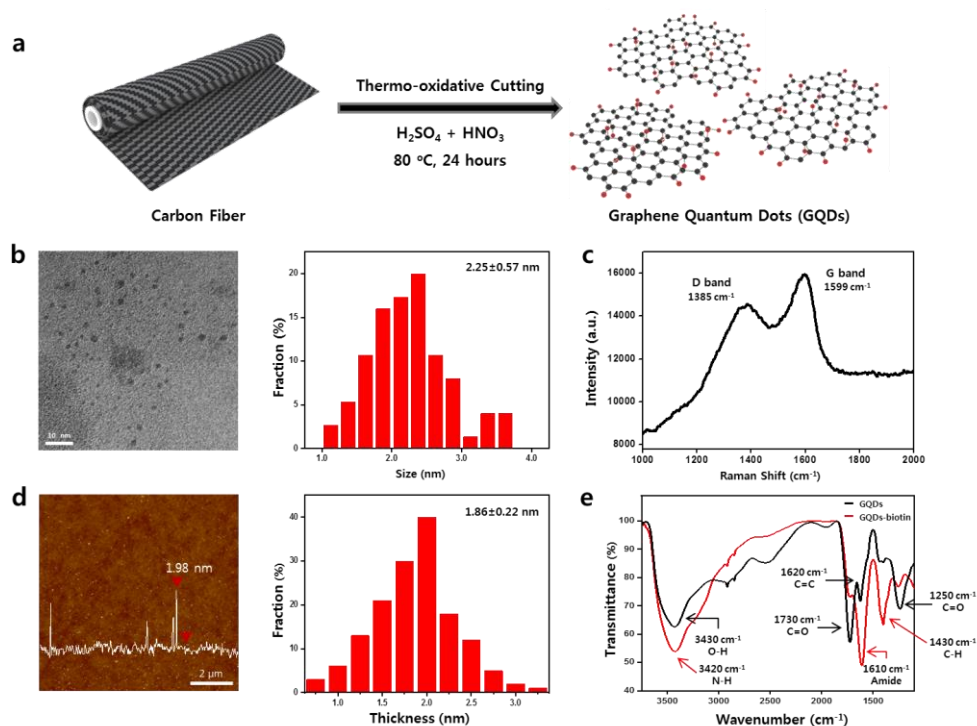


**Figure 4-S1. Characterisation of GQDs.** **a**, Schematic illustration of the GQDs synthesis from carbon fibres. **b**, Representative TEM imaging and the fractional analysis of the synthesised GQDs. **c**, Representative Raman spectrum of GQDs with designated D and G bands. **d**, Representative AFM imaging and respective the fractional analysis of the synthesised GQDs. **e**, FT-IR spectra of pristine (black) and biotinylated (red) GQDs with designated peaks for respective functional groups.

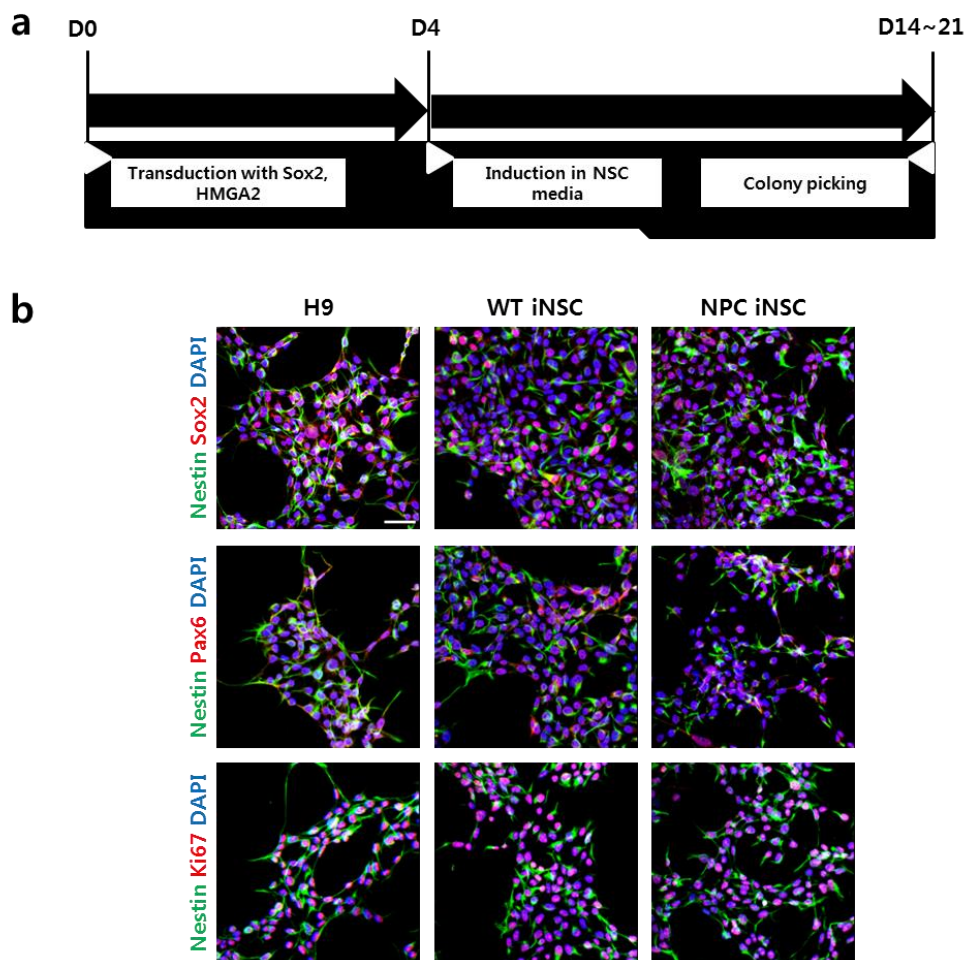


**Figure 4-S2. Direct conversion of NPC1 patient derived fibroblasts to neural stem cells.** **a**, Schematic illustration of the process of direct conversion. **b**, Immunocytochemistry analysis of neural stem cell specific marker proteins labeled with anti-nestin, Sox2, Pax6, and Ki67 in H9, WT iNSC and NPC iNSC. Nuclei were counterstained with DAPI.

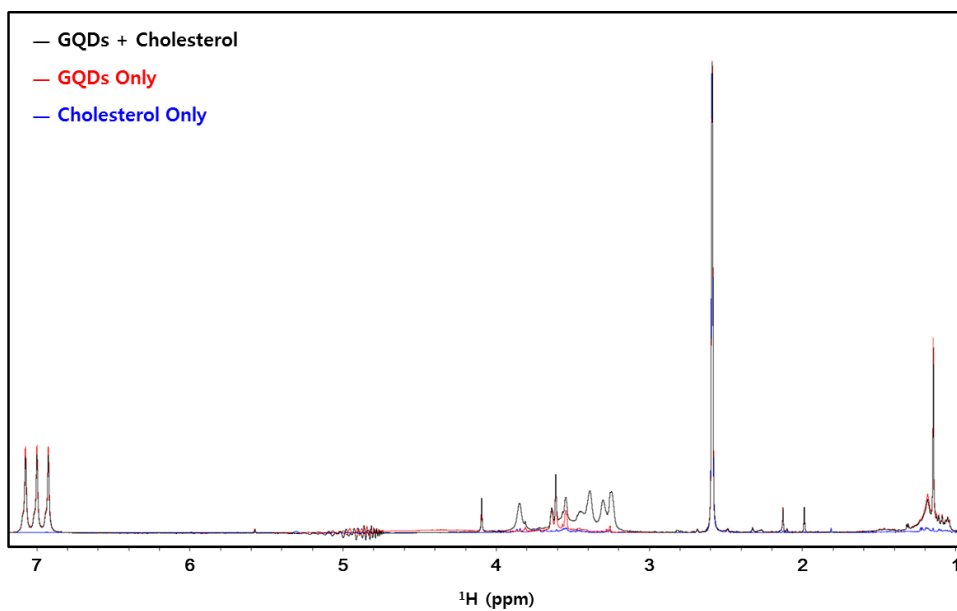


**Figure 4-S3. Extended  $^1\text{H}$  NMR spectra.** Each line represents cholesterol only (blue), GQDs only (red) and cholesterol with GQDs (black).



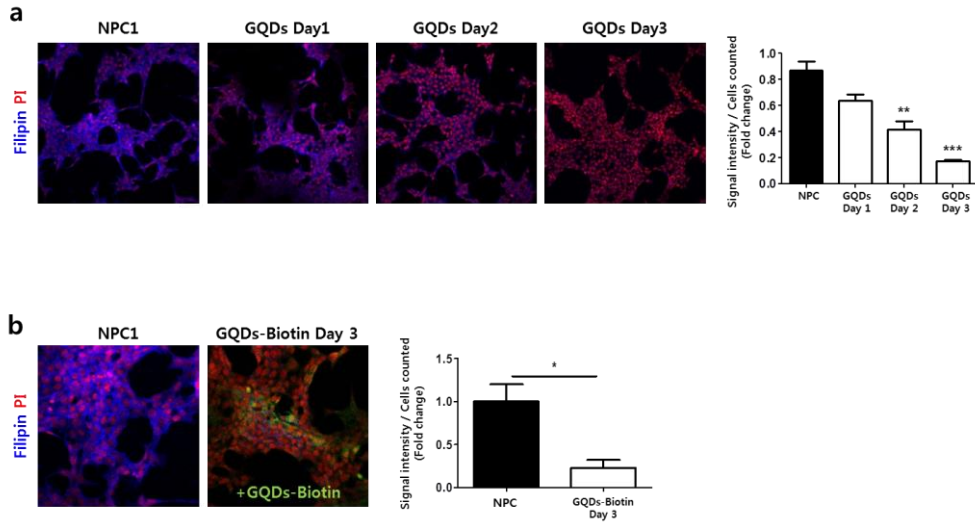


**Figure 4-S4. The time-dependent effect of GQDs on cholesterol accumulation in NPC-iNSC and the effect of GQDs-biotin. a**, GQDs were treated in NPC1 iNSC for 3 days and unesterified cholesterol was stained with filipin each day. Nuclei were counterstained with DAPI. Scale bars, 100  $\mu$ m. Data are presented as mean  $\pm$  standard error of the mean (s.e.m) from three independent experiments. Significance levels are expressed as asterisks: \*\* $P < 0.01$ , \*\*\* $P < 0.001$  via one-way ANOVA with Tukey's multiple comparisons test. **b**, Cholesterol accumulation is ameliorated by GQDs-biotin. GQDs-biotin was treated in NPC-iNSC for 3 days and stained with filipin to analysis unesterified cholesterol. Nuclei were counterstained with DAPI. Scale bars, 100  $\mu$ m. Significance levels are expressed as asterisks: \* $P < 0.0$  via one-way ANOVA with Tukey's multiple comparisons test.

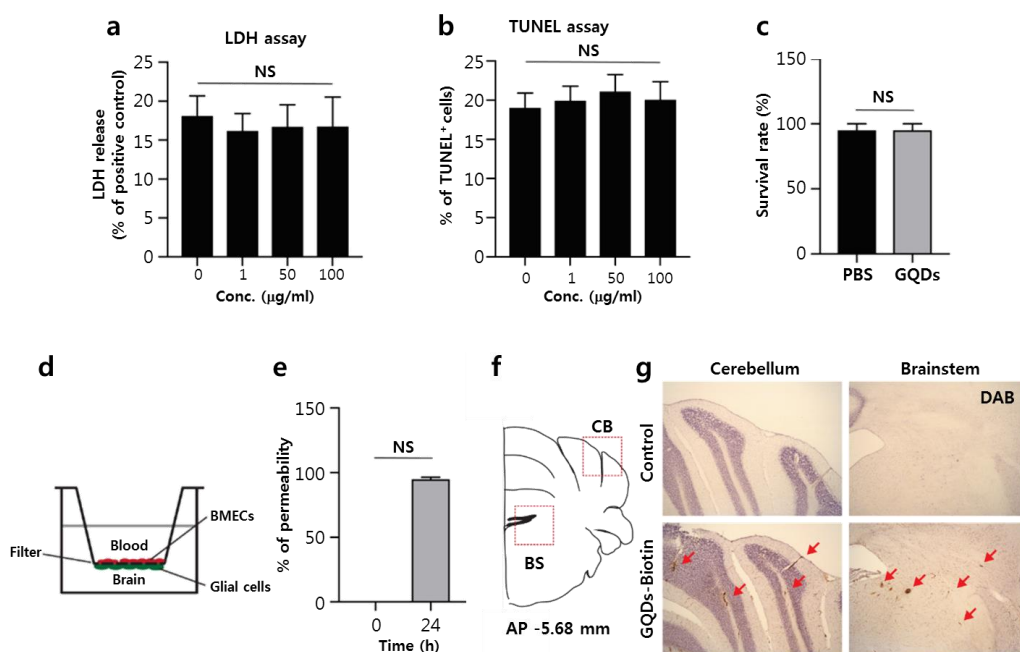


**Figure 4-S5. Cytotoxicity, survival rate, *in vitro* and *in vivo* permeability of GQDs.** **a**, LDH and **b**, TUNEL assays with varying GQDs concentrations for cytotoxicity studies. **c**, The mice survival rate with GQDs-injected mice for long-term *in vivo* toxicity analysis. **d**, Schematic illustration of the *in vitro* BBB study model and the permeability analysed with GQDs-biotin. **e**, DAB staining-based *in vivo* BBB permeability study in the cerebellum and brainstem with i.p. injected GQDs-biotin (2 mg/kg) mice. The red arrows point the DAB-stained areas of the brain regions.

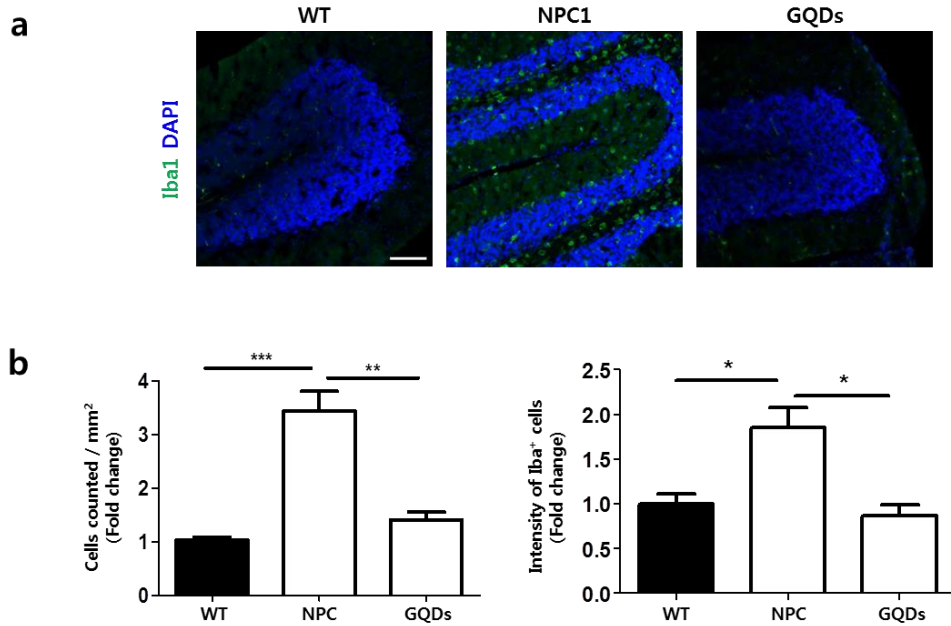


**Figure 4-S6. Inhibited microgliosis in GQDs treated NPC1 mutant mice.** Iba-1 immunostaining and its density and count show GQDs administration could inhibit microgliosis in the NPC1 cerebellum. Scale bars, 100  $\mu$ m. Data are presented as mean  $\pm$  standard error of the mean (s.e.m) from three independent experiments. Significance levels are expressed as asterisks: \*P < 0.05, \*\*P < 0.01, \*\*\*P < 0.001 via one-way ANOVA with Tukey's multiple comparisons test.

## 1.7. References

1. Vanier, M. T. Niemann-Pick disease Type C. *Orphanet Journal of Rare Diseases* **5** (2010)..
2. Pacheco, C. D. & Lieberman, A. P. The pathogenesis of Niemann-Pick type C disease: a role for autophagy? *Exp. Rev. Mol. Med.* **10**, e26 (2008).
3. Ikonen, E. Cellular cholesterol trafficking and compartmentalization. *Nat. Rev. Mol. Cell Biol* **9**, 125-138 (2008).
4. Sturley, S. L., Patterson, M. C., Balch, W. & Liscum, L. The pathophysiology and mechanisms of NP-C disease. *Biochim. Biophys. Acta* **1685**, 83-87 (2004).
5. Ko, D. C., Milenkovic, L., Beier, S. M., Manuel, M., Buchanan, A. & Scott, M. P. Cell-Autonomous Death of Cerebellar Purkinje Neurons with Autophagy in Niemann-Pick Type C Disease. *PLoS Genet.* **1**, e86 (2009).
6. Griffin, L. D., Gong, W., Verot, L. & Mellon, S. H. Niemann-Pick type C disease involves disrupted neurosteroidogenesis and responds to allopregnanolone. *Nat. Med.* **10**, 704-711, (2004).
7. Bosch, M. E. & Kielian, T. Neuroinflammatory paradigms in lysosomal storage diseases. *Front Neurosci.* **9**, 417 (2015).
8. Cougnoux, A. *et al.* Microglia activation in Niemann-Pick disease, type C1 is amendable to therapeutic intervention. *Hum Mol. Genet.* **27**, 2076-2089 (2018).
9. Sarkar, S. *et al.* Impaired autophagy in the lipid-storage disorder Niemann-Pick type C1 disease. *Cell Rep.* **5**, 1302-1315 (2013).
10. Rosenbaum, A. I. & Maxfield, F. R. Niemann-Pick type C disease: molecular mechanisms and potential therapeutic approaches. *J. Neurochem.* **116**, 789-795 (2011).
11. Rosenbaum, A. I., Zhang, G., Warren, J. D. & Maxfield, F. R. Endocytosis of beta-cyclodextrins is responsible for cholesterol reduction in Niemann-Pick type C mutant cells. *Proc. Natl. Acad. Sci. USA* **107**, 5477-5482 (2010).
12. Davidson, C. D. *et al.* Chronic Cyclodextrin Treatment of Murine Niemann-Pick C Disease Ameliorates Neuronal Cholesterol and Glycosphingolipid Storage and Disease Progression. *PLoS ONE* **4**, e6951 (2009).

13. Ory, D. S. *et al.* Intrathecal 2-hydroxypropyl- $\beta$ -cyclodextrin decreases neurological disease progression in Niemann-Pick disease, type C1: a non-randomised, open-label, phase 1–2 trial. *Lancet* **390**, 1758-1768 (2017).
14. Kim, D. *et al.* Graphene quantum dots prevent alpha-synucleinopathy in Parkinson's disease. *Nat. Nanotechnol.* **13** 812-818 (2018).
15. Zhang, L., Xu, B. & Wang, X. Cholesterol Extraction from Cell Membrane by Graphene Nanosheets: A Computational Study. *J. Phys. Chem. B* **120**, 957-964 (2016).
16. Bernabò, N. *et al.* Graphene oxide affects in vitro fertilization outcome by interacting with sperm membrane in an animal model. *Carbon* **129**, 428-437 (2018).
17. Qin, Y. *et al.* Graphene quantum dots induce apoptosis, autophagy, and inflammatory response via p38 mitogen-activated protein kinase and nuclear factor-kappaB mediated signaling pathways in activated THP-1 macrophages. *Toxicology* **327**, 62-76 (2015).
18. Tomic, S. *et al.* Graphene quantum dots suppress proinflammatory T cell responses via autophagy-dependent induction of tolerogenic dendritic cells. *Biomaterials* **146**, 13-28 (2017).
19. Yu, K. R. *et al.* Rapid and Efficient Direct Conversion of Human Adult Somatic Cells into Neural Stem Cells by HMGA2/let-7b. *Cell Rep.* **20**, 441-452 (2015).
20. Sung, E. A. *et al.* Generation of patient specific human neural stem cells from Niemann-Pick disease type C patient-derived fibroblasts. *Oncotarget* **8**, 85428-85441 (2017).
21. Whitney, E. R., Kemper, T. L., Rosene, D. L., Bauman, M. L. & Blatt, G. J. Calbindin-D28k is a more reliable marker of human Purkinje cells than standard Nissl stains: a stereological experiment. *J. Neurosci. Methods* **168**, 42-47 (2008).
22. Seo, Y. *et al.* Human umbilical cord blood-derived mesenchymal stem cells protect against neuronal cell death and ameliorate motor deficits in Niemann Pick type C1 mice. *Cell Transplant* **20**, 1033-1047 (2011).
23. Vöikar, V., Rauvala, H. & Ikonen, E. Cognitive deficit and development of motor impairment in a mouse model of Niemann-Pick type C disease. *Behav. Brain. Res.* **132**, 1-10 (2002).

# Appendix

## EDUCATION

**Sep. 2009 ~ Dec. 2012**, Department of Chemistry, Krieger School of Arts and Sciences, Johns Hopkins University, Baltimore, MD, USA. Bachelor of Arts in Chemistry

**Mar. 2013 ~ Feb. 2018**, Department of Chemistry, College of Natural Sciences, Seoul National University, Seoul, Republic of Korea. Doctor of Philosophy in Physical Chemistry.

## PROFESSIONAL EXPERIENCE

**Feb. 2010 ~ Dec. 2012**, Department of Neurology, Institute for Cell Engineering, Program in Neurorogeneration and Stem Cell Program, The Johns Hopkins University School of Medicine, Baltimore, MD, USA. Undergraduate Research Assistant.

## AWARDS AND HONORS

**Global Ph.D. Fellowship.** Therapeutic Applications of Graphene Quantum Dots (GQDs) for Neurodegenerative Diseases. The National Research Foundation of Korea (NRF), Ministry of Education (Mar. 2014 ~ Feb. 2019).

**Distinguished Poster Award.** "Highly Efficient Nucleic Acid Drug Delivery by Graphene Quantum Dots (GQDs)-Mediated Hyperthermia." The 2nd Korean Graphene Symposium (2015).

## PEER-REVIEWED PUBLICATIONS

(<sup>†</sup> denotes equal contribution; \* denotes corresponding author)

**9.** M. J. Park, H. –H. Choi, B. Park, J. Y. Lee, C. –H. Lee, Y. S. Choi, Y. Kim, **J. M. Yoo**, H. Lee, B. H. Hong<sup>\*</sup>. "Enhanced Chemical Reactivity of Graphene by Fermi Level Modulation." *Chemistry of Materials*, **30**, 5602-5609 (2018)

8. D. Kim<sup>†</sup>, **J. M. Yoo**<sup>†</sup>, H. Hwang, J. Lee, S. H. Lee, S. P. Yun, M. J. Park, M. Lee, S. Choi, S. H. Kwon, S. Lee, S. -H. Kwon, S. Kim, Y. J. Park, M. Kinoshita, Y. - H. Lee, S. Shin, S. R. Paik, S. J. Lee, S. Lee, B. H. Hong\* and H. S. Ko\*. "Graphene quantum dots prevent  $\alpha$ -synucleinopathy in Parkinson's disease." *Nature Nanotechnology*, **13**, 812-818 (2018)
7. **J. M. Yoo**<sup>†</sup>, B. Park<sup>†</sup>, S. J. Kim, Y. S. Choi, S. Park, E. H. Jeong, H. Lee\* and B. H. Hong\*. "Catalytic degradation of phenols by recyclable CVD graphene films." *Nanoscale*, **10**, 5840-5844 (2018)
6. J. B. Park<sup>†</sup>, Y. -J. Kim<sup>†</sup>, S. -M. Kim, **J. M. Yoo**, Y. Kim, R. Gorbachev, I. I. Barbolina, S. J. Kim, S. Kang, M. -H. Yoon, S. -P. Cho, K. S. Novoselov and B. H. Hong\*. "Non-destructive electron microscopy imaging and analysis of biological samples with graphene coating." *2D Materials*, **3**, 045004 (2016)
5. S. J. Kim<sup>†</sup>, T. Choi<sup>†</sup>, B. Lee, S. Lee, K. Choi, J. B. Park, **J. M. Yoo**, Y. S. Choi, J. Ryu, P. Kim, J. Hone\* and B. H. Hong\*. "Ultraclean Patterned Transfer of Single-Layer Graphene by Recyclable Pressure Sensitive Adhesive Films." *Nano Letters*, **15**, 3236-3240 (2015)
4. Y. Kim<sup>†</sup>, J. Park<sup>†</sup>, J. Kang, **J. M. Yoo**, K. Choi, E. S. Kim, J. -B. Choi, C. Hwang, K. S. Novoselov and B. H. Hong\* "A highly conducting graphene film with dual-side molecular n-doping." *Nanoscale*, **6**, 9545-9549 (2014)
3. S. J. Kim<sup>†</sup>, J. Ryu<sup>†</sup>, S. Son, **J. M. Yoo**, J. B. Park, D. Won, E. -K. Lee, S. -P. Cho, S. Bae, S. Cho and B. H. Hong\*. "Simultaneous Etching and Doping by Cu-Stabilizing Agent for High-Performance Graphene-Based Transparent Electrodes." *Chemistry of Materials*, **26**, 2332-2336 (2014)
2. Y. Kim<sup>†</sup>, J. Ryu<sup>†</sup>, M. Park, E. S. Kim, **J. M. Yoo**, J. Park, J. H. Kang and B. H. Hong\*. "Vapor-Phase Molecular Doping of Graphene for High-Performance Transparent Electrodes." *ACS Nano*, **8**, 868-874 (2014)
1. Y. Kim, **J. M. Yoo**, H. R. Jeon\*, B. H. Hong\*. "Efficient n-doping of graphene films by APPE (aminophenyl propargyl ether): a substituent effect." *Physical Chemistry Chemical Physics*, **15**, 18353-18356 (2013)

## MANUSCRIPTS UNDER REVIEW / IN PREPARATION

3. I. Kang<sup>†</sup>, **J. M. Yoo**<sup>†</sup>, D. Kim, D. J. Kim, J. Kim, B. -C. Lee, J. Y. Lee, J. -J. Kim, N. Shin, Y. -H. Lee, B. H. Hong<sup>\*</sup>, K. -S. Kang<sup>\*</sup>. “Graphene Quantum Dots Alleviate Impaired Functions in Niemann-Pick Type C Disease In Vivo.”
2. D. Kim, H. Hwang, S. Choi, S. H. Kwon, S. -U. Kang, T. -I. Kam, K. Kim, S. S. Karuppagounder, B. -G. Kang, S. Lee, **J. M. Yoo**, H. Park, S. Kim, W. Yan, Y. -S. Li, S. -H. Kuo, O. Pletnikova, J. C. Troncoso, X. Mao, V. L. Dawson, T. M. Dawson<sup>\*</sup> and H. S. Ko<sup>\*</sup>. “TRIP12 Ubiquitination of GBA1 Contributes to Neurodegeneration in Parkinson’s Disease.”
1. B. -C. Lee<sup>†</sup>, J. Y. Lee<sup>†</sup>, **J. M. Yoo**, I. Kang, J. -J. Kim, N. Shin, D. J. Kim, S. W. Choi, B. H. Hong and K. -S. Kang<sup>\*</sup>. “Nano-sized graphene oxides attenuate intestinal inflammation by modulating immune homeostasis.”

## REVIEWS AND BOOK CHAPTERS

2. **J. M. Yoo**, D. W. Hwang, and B. H. Hong. (2018). “Graphene-Based Nanomaterials.” In: D. Lee, ed., *Radionanomedicine: Combined Nuclear and Nanomedicine*. Springer International Publishing, pp.79-103.
1. **J. M. Yoo**<sup>†</sup>, J. H. Kang<sup>†</sup> and B. H. Hong<sup>\*</sup>. "Graphene-based nanomaterials for versatile imaging studies." *Chemical Society Reviews*, **44**, 4835-4852 (2015)

## SELECTED PRESENTATIONS

**The 2019 MRS Spring Meeting & Exhibit (Contributed Talk).** *Graphene Quantum Dots Prevent  $\alpha$ -Synucleinopathy in Parkinson’s Disease*. Phoenix, AZ, USA (April 2019).

**The 2018 MRS Spring Meeting & Exhibit (Poster).** *Catalytic degradation of phenols by recyclable CVD graphene film*. Phoenix, AZ, USA (April 2018).

**The 4th Korea Global Ph.D. Fellowship Conference.** *Therapeutic Applications of Graphene Quantum Dots (GQDs) for Parkinson’s Disease*. Busan, Republic of Korea (December 2017).



**The 4th Korean Symposium on Graphene and 2D Materials (Poster).** *Catalytic degradation of phenols by recyclable CVD graphene film.* Buyeo, Republic of Korea (April 2017).

**The Seawater Utilization Plant Research Center: Korea Research Institute of Ships & Ocean Engineering (Invited Talk).** *Graphene: A New Class of Materials for Various Future Applications.* Goseong, Republic of Korea (March 2017).

**The 1st International Society for Nanomedicine (ISNM) Congress (Poster).** *Therapeutic Effects of Functionalized Nanographene: Parkinson's Disease.* Seoul, Republic of Korea (October 2016).

**8th International Conference on Recent Progress in Graphene / 2D Research (Contributed Talk).** *Therapeutic Application of Graphene Quantum Dots (GQDs) for Parkinson's Disease.* Seoul, Republic of Korea (October 2016)

**The 3rd Korean Graphene Symposium (Contributed Talk).** *Therapeutic Applications of Graphene Quantum Dots (GQDs) for Parkinson's Disease.* Buyeo, Republic of Korea (April 2016)

**Graphene Flagship – Graphene Week 2015 (Poster).** *Highly Efficient Nucleic Acid Drug Delivery by Graphene Oxides (GOs)-Mediated Hyperthermia.* Manchester, UK (June 2015).

**The 2nd Korean Graphene Symposium (Poster).** *Highly Efficient Nucleic Acid Drug Delivery by Graphene Quantum Dots (GQDs)-Mediated Hyperthermia.* Buyeo, Republic of Korea (March 2015).

# 초록

## 그래핀 기반 나노소재들의 바이오의료 응용연구

유제민

자연과학대학 화학부

서울대학교 대학원

그래핀은 2004년 맨체스터 대학의 과학자들에 의해 처음으로 실험적으로 발견된 이후부터 전례 없이 뛰어난 다양한 특성들로 많은 과학자들의 이목을 끌었다. 실질적으로 '그래핀'이라는 용어는 흑연을 1층으로 박리시킨 원자 한 층의 필름을 의미하며, 초기에는 이 필름을 활용해 인듐 주석 산화물 박막을 대체할 투명 유연 디스플레이 소재로서의 가능성이 주목받았다. 최근에는 이러한 가능성을 넘어 수용액상에 녹을 수 있는 형태의 그래핀 기반 물질들이 지닌 다양한 생물학적, 나노의학적 분야에 적합한 특성들이 보고되며 또 다른 주목을 받고 있다. 특히 최근 이러한 연구분야들에서 신소재를 활용한 새로운 응용연구들이 각광받고 있으며, 우리는 다양한 시도들을 통해 몇 가지 선구적인 결과들을 얻어낼 수 있었다. 따라서 본 논문에서는 그동안 수행한 몇가지 연구들을 취합하여 그래핀 및 그래핀 기반 나노물질들이 인체 보건 및 퇴행성 뇌질환 치료에 어떠한 영향을 끼치는지에 대해 보고한다.

제1장에서는 그래핀 기반 나노물질들에 대해 생물학 및 의과학 분야 적용 사례들과 이에 필요한 합성법 및 최근 보고된 몇 가지 독성연구에 대해 간략히 소개한다.

제2장에서는 CVD 그래핀 필름을 활용한 산업폐수처리 실험에 대해 소개한다. 페놀과 페놀 기반 유기분자들은 산업폐수에 대량 포함되어 있으며 돌연변이 유발 요인 혹은 발암요인으로 여겨진다. 철 촉매를 활용한 기존의

페놀 분해 방법은 페놀을 완전히 분해시킬 수 있다는 장점은 있으나 기초설비비용과 처리비용이 높은 편이며 처리 과정에서 발생하는 추가적인 촉매 산물 제거 과정 및 산성조건 설정 등 부수적인 환경문제를 야기한다. 본 연구에서는 재활용 가능한 CVD 그래핀 필름을 활용해 페놀을 분해시킬 수 있는 활성산소를 생성하고 향후 추가적으로 개선이 가능한 새로운 환경친화적 촉매로의 적용 가능성을 보여준다.

제3장에서는 그래핀 양자점의 파킨슨병 치료제 개발로서의 가능성을 소개한다. 파킨슨병의 발병과정은 그 원인이 명확히 밝혀지지 않는으나 알파시뉴클레인이라는 신경 단백질의 응집이 매우 중요하다고 알려져 있다. 다양한 실험을 통해 그래핀 양자점이 알파시뉴클레인의 초기 응집을 억제할 뿐만 아니라 이미 형성된 응집체를 풀어주고, 주변 신경세포들의 전이를 억제할 수 있다는 사실을 보여준다. 또한 혈뇌장벽 투과를 통해 중뇌에 있는 도파민 작동성 신경세포의 사멸을 막아줄 수 있다는 결과들을 통해 단순히 증상의 완화만을 목적으로 하는 기존의 약물들과는 달리 질병의 근본적 치료가 가능한 임상 약물로서의 가능성을 보여준다.

마지막으로 제4장에서는 그래핀 양자점을 또 다른 퇴행성 뇌질환 중 하나인 니만피크C형에 대한 치료제로서의 가능성을 보여준다. 이 실험을 통해 그래핀 양자점이 세포 내 비정상적 콜레스테롤 축적 및 손상된 자가포식현상에 도움을 줄 수 있다는 결과를 소개하고자 한다.

**주요어:** 그래핀, 그래핀 양자점, 환경촉매, 의과학적 적용, 나노의학, 퇴행성 뇌질환

**학번:** 2013-20274